



Universidad de Concepción
Dirección de Postgrado
Facultad de Ciencias Naturales y Oceanográficas
Programa de Doctorado en Oceanografía

**Modelling the global climate-carbon cycle across the
Middle-Pleistocene Transition using the new
Earth System Model DCESS II**

**(Modelación del ciclo global del carbono a través de la
Transición del Pleistoceno Medio utilizando el nuevo
Modelo del Sistema Tierra DCESS II)**

Tesis para optar al grado de Doctor en Oceanografía

ESTEBAN JAVIER FERNÁNDEZ VILLANUEVA
CONCEPCIÓN-CHILE
Agosto de 2025

Colaborador Principal: Gary Shaffer
Dpto. Oceanografía, Facultad de Ciencias Naturales y Oceanográficas
Universidad de Concepción

© 2025 Esteban Javier Fernández Villanueva
Se autoriza la reproducción total o parcial, con fines académicos, por cualquier medio o procedimiento, incluyendo la cita bibliográfica del documento.

Universidad de Concepción
Dirección de Postgrado

La Tesis de *Doctorado en Oceanografía* titulada “*Modelling the global climate-carbon cycle across the Middle-Pleistocene Transition using the new Earth System Model DCESS II*”, del Sr. Esteban Javier Fernández Villanueva y realizada bajo la Facultad de Ciencias Naturales y Oceanográficas, Universidad de Concepción, ha sido aprobada por la siguiente Comisión de Evaluación:

Dr. Gary Shaffer
Colaborador Principal
University of Copenhagen

Dr. Oscar Pizarro
Profesor guía
Universidad de Concepción

Dr. Martin Jacques
Miembro Comité de Tesis
Universidad de Concepción

Dr. Fabrice Lambert
Evaluador externo
Pontificia Universidad Católica

Dra. Pamela Hidalgo
Director
Programa de Doctorado en Oceanografía
Universidad de Concepción

*Agradezco a todas y todos quienes me han
acompañado en este proceso.*

ACKNOWLEDGMENTS

I wish to express my deepest gratitude to my supervisor, Prof. Gary Shaffer, for giving me the opportunity to do this study, for the many fruitful and extensive discussions that shaped this work, and for his invaluable support during difficult times. My sincere thanks also to Prof. Donald Canfield for inviting me to the Nordcee Institute as part of my PhD. His vision of science is truly inspiring. I particularly acknowledge Prof. Oscar Pizarro for his role and willingness throughout this process.

This journey has been one of light and shadows. In moments of doubt, family and friends were fundamental; to them, my eternal gratitude, especially to Edgart Flores for his unconditional friendship. To all those who were probably burdened more than reasonably. Above all, to Patricia González for standing by me and easing the hardest moments. Finally, to a faithful anonymous friend, whose endless joy was a balm during our time together.

Curriculum Vitae

Esteban Javier Fernández Villanueva

Born on February 8, 1988, Santiago, Chile

2013: Bachelor's degree in Physical Sciences, Universidad de Concepción

2015: Geophysicist, Universidad de Concepción

2018: Master's degree in Meteorology and Climatology, Universidad de Chile

RESEARCH AREA

Principal: Earth System modelling

Secondary: Paleoclimate

Other: Earth system interactions and climate feedbacks, large-scale ocean circulation, global biogeochemical cycles, climate modelling.

PUBLICATIONS

- Shaffer, G., **Fernández Villanueva, E.**, Rondanelli, R., Pedersen, J. O. P., Olsen, S. M., and Huber, M., 2017: Implementation of methane cycling for deep-time global warming simulations with the DCESS Earth system model (version 1.2). *Geoscientific Model Development.*, 10, 4081–4103, <https://doi.org/10.5194/gmd-10-4081-2017>.
- **Fernández Villanueva, E.**, and Shaffer, G., 2025. Presentation, calibration and testing of the DCESS II Earth system model of intermediate complexity (version 1.0). *Geoscientific Model Development*, 18(7), 2161-2192. <https://doi.org/10.5194/gmd-18-2161-2025>.
- Shaffer, G., **Fernández Villanueva, E.**, and Karas, C., 2025: Role of mid- and high-latitude, Southern Hemisphere processes for ushering in the Middle Pleistocene Transition. Submitted to *Paleoceanography and Paleoclimatology*.
- Shaffer, G., **Fernández Villanueva, E.**, Luzardi, A., C., Pedersen, J. O. P., Huber, M., and Zachos, J.: Coupled evolution of climate, Antarctic Ice Sheet and carbon dioxide, 66 to 5 million years ago. In preparation to be submitted to *Science/Science Advances*.

- Xiong, G., Zhang, F., **Fernández Villanueva, E.**, Shaffer, G., Lin, Y., Zhang, H., Wei, G., Wang, W., Cao, M., Mills, B., Cheng, H., and Shen, S.: Methane hydrate release expanded seafloor deoxygenation and initiated the Paleocene–Eocene Thermal Maximum. In preparation to be submitted to Nature Geoscience.

LABORAL EXPERIENCE

- 2014: Student research assistant in project “Modelling and analysis of the Paleocene-Eocene Thermal Maximum and other past warming events using the DCESS Earth System Model”. Principal Investigator: Dr. Gary Shaffer. Chilean National Agency for Research and Development (ANID), FONDECYT nr. 1120040.
- 2015-2016: Thesis student in project Paleoclimate of the Southern Hemisphere - Climate Modelling Research line. Principal Investigator: Dr. Fabrice Lambert. Chilean National Agency for Research and Development (ANID) Millennium Science Initiative Program (Millenium Nucleus NC120066).
- 2017-2019: Student research assistant in project “Modelling the possible role of methane in deep-time, global warming events using the DCESS Earth System Model”. Principal Investigator: Dr. Gary Shaffer. Chilean National Agency for Research and Development (ANID), FONDECYT nr. 1150913.
- 2020-2022: Student research assistant in project “Modelling the interactive evolutions of climate, carbon cycling and the Antarctic Ice Sheet across the Eocene-Oligocene transition using the DCESS Earth System and Antarctic Ice Sheet models”. Principal Investigator: Dr. Gary Shaffer. Chilean National Agency for Research and Development (ANID), FONDECYT nr. 1190230.
- 2023-2025: Student research assistant in project “Last deglacial South Pacific Antarctic Intermediate Water variability and its role for atmospheric CO₂ increases”. Principal Investigator: Cyrus Karas. Chilean National Agency for Research and Development (ANID), FONDECYT nr. 1230534.

TEACHING EXPERIENCE

- July-December 2016: Teaching assistant course “Sistema Climático” for undergraduate and graduate students in Faculty of Engineering. Universidad de Chile, Chile. Course instructed by Dr. Maisa Rojas.
- July-December 2019: Teaching assistant undergraduate course “Tópicos en Geofísica” for students of Geophysics at the Universidad de Concepción, Chile. Course instructed by Dr. Oscar Pizarro.

INTERNSHIPS

- Multiple visits to GAIA Antarctica Research Institute at the Universidad de Magallanes. Supervised by Dr. Gary Shaffer.
- July 2016: Niels Bohr Institute, University of Copenhagen, Denmark. Supervised by Dr. Gary Shaffer.
- August 2019: Nordcee Research Institute, University of Southern Denmark, Denmark. Supervised by Dr. Donald Canfield.
- November 2022 – April 2023: Nordcee Research Institute, University of Southern Denmark, Denmark. Supervised by Dr. Donald Canfield.

CONFERENCES

- September 2022: Poster presentation (main author) at the 14th International Conference on Paleoceanography (ICP-14): “A new, extended version of the DCESS Earth System model”. Bergen, Norway.
- September 2019: Poster presentation (main author) at the 13th International Conference on Paleoceanography (ICP-13): “The potential role of nitrous oxide in ancient global warming events”. Sydney, Australia.

- September 2019: Poster presentation (co-author) at the 13th International Conference on Paleoceanography (ICP-13): “Cenozoic evolution of global mean temperature, Antarctic Ice Sheet size and atmospheric $p\text{CO}_2$ ”. Sydney, Australia.
- November 2017: Oral presentation (main author) at the V Conference in Physical Oceanography, Meteorology and Climate: “Expansion of an Earth System model to deal with a suboxic/anoxic ocean and its effect on climate”. Concepción, Chile.
- October 2015: Poster presentation (main author) at the 11th International Conference on Southern Hemisphere Meteorology and Oceanography (ICSHMO): “Simulation and climate sensitivity of the warm climate of the early Eocene with the DCESS Earth System Model”. Santiago, Chile.

CONTENTS

ABSTRACT	x
RESUMEN	xii
1. INTRODUCTION.....	1
1.1. The global climate carbon cycle.....	1
1.2. The Middle-Pleistocene Transition	6
1.3. Earth System Models.....	6
2. HYPHOTESSES AND SPECIFIC GOALS	8
2.1. Hypotheses	8
2.2. Specific Objectives	8
3. METHODOLOGY	9
3.1. A new Earth System model	9
3.2. Long-term simulations and the MPT.....	14
4. RESULTS	17
4.1. Chapter 1: “Presentation, calibration and testing of the DCESS II Earth system model of intermediate complexity (version 1.0)”	17
4.2. Chapter 2: “Role of mid- and high-latitude, Southern Hemisphere processes for ushering in the Middle Pleistocene Transition”	51
5. DISCUSSION	92
5.1. A new Earth System Model.....	92
5.2. The Middle Pleistocene Transition.....	94
6. CONCLUSIONS.....	97
7. REFERENCES.....	98

ABSTRACT

Glacial-interglacial cycles increased in length from about 41 to 100 thousand years during the Middle Pleistocene Transition (MPT) about 1.5 to 0.8 million years ago without major changes in orbital forcing characteristics, pointing toward explanations in terms of Earth system properties and feedbacks. This took place in step with strong global cooling after several million years of weaker cooling. Such strong MPT cooling likely set the stage for longer ice age cycles by, for example, facilitating Northern Hemisphere ice sheet growth. Here simulations with a newly-developed Earth System model of Intermediate Complexity together with sea surface temperature reconstructions were used to evaluate possible causes of the MPT cooling.

First, a new Earth system model of intermediate complexity, DCESS II, is presented that builds upon, improves and extends the Danish Center for Earth System Science (DCESS) Earth system model (DCESS I). DCESS II has considerably greater spatial resolution than DCESS I while retaining the fine, 100 m vertical resolution in the ocean. It contains modules for the atmosphere, ocean, ocean sediment, land biosphere and lithosphere and is designed to deal with global change simulations on scales of years to millions of years while using limited computational resources. Tracers of the atmospheric module are temperature, nitrous oxide, methane ($^{12,13}\text{C}$ isotopes), carbon dioxide ($^{12,13,14}\text{C}$ isotopes) and atmospheric oxygen. For the ocean module, tracers are conservative temperature, absolute salinity, water ^{18}O , phosphate, dissolved inorganic carbon ($^{12,13,14}\text{C}$ isotopes), alkalinity and dissolved oxygen. Furthermore, the ocean module considers simplified dynamical schemes for large-scale meridional circulation and sea ice dynamics, stratification-dependent vertical diffusion, a gravity current approach to the formation of Antarctic Bottom Water, and improvements in ocean biogeochemistry. DCESS II has two hemispheres with six zonally averaged atmospheric boxes and 12 ocean sectors distributed across the Indian–Pacific, the Atlantic, the Arctic and the Southern oceans. A new extended land biosphere scheme is implemented that considers three different vegetation types whereby net primary production depends on sunlight and atmospheric carbon dioxide (CO_2). The ocean sediment and lithosphere model formulations are adopted from DCESS I but now applied to the multiple ocean and land regions of the new model.

Model calibration was carried out for the pre-industrial climate, and model steady-state solutions were compared against available modern-day observations. For the most part, calibration results

agree well with observed data, including excellent agreement with ocean carbon species. This serves to demonstrate model utility for dealing with the global carbon cycle. Two idealized experiments were carried out in order to explore model performance. First, the model was forced by varying Ekman transport out of the model Southern Ocean, mimicking the effect of Southern Hemisphere westerly wind variations, and second, freshwater melting pulses from the Antarctic ice sheet on the model Southern Ocean shelf were imposed. Changes in ocean circulation and in the global carbon cycle found in these experiments are in line with results from much more complex models. Thus, we find DCESS II to be a useful and computationally friendly tool for simulations of past climates as well as for future Earth system projections.

When the new Earth system model, DCESS II, is used to study the Middle Pleistocene Transition (MPT), four forcings are proposed in order to explain strong observed global cooling across the MPT: 1. Southern West Wind strength and position, 2. Sea ice and iceberg export from the Antarctic shelf, 3. Dust fertilization of the Southern Ocean and 4. Northern Hemisphere ice sheet extent. We find that weakened, equatorward-shifted Southern West Winds in combination with increased sea ice and iceberg exports from the Antarctic Shelf can explain much of the strong MPT cooling. Simulations suggest that these changes caused the cooling by decreasing heat and carbon exchange between the upper and deep Southern Ocean and by increasing recirculation in the deep ocean, leading to deep ocean isolation and carbon storage together with atmospheric CO₂ drawdown. Dust-driven iron fertilization further enhanced this storage and drawdown while Northern Hemisphere ice sheet growth contributed mainly to regional cooling while promoting land biomass reduction that releases CO₂ to the atmosphere.

RESUMEN

Ciclos glaciales-interglaciales incrementaron duración de 41 a 100 mil años durante la Transición del Pleistoceno Medio (MPT) alrededor de 1.5 a 0.8 millones de años atrás sin mayores cambios en el forzamiento orbital característico. apuntando a explicaciones en términos de propiedades y retroalimentaciones del sistema Tierra. Esto ocurrió junto con un fuerte enfriamiento global después de varios millones de años de enfriamiento más débil. Tal enfriamiento durante MPT probablemente sentó las bases para ciclos glaciales más largos, por ejemplo, favoreciendo el crecimiento de mantos de hielo en el Hemisferio Norte (HN). Aquí, se usaron simulaciones con un nuevo modelo del Sistema Tierra de complejidad intermedia junto con reconstrucciones de temperatura superficial del mar para evaluar posibles causas del enfriamiento durante MPT.

En primer lugar, se presenta un nuevo modelo del Sistema Tierra de complejidad intermedia, DCESS II, que se basa, mejora y amplía el modelo llamado Danish Center for Earth System Science (DCESS I). DCESS II tiene una resolución espacial considerablemente mayor que DCESS I, al tiempo que mantiene la resolución vertical de 100 m en el océano. Contiene módulos para la atmósfera, el océano, los sedimentos marinos, la biósfera terrestre y la litósfera, y está diseñado para llevar cabo simulaciones de cambio global en escalas de años a millones de años sin la utilización de grandes recursos computacionales. Los trazadores del módulo atmosférico son temperatura, óxido nitroso, metano (con isótopos $^{12,13}\text{C}$), dióxido de carbono (con isótopos $^{12,13,14}\text{C}$) y oxígeno atmosférico. Para el módulo oceánico, los trazadores son temperatura conservativa, salinidad absoluta, ^{18}O del agua de mar, fosfato, carbono inorgánico disuelto (con isótopos $^{12,13,14}\text{C}$), alcalinidad y oxígeno disuelto. Además, el módulo de océano considera un esquema dinámico simplificado para la circulación meridional de gran escala y la dinámica del hielo marino, la difusión vertical es dependiente de la estratificación, un enfoque de corriente de gravedad para la formación del agua de fondo Antártica y mejoras en la biogeoquímica del océano. DCESS II tiene 2 hemisferios con seis sectores atmosféricos promediadas zonalmente y 12 sectores oceánicos distribuidos entre el Océano Índico-Pacífico, Atlántico, Ártico y Austral. Se ha implementado un nuevo esquema ampliado de la biósfera terrestre que considera tres tipos diferentes de vegetación, en el que la producción primaria neta depende de la luz solar y el dióxido de carbono atmosférico (CO_2). Las formulaciones del

modelo de sedimento y litósfera se adoptan de DCESS I, pero ahora aplicados a las múltiples regiones oceánicas y terrestres del nuevo modelo.

La calibración del modelo se llevó a cabo para el clima del pre-industrial y se compararon las soluciones del modelo en estado estacionario con las observaciones modernas disponibles. En su mayor parte, los resultados de la calibración concuerdan bien con los datos observados, incluyendo una excelente concordancia con variables asociadas al ciclo del carbono en el océano. Se llevaron a cabo 2 experimentos idealizados con el fin de explorar el rendimiento del modelo. Primero, se forzó el modelo variando el transporte de Ekman en el Océano Austral, imitando el efecto de las variaciones de los vientos del oeste del Hemisferio Sur (HS), y segundo, se impusieron pulsos de derretimiento de agua dulce de Antártica sobre la plataforma continental del Océano Austral. Los cambios en la circulación oceánica y en el ciclo global del carbono coinciden con resultados de modelos mucho más complejos. Por lo tanto, consideramos que DCESS II es una herramienta útil y fácil de usar para realizar simulaciones de climas pasado, así como también para proyecciones del sistema terrestre.

Cuando el nuevo modelo de Sistema Tierra, DCESS II, es usado para estudiar la Transición del Pleistoceno Medio (MPT), se proponen cuatro forzamientos de manera de explicar el fuerte enfriamiento global observado a través de MPT: 1. Intensidad y posición de los vientos del oeste en el HS, 2. Exporte de hielo marino y icebergs desde la plataforma Antártica, 3. Fertilización del Océano Austral por polvo y 4. Avance de los mantos de hielo continental en el HN. Encontramos que el debilitamiento y desplazamiento hacia el ecuador de los vientos del oeste en el HS y el incremento en el exporte de hielo marino y icebergs desde la plataforma Antártica, pueden explicar gran parte del fuerte enfriamiento durante MPT. Las simulaciones sugieren que estos cambios provocaron el enfriamiento al reducir el intercambio de calor y de carbono entre las capas superiores y profundas del Océano Austral, y por medio del aumento de la recirculación en el océano profundo, lo que condujo al aislamiento de éste, al almacenamiento de carbono y a la disminución de CO₂ en la atmósfera. La fertilización con hierro impulsada por el polvo reforzó aún más este almacenamiento y reducción, mientras que el crecimiento de la capa de hielo en el HN contribuyó principalmente al enfriamiento regional, al tiempo que promovió la reducción de la biomasa terrestre que libera CO₂ a la atmósfera.

1. INTRODUCTION

The Earth's climate system is a complex structure formed by dynamic interactions among the atmosphere, hydrosphere, cryosphere, biosphere and lithosphere. These components work in concert to maintain equable climate over large timescales helping to sustain life. In a long-term view, global climate over the Earth's history has followed a complex evolution passing through both extremely warm and cold periods with climate conditions quite different from today (Pierrehumbert et al., 2011). Some of such periods have had such profound effects on the Earth System as to lead to extensive mass extinctions (Bambach, 2006). All of these deep-time events share a common feature: global-scale perturbations of biogeochemical cycles operating on different time scales and interrelated in complex and subtle ways. One of these global cycles is the carbon cycle, the backbone of the climate system since it acts as a main regulator of global mean temperature via the atmospheric concentration of carbon dioxide (Sarmiento and Gruber, 2006).

1.1. The global climate carbon cycle

This cycle may be considered to be composed of two domains. One domain is a fast one with large exchange fluxes and relatively "rapid" reservoir turnovers (from years to thousands of years). This domain encompasses carbon in the atmosphere, ocean, superficial (bioturbated) ocean sediments and on land in vegetation, soil and freshwater. A second, slower domain (from hundreds of thousands to millions of years) consists of huge carbon stores in rocks and sediments that exchange carbon with the fast domain through volcanic emissions of carbon dioxide (CO₂), chemical weathering, erosion and sediment formation on the sea floor. How this carbon is partitioned between the different Earth's reservoirs is what sets the content of CO₂ in the atmosphere. In the following, both the short-term and the long-term domains are briefly explained.

Every year, a fraction of the biomass produced in the sunlit surface ocean sinks into the dark ocean interior before being decomposed, thereby "pumping" both nutrients and carbon into the deep ocean where carbon is sequestered away from the atmosphere and the nutrients cannot be immediately used to fuel new production of biomass. The original definition of the "biological pump" (Volk and Hoffert, 1985) emphasizes the importance of the biological sinking flux on

the distribution of carbon in the ocean. This depletes the surface ocean in carbon relative to the ocean interior. There are actually two biological pumps, one for soft tissue and the other for carbonate. The first pump results from the conversion of dissolved inorganic carbon (DIC) to organic carbon by autotrophic organisms in the lighted surface ocean, while the second pump is carried out by organisms that synthesize carbonates, primarily calcium carbonate (CaCO_3), to form hard exoskeletons (e.g., coccolithophores and foraminifera). The summed effect of these two pumps is to remove DIC from the surface and release it into the deeper water column (DeVries, 2022). As only the surface ocean can exchange carbon with the atmosphere, the sequestration of organic carbon at depths results in a lower partial pressure of CO_2 ($p\text{CO}_2$) of the surface waters, thus also lowering atmospheric CO_2 . At any given time, only a small fraction (~10%) of the carbon in the ocean can be said to be sequestered by the action of the biological pump. However, given the much greater size of the ocean carbon reservoir, even a small change in the amount of deeply sequestered carbon can have a substantial impact on the atmospheric CO_2 inventory (Hain et al., 2014).

The vast majority of organic matter (OM) exported from near-surface waters is converted back into its inorganic constituents by heterotrophic organisms within the water column and/or sediments, a process referred to as remineralization. Similarly, the exoskeletons are subject to dissolution as they sink into the deep ocean and reach ocean sediments, returning calcium and carbonate to the water column and/or pore-water sediments. However, this process is controlled by environmental conditions like pressure and sea-water chemical composition, unlike biotic OM remineralization. Significant spatial differences exist in the deposition of OM and CaCO_3 in marine sediments. While OM burial is highest in coastal environments, CaCO_3 predominantly accumulates in open-ocean sediments, where about half of the CaCO_3 leaving the surface reaches the seafloor and about one-third of this is ultimately buried. In contrast, nearly 95% of exported OM is remineralized within the water column, with only a minor fraction preserved and buried in open-ocean sediments (Canfield, 1993; Sarmiento and Gruber, 2006).

Sediment pore-water composition can be altered by remineralization of organic matter and dissolution of CaCO_3 . These biological and chemical processes create large concentration gradients between the pore-water and the overlying seawater, resulting in diffusion of solutes to and from the overlying water column (Bernier, 1980). Burial of organic matter and CaCO_3

removes carbon from the short-term carbon cycle and incorporates it into the long-term carbon cycle. Large-scale ocean circulation redistributes carbon (among other elements) and plays a significant role by adding (removing) carbon to (from) the atmosphere. For example, the upward flux in upwelling zones brings remineralized inorganic nutrients and carbon to the surface, thereby helping to close the cycling loop driven by the biological pump and eventually releasing carbon to the atmosphere.

The land biosphere stores carbon in vegetation and soil and interacts with the atmosphere through spatially heterogeneous fluxes from daily to multidecadal time-scales. The largest carbon stocks are held in aboveground biomass and soils in tropical and high latitude forests, respectively (Chapin III et al., 2011). Changes in environmental conditions can alter land ecosystems, driving shifts in carbon fluxes (alongside other elements) due to modifications in primary production and/or soil remineralization rates (Crisp et al., 2022). Primary production removes CO₂ from the atmosphere at a rate that increases with atmospheric *p*CO₂ itself (Chen et al., 2022; Saugier et al., 2001), while soil remineralization rates are enhanced by rising temperatures (Davidson and Janssens, 2006; Frey et al., 2013). Additionally, shifts in climate conditions can cause certain vegetation types to expand or retreat, altering the terrestrial biomass budget and, consequently, the amount of carbon stored in vegetation (Ciais et al., 2012). Furthermore, variations in permafrost extent during glacial-interglacial conditions can significantly influence atmospheric CO₂ concentrations, thereby impacting the global carbon cycle (Jones et al., 2023; Tesi et al., 2013).

The long-term carbon cycle involves the movement of carbon between the Earth's surface and its interior, controlled primarily through processes such as continental weathering, ocean sedimentation and volcanic activity. Carbon dioxide is removed from the atmosphere mainly from weathering of silicate and carbonate rocks, a process that forms bicarbonate ions which are transported to the surface ocean by rivers. In the marine environment, these ions combine with calcium to form CaCO₃. In the modern ocean, most of the calcium carbonate is made by calcifying organisms. After organisms die, they sink to the ocean floor and eventually accumulate in ocean sediments where, if they are not subject to dissolution, they are buried. Over geological timescales, carbon-rich, deep-ocean sediments are subducted into the Earth's mantle through tectonic processes in subduction zones, during which they are subject to high

temperature and pressure processes. This drives chemical reactions that release some carbon from the subducting slab, transferring it to buoyant fluids and eventually back to the Earth's surface for release at arc volcanoes (Manning, 2014). In this way, carbon, aerosols and other elements may eventually return to the atmosphere via volcanic eruptions.

The interplay between tectonics, weathering, and volcanic activity has historically maintained a balance in the carbon cycle, ensuring relatively-stable climate conditions over geological epochs. An example is the observed long-term global cooling over the whole Cenozoic (Westerhold et al., 2020; Zachos et al., 2001). However, this balance can be disrupted by significant geological events when both life and the environment evolved dramatically. One such example is the Paleocene-Eocene Thermal Maximum (~56 million years ago (Ma)) associated to a rapid and massive, ^{13}C -depleted carbon inputs to the ocean-atmosphere system (Pagani et al., 2006; Zachos, 2008).

Figure 1.1 show records of the climate evolution for the last 4.5 million years. Panel A shows measurements of benthic $\delta^{18}\text{O}$ that reflects a combination of local water temperature and ^{18}O content of sea-water, with the latter largely recording land-ice volume and thus sea level (Clark et al., 2024). During 2.5 million years (from 4 to 1.5 Ma), the Earth experienced a long-term global cooling (Figure 1.1C,D) accompanied by a slow decrease in the atmospheric content of CO_2 (Figure 1.1B), probably associated to increased continental weathering rates (Bayon et al., 2023; Chiang et al., 2024; Martin et al., 2023).

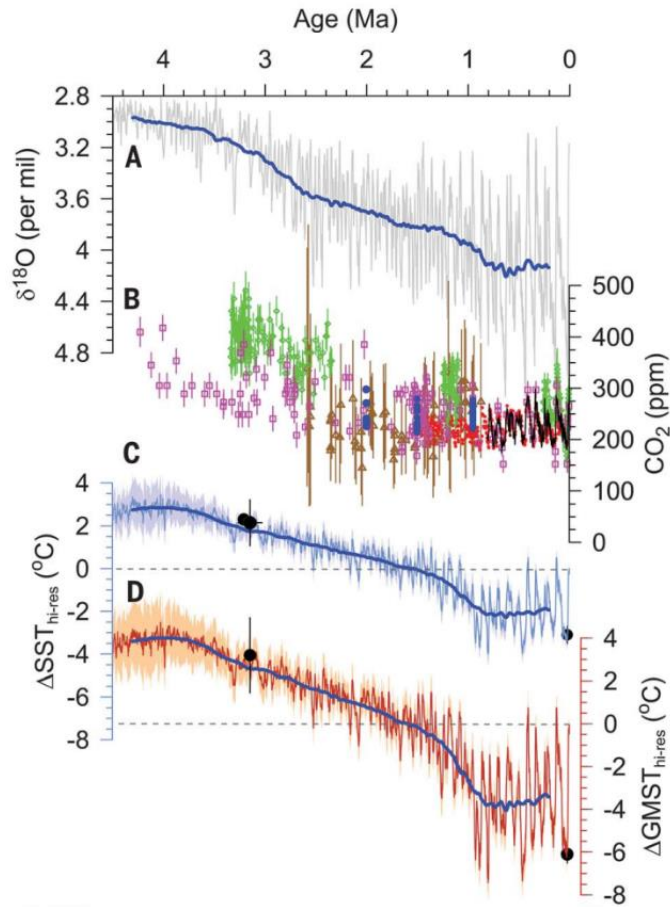


Figure 1.1: Proxy-records over the past 4.5 Myr. (A) Benthic $\delta^{18}\text{O}$ record in gray with 400 kyr running average in blue (1 kyr = 1,000 years). **(B)** Proxy and ice-core CO_2 data. **(C)** Global Sea Surface Temperature (SST) change (light blue with 1σ uncertainty and long-term averaged in dark blue) referenced to the pre-industrial (PI). **(D)** Global mean surface temperature changes (red with 1σ uncertainty and long-term average in blue) referenced to the PI. Adapted from Clark et al., (2024).

This slow trend culminates at approximately 1.5 Ma with intensified global cooling, coinciding with a transition period characterized by significant changes in both the amplitude and periodicity of temperature and land ice volume oscillations, as evidenced by $\delta^{18}\text{O}$ records (Figure 1.1A). This marks the onset of the Middle Pleistocene Transition (MPT), a ~ 700 -kyr interval (1.5-0.8 Ma) during which Earth's climate cycles shifted from 40-kyr to dominant 100-kyr glacial-interglacial cycles (Clark et al., 2006; Elderfield et al., 2012; Lisiecki and Raymo 2005). The pronounced global cooling during this period represents one of the main focuses of this study.

1.2. The Middle-Pleistocene Transition

The MPT was a period of strong global cooling following million years of weaker cooling (Lisiecki & Raymo, 2005, Westerhold et al., 2020). Before the MPT, glacial-interglacial cycles were relatively symmetric and weak, whereas after the MPT cycles were stronger and more asymmetric with longer glacial and shorter interglacial periods (Medina-Elizalde and Lea, 2005; von der Heydt et al., 2021). Evidence shows that MPT occurred in absence of any appreciable astronomical forcing change, pointing toward explanations attributed to feedbacks and internal changes in the Earth's climate system (Herbert, 2023; Ruddiman et al., 1986). Proposed mechanisms include Northern Hemisphere bedrock and regolith erosion beneath the ice sheets, gradual atmospheric CO₂ decline, Antarctic Ice Sheet expansion, and deep ocean circulation reorganization (An et al., 2024; Clark et al., 2006; Raymo et al., 2006; Tziperman and Gildor 2003; Willeit et al., 2019).

A major change across the MPT was the expansion of Northern Hemisphere (NH) ice sheets (Ao et al., 2023; Lisiecki & Raymo, 2005; Batchelor et al., 2019), which helped merge them and enable them to survive insolation maxima and reach continental scales (Bintanja & van de Wal, 2008). Larger ice sheets promoted feedbacks like increased surface albedo and adiabatic cooling with increasing height, leading to further growth (Berends et al., 2021; Clark and Pollard, 1998). Furthermore, larger NH ice sheets become more susceptible to mechanisms favoring longer, asymmetrical ~100 kyr cycles like bedrock depression and calving (Abe-Ouchi et al., 2013, Clark and Pollard, 1998). Whatever combination of processes are evoked to explain MPT ice age cycle lengthening, such strong MPT cooling likely preconditioned the system for such cycle lengthening by, for example, driving NH ice sheet expansion.

1.3. Earth System Models

In order to study complex, multi-scale climate system interactions like those mentioned above, scientists have developed a new type of climate model known as an Earth System Model (ESM). The ESMs are advanced computational tools designed to provide a comprehensive understanding of how the Earth works as a system of interdependent parts. These models integrate a wide range of physical, chemical, and biological processes across the different Earth system components, involving, generally, contributions from many scientists and many areas of

science (Flato 2011). ESMs go beyond the scope of their predecessors, Global Climate Models (GCMs), as one of the key strengths of ESMs is their ability to incorporate feedback mechanisms resulting from all its interactions (Heinze et al., 2015; Pan et al., 2025). Depending on their purpose, these models can vary significantly in complexity and, subsequently, in the time and the computational resources used to run modelled experiments.

With the recent emergence of the Earth System Science approach (Steffen et al., 2020), ESMs have become essential tools for projecting climate responses under current global warming scenarios. Ongoing scientific efforts continue to enhance ESMs accuracy and reliability, and these models remain the most powerful instruments for both projecting future climate change and informing policymakers, despite their inherent limitations (Prinn, 2013).

This study investigates the global climate-carbon cycle dynamics driving the observed strong cooling during the Middle Pleistocene Transition (MPT) using the new Earth System Model DCESS II (Fernández and Shaffer, 2025). Chapter 2 presents the hypotheses and objectives, while Chapter 3 details the model framework and experimental design. Results are presented in Chapter 4, with findings discussed in Chapter 5 and key conclusions outlined in Chapter 6.

2. HYPHOTESSES AND SPECIFIC GOALS

2.1. Hypotheses

Hypothesis 1: Mid- and high-latitude Southern Hemisphere ocean-atmosphere coupled processes are the main drivers in the evolution of the global climate-carbon cycle during MPT.

Hypothesis 2: Equatorward migration of Southern Hemisphere westerly winds combined with increased sea ice and iceberg export from Antarctic shelf explains much of the strong MPT cooling by way of decreased heat and CO₂ exchange between the upper and deep Southern Ocean and increased deep ocean isolation and carbon storage.

2.2. Specific Objectives

Objective 1: Develop a new version of the DCESS model (Shaffer et al., 2008) to be known as the DCESS II model. Key features of the new model include two hemispheres, improved spatial and temporal resolution, dynamic formulation for large-scale ocean circulation, a realistic formulation for the Antarctic Bottom Water formation, a new land biosphere module, and improvements in the treatments of ocean biogeochemical cycles and sea ice.

Objective 2: Model the global climate-carbon cycle change across the MPT using the new Earth System model DCESS II, evaluating potential climate forcings in order to explain the observed global cooling during this transition period.

3. METHODOLOGY

The methodology to address each specific objective proposed above is summarized in the following subsections. The new model is first briefly described, and then the approach used to simulate the MPT is presented.

3.1. A new Earth System model

A new Earth System model of intermediate complexity is created, that builds upon, improves and extends the Danish Center for Earth System Science (DCESS) Earth System model (Shaffer et al., 2008). As its predecessor (DCESS I), DCESS II contains modules of atmosphere, ocean, ocean sediment, land biosphere and lithosphere and is designed to deal with global climate simulations on scales of years to millions of years with no need for large computational resources. In the following, features of the new model are described.

3.1.1. Model geometry

The model geometry has been extended to include two hemispheres with a present-day continental distribution and ocean depth distribution as shown in Figure 3.1.

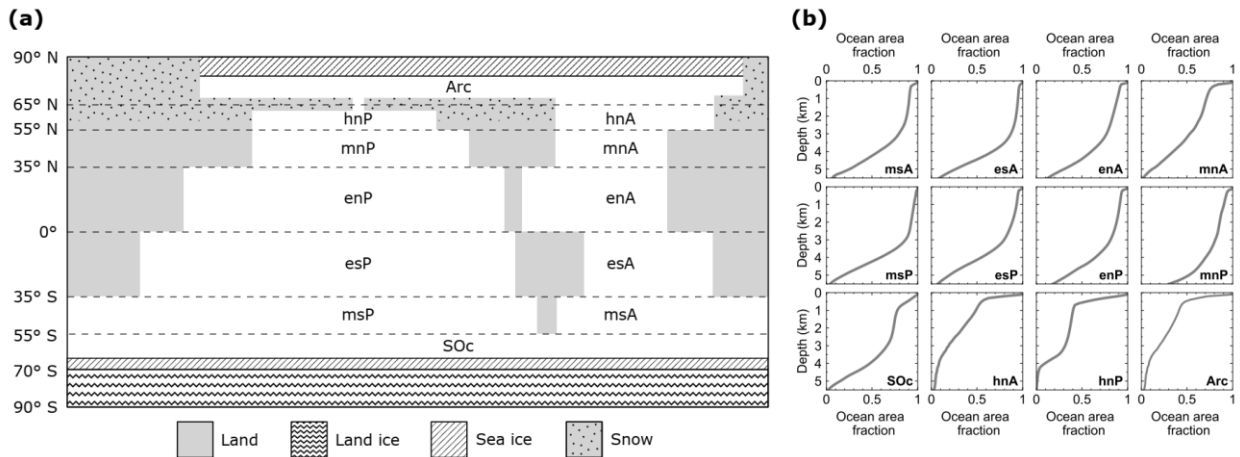


Figure 3.1: (a) Pre-industrial model land continental distribution and meridional boundaries of ocean sectors (dashed lines). There are twelve ocean sectors with their respective identifiers: Arc: Arctic Ocean, Soc: Southern Ocean, hn: high north, mn: mid north and en: equatorial north for Atlantic (A) and Indian-Pacific (P) Ocean. Sector names in the Southern Hemisphere follow

the same convention. High latitude North Pacific sector (hnP) and the Arctic Ocean are connected through the Bering Strait. Land south of 70° S is fully ice covered. Meridional sea ice and snowline extents vary freely. **(b)** Observed present-day ocean area fraction profile of each ocean model sector calculated from Amante and Eakins (2009).

The atmosphere module considers three zonally-averaged boxes per hemisphere as low-, mid-, and high-latitude sectors divided at 35° and 55° north and south latitudes (Figure 3.2a). In the ocean module an extra division at 65° N is included to allow consideration of four global ocean basins (Atlantic, Indian-Pacific, Arctic and Southern Ocean). The Southern Ocean is 360° wide and extends down to 69° S, where it interacts with an ocean shelf extending to 70° S. In total, there are 12 ocean sectors (compared to only 2 in previous DCESS model version). Each ocean sector is divided into 55 vertical layers with 100 m vertical resolution reaching 5500 m depth where each layer has an associated sediment segment (Figure 3.2b). For each sector, ocean layer and ocean sediment areas are determined from observed ocean depth distributions (Figure 3.1b).

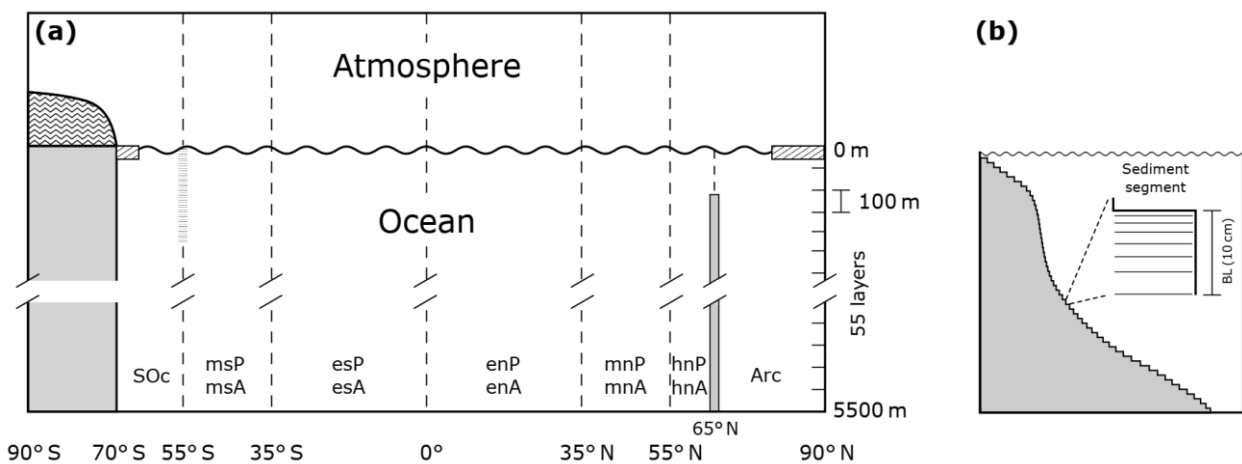


Figure 3.2: **(a)** Ocean-atmosphere cross-section view depicting meridional distributions of ocean and atmospheric boxes. There are six zonal-averaged atmospheric boxes and twelve ocean sectors (see also Fig. 1a). The shaded vertical bar at 55° S extending from the surface to 2000 m depth is a virtual barrier against meridional geostrophic flow above the Drake Passage sill depth. The vertical barrier at 65° N extending from the bottom up to 1000 m depth is a physical barrier associated with Denmark Strait bathymetry. **(b)** Sketch of an idealized vertical area profile for an ocean sector (the actual profile for each sector is based on bathymetry observations; see Fig. 1b). Also shown is an idealized sediment segment contained in a 100 m thick box layer (the area of each specific segment is again based on bathymetric observations). The bioturbated layer (BL) is assumed to be 10 cm thick and is divided into seven sublayers as shown.

The continental distribution shown In Fig. 3.1a can be relatively straightforward modified as needed depending on the climate stage to be studied. In the next section, main features of each model module are described.

3.1.2. Module descriptions

Atmospheric module

The tracers considered in this module are temperature, nitrous oxide, methane ($^{12,13}\text{C}$ isotopes), carbon dioxide ($^{12,13,14}\text{C}$ isotopes) and atmospheric oxygen. Temperature is modelled using a zonally integrated energy balance model forced by seasonally varying insolation, heat exchange with the ocean surface, and meridional heat transport. Atmospheric gases are forced by air-sea gas exchange, meridional transport between adjacent boxes, and sources/sinks within the atmosphere or net transports to or from the atmosphere via weathering, volcanism, and interaction with land biosphere. In combination with simple sea ice and snow parameterizations, the model includes the ice-snow albedo feedback and the insulating effect of sea ice. Sea ice is modelled by implementing the simple dynamical formulation according to Olsen et al. (2005) for the seasonal, equatorward sea ice extent. This approach gives sea ice rates of advance and retreat taking advantage of meridional profile of atmospheric temperature and sea surface temperature. Changes in sea ice line position are determined individually for the Arctic-North Atlantic, North Pacific and Southern Oceans. Snow line responds instantaneously to atmospheric temperature changes. Furthermore, present-day Northern Hemisphere ice sheets are prescribed as a constant area with ice albedo throughout the year independent of the snow line position.

Ocean module

Tracers of the ocean module are conservative temperature, absolute salinity, phosphate (PO_4), dissolved oxygen (O_2), dissolved inorganic carbon (DIC) in $^{12,13,14}\text{C}$ species, alkalinity (ALK), and sea-water oxygen-18 ($\delta^{18}\text{O}_w$). Conservation of any ocean tracer is given by an advection-diffusion equation plus terms associated with air-sea exchange of heat and gases, exchange of dissolved substances with the ocean sediment, and internal sources and sinks into the water column. Large-scale ocean circulation is based on a dynamical approach consisting of a balance between the pressure gradient force and the linear friction acting on the meridional velocity.

Horizontal mixing is parameterized by a depth-dependent horizontal diffusivity, while vertical mixing is modelled using a stratification-dependent form. There is a prescribed northward volume flux in the surface layer at 55° S to account for Ekman transport, forced by prevailing westerly winds, as well as a prescribed northward flow at 65° N from the North Pacific to the Arctic Ocean through the Bering Strait. An observation-based, formation process of Antarctic Bottom Water (AABW) is implemented following a gravity-current approach including Antarctic shelf water production and mixing by entrainment as an AABW plume flows down the Antarctic slope (Baines, 2005, 2008; Gordon, 2019; Orsi, 2002). Southern Ocean shelf tracers are forced by freshwater input from melting, calving and precipitation, export of sea ice and icebergs out of the shelf, influx from the Southern Ocean, and gas exchange. Shelf temperature is held constant at its freezing point due to air-sea heat exchanges there.

New (exported) production (NP) of organic matter is modelled using a Michaelis–Menten approach dependent on surface phosphorus (Maier-Reimer, 1993; Yamanaka and Tajika, 1996) and solar radiation. A limitation factor for NP is applied to the Arctic and the Southern Ocean to account for effects like dust fertilization. Surface (export) production of biogenic calcite is related to the new production by the “rain” ratio according to Maier-Reimer (1993) and Marchal et al., (1998) but with the addition of a dependence on temperature and the calcite saturation state of the ocean surface layer following Shaffer et al., (2016). Organic matter remineralization rate is modelled following an exponential-type law for the vertical fraction of both, particulate organic matter “nutrient” and “carbon” components plus a local temperature dependence. Calcite dissolution follows a simple exponential law with a constant e-folding length.

Sediment module

The sediment module is adopted from DCESS I model (Shaffer et al., 2008) but now applied to the multiple ocean regions. Each ocean layer is assigned a sediment segment composed of calcite, non-calcite mineral and reactive organic matter. The segment is a bioturbated layer (BL) of 10 cm thick divided in 7 sublayers. Sediment segment areas are determined by model topography. This module address calcium carbonate dissolution and (oxic and anoxic) organic matter remineralization by calculating concentrations of reactive organic carbon, pore-water O₂ and pore-water CO₃²⁻ for each sediment sublayer. To account for the role of benthic fauna, the bioturbation rate is parameterized to depend on organic carbon rates but also to consider

attenuation associated with very low dissolved oxygen concentrations. From sedimentation velocity, burial rates of phosphorus, organic carbon and carbonate carbon down and out of the base of the BL are determined. This module provides fluxes between ocean and sediment layers of PO_4 , O_2 , DIC and ALK based on concentrations of these tracers in each respective adjacent ocean layer and sediment pore-water concentrations from organic matter remineralization and calcium carbonate dissolution.

Land biosphere module

This module considers three different, dynamically varying vegetation zones per hemisphere. A grassland-desert zone bordered equatorward and poleward by tropical forest and extratropical forest zones, respectively. These zones are based on definitions of Eichinger et al., (2017) but applied to Northern and Southern Hemispheres. Latitudinal boundaries of the zones are defined as functions of atmospheric temperature alone, encompassing implicit dependency on precipitation. This three-zone approach captures the way the biosphere influences radiative forcing, since albedo is higher for grasslands-deserts than for forests (Bonan, 2008). Each vegetation zone includes carbon ($^{12,13,14}\text{C}$ isotopes) reservoirs for leaves, wood, litter and soil. Net primary production on land takes up atmospheric CO_2 and is forced by seasonally-varying solar radiation. Biotic activity in soil is dependent on atmospheric temperature. For each vegetation zone there are land biosphere-atmosphere fluxes of $^{12,13,14}\text{CO}_2$ and N_2O . Emissions of $^{12,13,14}\text{CH}_4$ are assumed to come only from wet areas, i.e. the forest zones.

Lithosphere module

This module follows the approach as in DCESS I model (Shaffer et al., 2008), but extended to include a global continental configuration, and distributions of river mouths and volcanoes. It considers carbonate and silicate weathering, lithospheric outgassing and river input of phosphorus and carbon species. Weathering rates of rocks containing phosphorus, as well as carbonate and silicate weathering rates are taken to depend on deviations of mean atmospheric temperature from its pre-industrial value and include a temperature sensitivity factor for weathering rates (Q_{10}). Silicate and carbonate weathering supply bicarbonate ion by way of rivers to ocean surface layers, modifying DIC and ALK concentrations there. Rivers also supply phosphorus, affecting ocean phosphate content. Silicate and carbonate weathering are sinks of carbon from the atmosphere, while weathering of rocks containing old organic carbon and

volcanism are sources of carbon to the atmosphere. The total river inputs are distributed among the 12 ocean sectors according to the river mouth distributions. Model configuration of rivers and volcanoes follow the present-day distribution but can be easily modified as needed.

3.1.3. Solution, calibration and validation procedure

Prognostic equations for atmosphere, land biosphere, lithosphere and the ocean modules are solved simultaneously using a fourth order Runge-Kutta algorithm with a two-week time step. Prognostic equations for the ocean sediment are solved by simple time stepping with a one-year time step. The complete coupled model is written in Fortran language and runs at a speed of about 10,000 years of simulation per 30 minutes of computer time on a high-end personal computer. The calibration procedure consists of six steps, all of them fully described in Fernández and Shaffer (2025), taking the pre-industrial time as the baseline with a climate sensitivity of 3°C per doubling atmospheric CO₂. Finally, components of the steady-state model solution are compared against observed data from the present-day, and two simple experiments are carried out in order to test the model performance.

3.2. Long-term simulations and the MPT

Using the model briefly described above and fully presented in Fernández and Shaffer (2025), attempts are made in order to reproduce the long-term, slow global cooling from 4 Ma until about 1.5 Ma followed by a stronger cooling across de MPT until about 0.8 Ma. For this purpose, some modifications were made in the original DCESS II model version as detailed below.

First, the model is recalibrated with a new pre-industrial steady state with a new equilibrium climate sensitivity of 5°C per doubling atmospheric CO₂. This recalibration proved to be necessary to achieve initial conditions at 4 Ma indicated by observations. Second, inflow from the Southern Ocean onto the Antarctic continental shelf is now implemented as an inflow at the shelf edge (500 m depth), rather than as a uniform inflow across the 0 – 500 m depth range. Third, under non-pre-industrial conditions, the originally fixed total freshwater forcing of the Southern Ocean shelf from precipitation, calving, and ice melting, is now taken as a time-dependent function of the annual mean atmospheric freshwater flux crossing 55°S. Fourth, the factor Q₁₀ (see above) has been now reduced from 2 to 1.5 increase for a 10 °C increase in

atmospheric temperature. This recalibration proved necessary to capture the long-term, slow global cooling from 4 Ma until about 1.5 Ma.

From this new PI steady-state, model initial conditions at 4 Ma are derived. For this, estimations of ocean calcium content and ocean carbon dissociation constants at that time are included (Zeebe and Tyrrell, 2019), and model weathering rates of carbonate, silicate, old organic carbon and phosphate are adjusted in order to achieve a long-term steady-state balance with model ocean sediment burial of calcium carbonate and organic matter for an atmospheric CO₂ concentration of 400 ppm, as indicated by proxy reconstructions (Bartoli et al., 2011; Köhler, 2023, LaRiviere et al., 2012; Sosdian et al., 2018). An alternative would have been to increase lithosphere outgassing as in other, related work (Willeit et al., 2019) but the present approach is focused on weathering, which is thought to control long-term cooling over the Pliocene-Pleistocene (Bayon et al., 2023; Chiang et al., 2024; Martin et al., 2023). At this point, model weathering formulation is expanded to include a time-dependent, weatherability factor representing non-temperature-dependent weathering changes due to factors like mountain building.

From this 4 Ma initial steady-state, and using prescribed time evolution of ocean calcium content and ocean carbon dissociation constants (Zeebe and Tyrrell, 2019), and incorporating the time-dependent orbital forcing from Berger and Loutre (1991), parameters in the model weathering formulation are tuned until the simulation reproduces the observed, uniform global mean SST decrease from 4 to 1.5 Ma (Figure 1c). From this point until 0.8 Ma, additional processes are included that are thought to have probably contributed to the observed acceleration in global cooling. The proposed forcings are:

1. Northward Ekman transport in the Southern Ocean, driven by shifts in the strength and latitudinal position of the Southern Westerly Winds (SWW).
2. Sea ice and iceberg export from the Antarctic shelf, which influences the Antarctic shelf water and, consequently, Antarctic Bottom Water formation.
3. Dust fertilization of the Southern Ocean, enhancing marine productivity there.
4. Equatorward extent of Northern Hemisphere ice sheets, affecting albedo and land biomass.

Assumptions about these forcings during MPT are:

1. The pre-existing trend of the weatherability factor is continued across the MPT as the simplest assumption with no expected, climate-related impact on it.
2. Influence of the SWWs extended to include possible Ekman transport across 35°S. Weakened and northward shifted SWWs would be expected across cooling intervals like the MPT (Toggweiler et al., 2006; Anderson et al., 2009; Venugopal et al., 2023).
3. Increased sea ice production and export from the Antarctic shelf as well as increased iceberg export/less Antarctic meltwater there in connection with MPT cooling (Shin et al., 2003; Starr et al., 2021).
4. Dust deposition and associated Southern Ocean fertilization are assumed to increase due to a drier climate and northward-shifted SWWs exposing more continental dust sources (Shaffer and Lambert, 2018; Martinez-Garcia et al., 2011; Lamy et al., 2014).
5. Northern Hemisphere ice sheets grew and expanded equatorward across the MPT as shown in geological reconstructions (Ao et al., 2023; Hodell and Channell, 2016).

Finally, based on the structure of the observed SST transition during MPT (Figure 1c), these forcings are prescribed to evolve linearly in two time-steps: from 1.5 to 1.2 Ma and from 1.2 to 0.8 Ma, accounting for a 10% and 90% of the total forcing respectively. For simplicity, these four forcings are held constant at their PI values (Fernández and Shaffer, 2025) before 1.5 Ma and at their 0.8 Ma values from 0.8 Ma to the present. Although post-0.8 Ma period is also simulated, this is only for completeness purposes and is not discussed further in this work.

4. RESULTS

4.1. Chapter 1: “Presentation, calibration and testing of the DCESS II Earth system model of intermediate complexity (version 1.0)”. Geoscientific Model Development, DOI: <https://doi.org/10.5194/gmd-18-2161-2025>.

Abstract

A new Earth system model of intermediate complexity, DCESS II, is presented that builds upon, improves and extends the Danish Center for Earth System Science (DCESS) Earth system model (DCESS I). DCESS II has considerably greater spatial resolution than DCESS I while retaining the fine, 100 m vertical resolution in the ocean. It contains modules for the atmosphere, ocean, ocean sediment, land biosphere and lithosphere and is designed to deal with global change simulations on scales of years to millions of years while using limited computational resources. Tracers of the atmospheric module are temperature, nitrous oxide, methane ($^{12,13}\text{C}$ isotopes), carbon dioxide ($^{12,13,14}\text{C}$ isotopes) and atmospheric oxygen. For the ocean module, tracers are conservative temperature, absolute salinity, water ^{18}O , phosphate, dissolved inorganic carbon ($^{12,13,14}\text{C}$ isotopes), alkalinity and dissolved oxygen. Furthermore, the ocean module considers simplified dynamical schemes for large-scale meridional circulation and sea ice dynamics, stratification-dependent vertical diffusion, a gravity current approach to the formation of Antarctic Bottom Water, and improvements in ocean biogeochemistry. DCESS II has two hemispheres with six zonally averaged atmospheric boxes and 12 ocean sectors distributed across the Indian–Pacific, the Atlantic, the Arctic and the Southern oceans. A new extended land biosphere scheme is implemented that considers three different vegetation types whereby net primary production depends on sunlight and atmospheric carbon dioxide. The ocean sediment and lithosphere model formulations are adopted from DCESS I but now applied to the multiple ocean and land regions of the new model.

Model calibration was carried out for the pre-industrial climate, and model steady-state solutions were compared against available modern-day observations. For the most part, calibration results agree well with observed data, including excellent agreement with ocean

carbon species. This serves to demonstrate model utility for dealing with the global carbon cycle. Finally, two idealized experiments were carried out in order to explore model performance. First, we forced the model by varying Ekman transport out of the model Southern Ocean, mimicking the effect of Southern Hemisphere westerly wind variations, and second, we imposed freshwater melting pulses from the Antarctic ice sheet on the model Southern Ocean shelf. Changes in ocean circulation and in the global carbon cycle found in these experiments are in line with results from much more complex models. Thus, we find DCESS II to be a useful and computationally friendly tool for simulations of past climates as well as for future Earth system projections.



Presentation, calibration and testing of the DCESS II Earth system model of intermediate complexity (version 1.0)

Esteban Fernández Villanueva¹ and Gary Shaffer²

¹Graduate Program in Oceanography, Department of Oceanography, Faculty of Natural Sciences and Oceanography, University of Concepción, P.O. Box 160-C, Concepción, Chile

²Niels Bohr Institute, University of Copenhagen, 2100 Copenhagen Ø, Denmark

Correspondence: Esteban Fernández Villanueva (estfernandez@udec.cl)

Received: 29 June 2024 – Discussion started: 22 August 2024

Revised: 2 December 2024 – Accepted: 23 January 2025 – Published: 8 April 2025

Abstract. A new Earth system model of intermediate complexity, DCESS II, is presented that builds upon, improves and extends the Danish Center for Earth System Science (DCESS) Earth system model (DCESS I). DCESS II has considerably greater spatial resolution than DCESS I while retaining the fine, 100 m vertical resolution in the ocean. It contains modules for the atmosphere, ocean, ocean sediment, land biosphere and lithosphere and is designed to deal with global change simulations on scales of years to millions of years while using limited computational resources. Tracers of the atmospheric module are temperature, nitrous oxide, methane (^{12,13}C isotopes), carbon dioxide (^{12,13,14}C isotopes) and atmospheric oxygen. For the ocean module, tracers are conservative temperature, absolute salinity, water ¹⁸O, phosphate, dissolved inorganic carbon (^{12,13,14}C isotopes), alkalinity and dissolved oxygen. Furthermore, the ocean module considers simplified dynamical schemes for large-scale meridional circulation and sea ice dynamics, stratification-dependent vertical diffusion, a gravity current approach to the formation of Antarctic Bottom Water, and improvements in ocean biogeochemistry. DCESS II has two hemispheres with six zonally averaged atmospheric boxes and 12 ocean sectors distributed across the Indian–Pacific, the Atlantic, the Arctic and the Southern oceans. A new extended land biosphere scheme is implemented that considers three different vegetation types whereby net primary production depends on sunlight and atmospheric carbon dioxide. The ocean sediment and lithosphere model formulations are adopted from DCESS I but now applied to the multiple ocean and land regions of the new model.

Model calibration was carried out for the pre-industrial climate, and model steady-state solutions were compared against available modern-day observations. For the most part, calibration results agree well with observed data, including excellent agreement with ocean carbon species. This serves to demonstrate model utility for dealing with the global carbon cycle. Finally, two idealized experiments were carried out in order to explore model performance. First, we forced the model by varying Ekman transport out of the model Southern Ocean, mimicking the effect of Southern Hemisphere westerly wind variations, and second, we imposed freshwater melting pulses from the Antarctic ice sheet on the model Southern Ocean shelf. Changes in ocean circulation and in the global carbon cycle found in these experiments are in line with results from much more complex models. Thus, we find DCESS II to be a useful and computationally friendly tool for simulations of past climates as well as for future Earth system projections.

1 Introduction

The carbon cycle is the backbone of the Earth's climate system since it acts as a main regulator of global mean atmospheric temperature via atmospheric concentration of carbon dioxide ($p\text{CO}_2$). This cycle may be considered to be composed of two domains. One domain is a fast one with large exchange fluxes and relatively "rapid" reservoir turnovers (from years to thousands of years). This domain encompasses carbon in the atmosphere, ocean and superficial (bio-turbated) ocean sediments and on land in vegetation, soil and

freshwater. A second slower domain (from hundreds of thousands to millions of years) consists of huge carbon stores in rocks and sediments that exchange carbon with the fast domain through volcanic emissions of CO₂, chemical weathering, erosion and sediment formation on the seafloor. How this carbon is partitioned between the Earth's different reservoirs is what sets the pCO₂ in the atmosphere.

Earth system models (ESMs) include one or both of these domains. They are thereby useful tools that can help us gain understanding of past climates as well as make future climate projections. Depending on their complexity and spatial resolution, ESMs can take days, weeks or even months to run model simulations on the range of timescales mentioned above while using substantial computational resources. The Danish Center for Earth System Science (DCESS) model (DCESS I; Shaffer et al., 2008) is a low-order ESM with a simple geometry and ocean physics that deals with both domains of the global-scale carbon cycle and is thereby suitable for investigating Earth system changes on scales of years to millions of years while taking only minutes to days to run. The DCESS I model has proven to be a useful tool in such studies as documented by many stand-alone or intercomparison study publications (e.g., Eby et al., 2013; Harper et al., 2020; Joos et al., 2013; MacDougall et al., 2020; Shaffer, 2010; Shaffer and Lambert, 2018; Shaffer et al., 2009; Zickfeld et al., 2013). Nonetheless, DCESS I has serious limitations when it comes to addressing many important Earth system problems, like glacial–interglacial cycles, due to its one-hemisphere, two-sector horizontal resolution; lack of ocean dynamics; lack of seasonal cycles; and simplified land vegetation scheme, among other factors. In order to address those deficiencies, here we present a new Earth system model, DCESS II, that contains great improvements in model geometry and physical–biogeochemical processes. This new model is able not only to capture relevant environmental differences between major ocean basins, but also, for example, to produce synthetic ocean sediment cores from distinct ocean zones for more detailed comparison with data, and this it can do while retaining much of the simplicity and the spirit of the DCESS I model. Thus, DCESS II is a simple, fast and highly flexible ESM of intermediate complexity that is well suited to running long-term experiments in a relatively simple way with no need for substantial computational resources.

This paper is organized as follows: in Sect. 2 we describe the modules of atmosphere, ocean, ocean sediment, land biosphere and lithosphere. In Sect. 3, we present the model solution and calibration procedure and show results for the model steady-state, pre-industrial simulation. In addition, we carry out two idealized experiments in order to explore and test model performance. Finally in Sect. 4 we discuss our results, outline future perspectives and present conclusions.

2 Model description

DCESS II is an intermediate-complexity Earth system model containing atmosphere, ocean, land biosphere, lithosphere and ocean sediment modules designed to deal with global climate simulations on scales of years to millions of years. It is an enhancement and extension of the original DCESS I model (Shaffer et al., 2008) and includes, for example, a much improved horizontal and time resolution as well as simplified ocean dynamics. Model geometry consists of two hemispheres with a land–ocean area distribution and ocean depth distribution as shown in Fig. 1.

The atmospheric module considers three zonally averaged boxes per hemisphere as low-, mid-, and high-latitude sectors divided at 35° (ϕ_{35}) and 55° (ϕ_{55}) north and south latitudes (Fig. 2a). In the ocean module we include an extra division at 65° N which allows us to consider four global ocean basins (Atlantic, Indian–Pacific, Arctic and Southern Ocean; for simplicity, hereafter the Indian–Pacific Ocean will be called only the Pacific Ocean). The Southern Ocean is 360° wide and extends up to 69° S, where it interacts with an ocean shelf extending to 70° S. In total, there are 12 ocean sectors (compared to only 2 in DCESS I). Each ocean sector is divided into 55 vertical layers with 100 m vertical resolution reaching 5500 m depth. An ocean sediment segment is assigned to each of the layers (Fig. 2b). For each sector, ocean layer and ocean sediment areas are determined from observed ocean depth distributions (Fig. 1b).

The land biosphere module considers three different types of vegetation per hemisphere whose latitudinal limits vary dynamically according to climate conditions. All model modules are described in detail in the following subsections.

2.1 Atmosphere exchange, heat balance and ice–snow extent

We use a simple, zonally integrated energy balance model for the near-surface atmospheric temperature, T_a (°C), forced by seasonally varying insolation, heat exchange with the ocean and meridional heat transport. In combination with simple sea ice and snow parameterizations, the model includes the ice–snow albedo feedback and the insulating effect of sea ice. Prognostic equations for mean T_a in the 0–35°, 35–55° and 55–90° zones ($T_a^{l,m,h}$) are obtained by integrating the surface energy balance over the zones as

$$\Lambda \frac{dT_a^{l,m,h}}{dt} = r^2 \int_0^{2\pi} \int_{\phi_{35}, \phi_{55}, \pi/2} \cos \phi d\phi d\xi \pm F^{\text{net}}, \quad (1)$$

where $\Lambda = A^{l,m,h} \rho_0 C_p b^{l,m,h}$, with $A^{l,m,h}$ denoting the atmospheric box areas, ρ_0 the reference density of water, C_p the specific heat capacity and $b^{l,m,h}$ the thicknesses chosen to yield observed seasonal cycles of $T_a^{l,m,h}$ (partially based

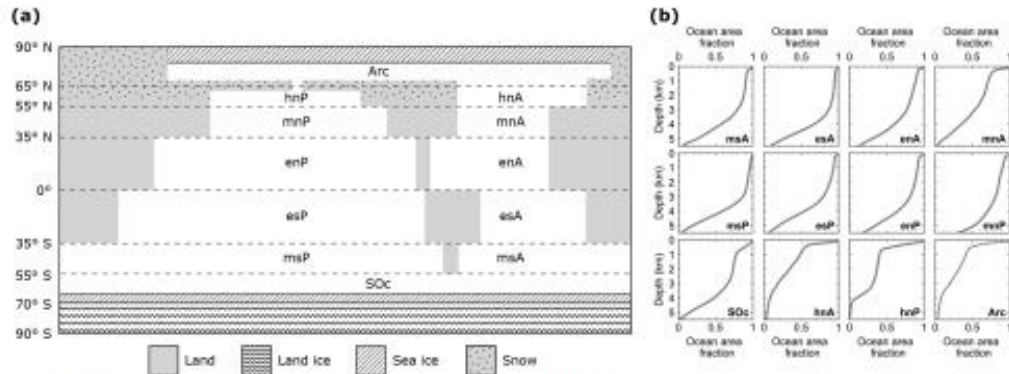


Figure 1. (a) Pre-industrial model land continental distribution and meridional boundaries of ocean sectors (dashed lines). There are 12 ocean sectors with their respective identifiers: Arc, Arctic Ocean; SOc, Southern Ocean; hn, high north; mn, mid-north; and en, equatorial north for the Atlantic (A) and Indian–Pacific (P) oceans. Sector names in the Southern Hemisphere follow the same convention. High-latitude North Pacific sector (hnP) and the Arctic Ocean are connected through the Bering Strait. Land south of 70° S is fully ice covered. Meridional sea ice and snow line extents vary freely. (b) The observed present-day ocean area fraction profile of each ocean model sector calculated from Amante and Eakins (2009).

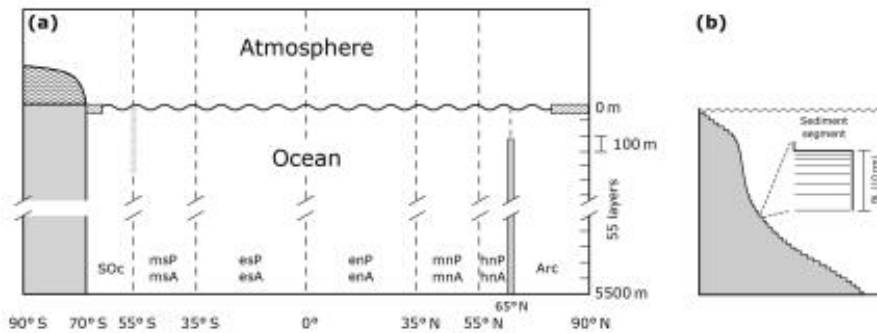


Figure 2. (a) Ocean–atmosphere cross-section view depicting meridional distributions of ocean and atmospheric boxes. There are six zonally averaged atmospheric boxes and 12 ocean sectors (see also Fig. 1a). The shaded vertical bar at 55° S extending from the surface to 2000 m depth is a virtual barrier against meridional geostrophic flow above the Drake Passage sill depth. The vertical barrier at 65° N extending from the bottom up to 1000 m depth is a physical barrier associated with Denmark Strait bathymetry. (b) Sketch of an idealized vertical area profile for an ocean sector (the actual profile for each sector is based on bathymetry observations; see Fig. 1b). Also shown is an idealized sediment segment contained in a 100 m thick box layer (the area of each specific segment is again based on bathymetric observations). The bioturbated layer (BL) is assumed to be 10 cm thick and is divided into seven sublayers as shown.

on Olsen et al., 2005), and r , ϕ and ξ are the Earth’s radius, latitude and longitude, respectively. Furthermore, F^{toa} and F^{T} are the vertical fluxes of heat through the top of atmosphere and the ocean surface, respectively, while F^{merid} corresponds to the loss (equatorward box) or gain (poleward box) of heat due to meridional transport across ϕ_{35} or ϕ_{55} . A no-flux boundary condition has been applied at the poles. At each point in time, we construct atmospheric temperature as a continuous function of latitude, $T_a(\phi)$, using a fourth-order

Legendre polynomial in the sine of latitude ϕ ,

$$T_a(\phi) = \sum T_n P_n(\sin \phi), \quad n = 2, 4, \quad (2)$$

where coefficients T_0 , T_2 and T_4 are determined by matching the area-weighted zone mean values of $T_a(\phi)$ to the prognostic mean sector values of $T_a^{j,m,h}$ in each hemisphere. Observations show that eddy heat fluxes in the mid-latitude atmosphere are much greater than advective heat fluxes there (Oort and Peixoto, 1983). By neglecting the advective heat fluxes, Wang et al. (1999) developed suitable expressions for F^{merid} and the associated moisture flux, E^{merid} , in terms of

T_a and $\partial T_a / \partial \phi$ at ϕ (for clarity we omit the index referencing low- to mid- and mid- to high-latitude boundaries, ϕ_{35} and ϕ_{55} , respectively):

$$F^{\text{merid}} = - \left[K_l + L_v K_q \exp(-5420T_a^{-1}) \right] |\partial T_a / \partial \phi|^{m-1} \partial T_a / \partial \phi, \quad (3)$$

$$E^{\text{merid}} = -K_q \exp(-5420T_a^{-1}) |\partial T_a / \partial \phi|^{m-1} \partial T_a / \partial \phi, \quad (4)$$

where K_l is a sensible heat exchange coefficient, K_q is a latent heat exchange coefficient and L_v is the latent heat of condensation ($2.25 \times 10^9 \text{ J m}^{-3}$). From observations, m is found to vary with latitude (Stone and Miller, 1980), and on this basis we take m to be 2.5 and 1.7 at ϕ_{35} and ϕ_{55} , respectively. The temperatures and temperature gradients entered in Eqs. (3)–(4) above are obtained from Eq. (2). The poleward freshwater flux crossing a latitude ϕ is evaporated from an equatorward ocean sector and drains into the respective poleward Atlantic, Pacific, Arctic or Southern Ocean basin/sector in accordance with observed land catchment areas (Rodríguez et al., 2011). In this way, each ocean sector receives a net freshwater flux from precipitation minus evaporation. The Arctic Ocean is an exception to this in as much as a fraction of E^{merid} crossing 55°N also drains there, emulating large northward-flowing rivers in Canada and Siberia. Furthermore, an atmospheric zonal transport of freshwater of 0.15 Sv ($1 \text{ Sv} = 10^6 \text{ m}^3 \text{ s}^{-1}$) is prescribed from the tropical North Atlantic sector to the tropical North Pacific sector, emulating the effects of trade winds there (Dey and Döös, 2020; Lohmann and Lorenz, 2000). All these fluxes force respective ocean sectors (see Sect. 2.3).

Based on a calibration procedure that makes use of monthly observed atmospheric temperature, we derived the following expression for interhemispheric heat transport at the Equator:

$$F^{\text{eq}} = K_l^{\text{eq}} \partial T_a / \partial \phi + 1.1 + \left[K_q^{\text{eq}} L_v \partial T_a / \partial \phi - 1.1 \right] \exp \left[-5420 \left(\frac{T_a^{\text{eq}^{-1}}}{T_a^{\text{PI}^{-1}}} - \frac{T_a^{\text{eq}^{-1}}}{T_a^{\text{PI}^{-1}}} \right) \right], \quad (5)$$

where K_l^{eq} and K_q^{eq} are sensible and latent heat coefficients and $\overline{T_a^{\text{eq}}}$ and $\overline{T_a^{\text{PI}}}$ are the model and observed pre-industrial atmospheric mean temperature at the Equator. For the $\overline{T_a^{\text{eq}}}$ calculation, Eq. (2) is used and evaluated at 0° latitude for the Northern Hemisphere and Southern Hemisphere. The heat flux at the top of the atmosphere is taken as the balance between shortwave and longwave radiation as follows:

$$F^{\text{toa}} = (1 - \alpha) Q - (A + BT_a), \quad (6)$$

where α is the planetary albedo, equal to 0.62 for ice and snow-covered areas and equal to $\alpha_0 - \alpha_2 (3 \sin^2 \phi - 1)$ otherwise. This formulation includes the effect of mean cloud cover and lower solar inclination at higher latitudes (Hart-

mann, 2016), and Q is the orbitally, seasonally and latitudinally varying (and if needed, paleo-time-varying) shortwave radiation (Berger and Loutre, 1991). The albedo of areas not covered by snow/ice varies with vegetation type since forested areas have lower albedo than non-forested areas (Bonan, 2008). We adopt the approach in Eichinger et al. (2017) that includes this effect by relating the α_0 factor to the vegetation type whereby $\alpha_0 = 0.3 - \gamma (1 - f(\delta T_a) / f_0)$, where the factor 0.3 is the present-day value of α_0 and γ is a multiplier equal to 0.02. $f(\delta T_a)$ is the ratio between the area of grassland–savanna–desert zone and the total area not covered by snow/ice as a function of δT_a , the deviation of atmospheric temperature from the present-day value (f_0 is the ratio at $\delta T_a = 0$; see Sect. 2.6 for details about vegetation zones). Finally, α_2 is equal to 0.0875.

The second term on the right-hand side of Eq. (6) is the outgoing longwave radiation (Budyko, 1969), where A and BT_a are the flux at $T_a = 0$ and the deviation from this flux, respectively. This simple formulation implicitly includes the radiative effects of changes in cloud cover and in atmospheric water vapor content. Greenhouse gas forcing is modeled by taking A to depend on deviations of (prognostic) atmospheric partial pressures of carbon dioxide, methane and nitrous oxide ($p\text{CO}_2$, $p\text{CH}_4$ and $p\text{N}_2\text{O}$) from their pre-industrial values (PI) such that

$$A = A_{\text{PI}} - (A_{\text{CO}_2} + A_{\text{CH}_4} + A_{\text{N}_2\text{O}}), \quad (7)$$

where expressions for A_{CO_2} , A_{CH_4} and $A_{\text{N}_2\text{O}}$ are taken from Byrne and Goldblatt (2014) and are valid for atmospheric concentrations in the range of 200–10 000 ppm for CO_2 and 0.1–100 ppm for CH_4 and N_2O . Overlap of the absorption by N_2O with CO_2 and CH_4 is included in these formulations. We take the year 1765 as our pre-industrial (PI) baseline, when values of $p\text{CO}_{2,\text{PI}}$, $p\text{CH}_{4,\text{PI}}$ and $p\text{N}_2\text{O}_{\text{PI}}$ were 280, 0.72 and 0.27 ppm, respectively, as indicated by ice-core data (IPCC, 2021, and citations therein). For simplicity and for the consideration of possible paleo-applications, we take constant values of A_{PI} and B for all atmospheric boxes (see Table 1). For each ocean sector, air–sea heat exchange is calculated according to Haney (1971) as

$$F^{\text{T}} = -L_o - \lambda (T_a^{\text{if}} - T_o), \quad (8)$$

where L_o is the direct (solar) heating of the ocean surface layer, taken to be 40, 20 and 0 W m^{-2} for the low-, mid- and high-latitude sectors, respectively; λ is a constant bulk transfer coefficient, as a good approximation taken to be $30 \text{ W m}^{-2} \text{ }^\circ\text{C}^{-1}$ but set to zero for areas covered by sea ice (Haney, 1971); T_a^{if} is the ice-free mean atmospheric temperature for each sector; and T_o is the zone mean ocean surface temperature of each ocean sector.

2.1.1 Sea ice and snow cover

Sea ice plays a pivotal role in the Earth's climate system, influencing radiative balance and thus global atmospheric tem-

Table 1. Atmosphere module parameters.

Parameter	Symbol	Value
Sensible heat exchange coefficient	$K_T (\phi_{eq}/\phi_{1m}/\phi_{mb})$	$2.40 \times 10^{15}/4.21 \times 10^{11}/3.30 \times 10^{12} \text{ J s}^{-1} \text{ }^\circ\text{C}^{-2.5}$
Latent heat exchange coefficient	$K_q (\phi_{eq}/\phi_{1m}/\phi_{mb})$	$-7.11 \times 10^5/1.56 \times 10^{10}/2.29 \times 10^{11} \text{ m}^3 \text{ s}^{-1} \text{ }^\circ\text{C}^{-2.5}$
Pre-industrial, longwave radiation for $T_a = 0 \text{ }^\circ\text{C}$	A_{PI}	206.58 W m^{-2}
Temperature sensitivity of longwave radiation	B	$2.21 \text{ W m}^{-2} \text{ }^\circ\text{C}^{-1}$
Inverse timescale for sea ice advance and retreat	Γ	$3 \times 10^{-2} \text{ s}^{-1}$
Ice–water heat exchange coefficient	κ_0	$150 \text{ W m}^{-2} \text{ }^\circ\text{C}^{-1}$

perature through its impact on surface albedo and air–sea heat exchange processes. For the sea ice cover, we take the same simple dynamical formulation as in Olsen et al. (2005) for the seasonal, equatorward sea ice extent. This formulation takes advantage of the meridional profile of T_a and assumes that (a) sea ice advance is proportional to the inverse timescale of cooling (τ^{adv}) of the ocean mixed layer to freezing temperature (T_f) by heat loss to the atmosphere and (b) that the retreat is proportional to the inverse timescale of melting (τ^{ret}) of seasonal sea ice cover. These inverse timescales are expressed as

$$\tau^{adv} = \frac{\lambda}{\rho_0 C_p d_m} \frac{T_a(\phi_i) - T_o}{T_o - T_f}, \quad (9)$$

$$\tau^{ret} = \frac{k_i}{\delta_i^2 \rho_i L_i} [T_a(\phi_i) - T_f] + \frac{\kappa_0}{\delta_i \rho_i L_i} [T_o - T_f], \quad (10)$$

where d_m is the mixed-layer depth (100 m); $T_a(\phi_i)$ is the atmospheric temperature at the sea ice edge; T_o is the ocean surface temperature; and k_i , δ_i , ρ_i , L_i and κ_0 are the thermal conductivity of ice ($2.0 \text{ W m}^{-2} \text{ }^\circ\text{C}^{-1}$), the sea ice thickness (2 m), the density of ice (917 kg m^{-3}), the latent heat of fusion of ice ($3.34 \times 10^5 \text{ J kg}^{-1}$), and the heat transfer coefficient between ice and water ($150 \text{ W m}^{-2} \text{ }^\circ\text{C}^{-1}$; Bendsen, 2002), respectively. Thus, changes in the sea ice line position are determined individually for the Arctic–North Atlantic, North Pacific and Southern Ocean as

$$\frac{\partial \phi_i}{\partial t} = -\Gamma (\tau^{adv} - \tau^{ret}), \quad (11)$$

where Γ is a free parameter that together with κ_0 has been chosen to match the observed seasonal amplitude and the annual mean position of sea ice cover, respectively. Land areas are covered by snow where $T_a(\phi) \leq 0 \text{ }^\circ\text{C}$ and are taken to respond instantaneously to atmospheric temperature changes. Furthermore, present-day Northern Hemisphere ice sheets are prescribed as a constant area with ice albedo throughout the year independent of the snow line position. All of Antarctica is covered by ice in the model.

2.2 Atmospheric chemistry and air–sea gas exchange

For each atmospheric box we consider partial pressures of $^{12,13}\text{CO}_2$, $^{12,13}\text{CH}_4$, N_2O and O_2 . The prognostic equation for the partial pressure of a gas χ is taken to be

$$\frac{dp(\chi)}{dt} = \frac{1}{v_a} \left[A_o^{\text{if}} \Psi_S(\chi) + \Psi_I(\chi) \pm \Psi_T(\chi) \right], \quad (12)$$

where v_a is an atmospheric mole volume; A_o^{if} is an ice-free ocean surface area; Ψ_S is an air–sea gas exchange flux; Ψ_I denotes sources or sinks within the atmosphere or net transports to or from the atmosphere via weathering, volcanism, interaction with land biosphere and – for recent times – anthropogenic activities; and Ψ_T is the gas transport between adjacent atmospheric boxes.

Air–sea exchange for $^{12}\text{CO}_2$ for each atmospheric box is written as (for simplicity we omit the atmospheric box index superscript)

$$\Psi_S = k_w \eta_{\text{CO}_2} (p\text{CO}_2 - p\text{CO}_{2,w}), \quad (13)$$

where the gas transfer velocity k_w is $0.39 u^2 (Sc/660)^{-0.5}$ with u being the long-term annual mean wind speed at 10 m above the ocean surface, Sc the CO_2 Schmidt number that depends on prognostic temperatures of the ocean surface layers (Wanninkhof, 1992), and η_{CO_2} the CO_2 solubility that is a function of temperature and salinity of the surface ocean layer (Weiss, 1974). $p\text{CO}_{2,w}$ is the prognostic CO_2 partial pressure at the ocean surface layer equal to $[\text{CO}_2]/\eta_{\text{CO}_2}$, where $[\text{CO}_2]$ is the prognostic dissolved CO_2 concentration of the ocean surface layer calculated from ocean carbonate carbon chemistry (see Sect. 2.4). Wind speeds are not calculated in our simplified atmosphere module, so we use observed values from the NOAA/CIRES/DOE 20th Century Reanalysis (V3) dataset for each ocean sector. For extremely warm climate experiments (annual mean sea-surface temperatures over $30 \text{ }^\circ\text{C}$), we use the Schmidt number formulation from Gröger and Mikolajewicz (2011), who demonstrated that the Wanninkhof (1992) formulation underestimates Sc in such conditions.

Air–sea exchange for $^i\text{CO}_2$ ($i = 13$ and 14) is given by

$$\Psi_S^i = k_w \eta_{\text{CO}_2}^i \alpha_k \left({}^i\alpha_{aw} p^i \text{CO}_2 - {}^i\alpha_{wa} p \text{CO}_{2,w} \frac{[\text{DIC}^i]}{[\text{DIC}]} \right), \quad (14)$$

where ${}^i\alpha_k = 0.99912$ is the kinetic fractionation factor (Zhang et al., 1995), $[\text{DIC}^i]$ and $[\text{DIC}]$ are concentrations of dissolved inorganic carbon in the surface ocean layer, ${}^i\alpha_{aw}$ is the fractionation factor due to different solubilities in the equilibration process, and ${}^i\alpha_{wa}$ is the fractionation factor in the dissociation reactions associated with ocean carbonate chemistry. This latter term is expressed as

$${}^i\alpha_{wa} = \frac{[\text{CO}_2] + {}^i\alpha_{\text{HCO}_3} [\text{HCO}_3^-] + {}^i\alpha_{\text{CO}_3} [\text{CO}_3^{2-}]}{[\text{DIC}]}, \quad (15)$$

where ${}^i\alpha_{\text{HCO}_3}$ and ${}^i\alpha_{\text{CO}_3}$ are individual fractionation factors for the carbon species $[\text{HCO}_3^-]$ and $[\text{CO}_3^{2-}]$ and surface layer values for these species are obtained from ocean carbonate chemistry calculations. Moreover, ${}^i\alpha_{\text{HCO}_3}$ and ${}^i\alpha_{\text{CO}_3}$ are functions of surface layer temperature (Zhang et al., 1995). As the rate at which different isotopes of a chemical element take part in a chemical reaction depends on their mass, we assume the $^{14}\text{C}/^{12}\text{C}$ fractionation to be twice as strong as that of $^{13}\text{C}/^{12}\text{C}$, and then ${}^{14}\alpha = 1 - 2(1 - {}^{13}\alpha)$.

For air–sea exchange of oxygen for each ocean surface sector,

$$\Psi_S = k_w (\eta_{\text{O}_2} p \text{O}_2 - [\text{O}_2]), \quad (16)$$

with k_w as before but with O_2 Schmidt numbers that depend on prognostic temperatures of the ocean surface layers (Keeling et al., 1998). The O_2 solubility (η_{O_2}) was converted from Bunsen solubility coefficients that depend on prognostic temperatures and salinities (Weiss, 1970) to model units using the ideal gas mole volume; $[\text{O}_2]$ is the prognostic dissolved oxygen concentration in the ocean surface layer (see Sect. 2.4). At present we do not include the air–sea exchange of methane and nitrous oxide in this model version. However, this could be readily accomplished as needed, as this has been successfully implemented in the DCESS I model (Shaffer et al., 2017).

With regard to sources and sinks (the second term on the right-hand side of Eq. 12), the model considers the following sources and sinks for each atmospheric tracer.

For carbon dioxide, there is net exchange with the land biosphere, oxidation of atmospheric methane, volcanic input, weathering of “old” organic carbon in rocks, and weathering of carbonate and silicate rocks. As needed, anthropogenic CO_2 sources associated with fossil fuel burning and/or land use change may be added. All these sources and sinks are also considered for atmospheric $^{13}\text{CO}_2$. For $^{14}\text{CO}_2$ the same sources and sinks as above are included, except for old (and thus ^{14}C -free) carbon sources, which are inputs from volcanoes, organic carbon weathering and fossil fuel burning. In addition, ^{14}C is produced naturally in the atmosphere via

cosmic ray flux and, in recent times, by atomic bomb testing. For each atmospheric box, the cosmic ray source of $^{14}\text{CO}_2$ can be expressed as $A^{l,m,h} p_{14\text{C}}^{l,m,h} / A_{\text{vg}}$, where A_{vg} is the Avogadro number and $P_{14\text{C}}^{l,m,h}$ (in atoms $\text{m}^{-2} \text{s}^{-1}$) is the magnitude of ^{14}C production, chosen here to match the estimated pre-industrial atmospheric ^{14}C concentration such that $\Delta^{14}\text{C}_{\text{atm}} \sim 0\%$. A small amount of atmospheric ^{14}C enters the land biosphere and decays there radioactively. A smaller fraction decays directly in the atmosphere, becoming an atmospheric sink of $^{14}\text{CO}_2$ with a decay rate $\lambda_{14\text{C}}$ of $3.84 \times 10^{-12} \text{s}^{-1}$. By far most of the ^{14}C produced enters the ocean by air–sea exchange, and by far most of this isotope decays within the ocean. Finally, a small amount of ^{14}C enters the ocean sediment via sinking of biogenic particles and part of this returns to the ocean due to remineralization/dissolution in the ocean sediment.

For methane there is production within the land biosphere (see Sect. 2.6) and consumption associated with OH radicals in the troposphere. The latter leads to the net consumption of two O_2 molecules and production of one CO_2 molecule for every CH_4 molecule consumed. Since this reaction depletes the concentration of these radicals, the atmospheric lifetime of CH_4 grows as methane concentration rises. We include this effect in the model by taking the atmospheric methane sink to be $\lambda_{\text{CH}_4} p \text{CH}_4$, with $\lambda_{\text{CH}_4} = v_a / \tau_{\text{CH}_4}$, where τ_{CH_4} is the (variable) atmospheric lifetime of methane. This lifetime is determined by fitting a function to the results from several modeling studies that consider a wide range of $p \text{CH}_4$ values. This fit yields a pre-industrial lifetime of 9.5 years, increasing for example to 10.8 and 15.1 years for 2 and 10 times the pre-industrial methane level, respectively (see Shaffer et al., 2017, for details). Potential sources like melting of methane hydrate in the Arctic tundra and ocean sediments and by human activities may be included in the model as needed. For $^{13}\text{CH}_4$ the same processes are considered but with their respective fractionation factors (Sect. 2.6) and adding the $p^{13}\text{CH}_4 / p^{12}\text{CH}_4$ ratio to the above OH-related atmospheric methane sink formulation.

For nitrous oxide there is production within the land biosphere and consumption in the atmosphere, here mainly due to photodissociation in the stratosphere. This is modeled as $\lambda_{\text{N}_2\text{O}} p \text{N}_2\text{O}$, with $\lambda_{\text{N}_2\text{O}} = v_a / \tau_{\text{N}_2\text{O}}$, where $\tau_{\text{N}_2\text{O}}$, the atmospheric lifetime of N_2O , is taken to be 150 years. Potential sources like N_2O flux from ocean denitrification and by human activities may be included in the model as needed.

For oxygen, there is consumption associated with oxidation of atmospheric methane and reaction with OH radicals (see above) and sinks (sources) from organic matter remineralization (photosynthesis) on land. Since methane is the end product of some of the remineralization on land (see Sect. 2.6), the land biosphere is a net O_2 source in a steady state. Furthermore, there are long-term atmospheric oxygen sinks due to weathering of organic carbon in rocks and oxidation of reduced carbon emitted in lithosphere outgassing. A

long-term, quasi-steady state of pO_2 is achieved in the model when these latter sinks balance net O_2 outgassing from the ocean from less O_2 consumption than production there due to burial of organic matter in the model ocean sediments. However, for multi-million-year timescales, the global sulfur cycle would need to be included in the model to achieve “true” pO_2 steady states (Bernier, 2006). Additional sinks (sources) of atmospheric O_2 associated with recent land use change and with burning of fossil fuels may be included in the model as needed.

The last term in Eq. (12) representing the gas transport between two adjacent atmospheric boxes is modeled as

$$\Psi_T(\chi) = -k_\chi \frac{dp(\chi)}{d\phi}, \quad (17)$$

with $k_\chi = 6 \times 10^{-8} \text{ s}^{-1}$ based on data–model comparisons we made using the DCESS I model (Shaffer et al., 2008). For simplicity, we take the same value for all gases and for all atmospheric boundaries.

Evaporation and precipitation modify both salinity and oxygen isotopic composition in the surface ocean. Fractionation due to evaporation enriches (depletes) the ^{18}O content in seawater (water vapor) from net evaporative model ocean (atmospheric) zones. Further depletion in water vapor takes place due to fractionation in the condensation process as the air mass cools in its poleward path. Given the importance of ^{18}O in paleoclimate studies, we incorporate atmospheric cycling of oxygen isotopes of water following Olsen et al. (2005), which gives the ^{18}O content in the well-known delta notation ($\delta^{18}O_w$) relative to Vienna Standard Mean Ocean Water (VSMOW). This approach takes advantage of meridional atmospheric temperature profiles estimating $\delta^{18}O_a$ at every atmospheric box division, where the subscript “a” refers to isotopic excursion of ^{18}O in the atmosphere.

2.3 Ocean circulation and mixing

Simplified ocean dynamics in the model consist of a balance between the pressure gradient force and linear (Rayleigh) friction acting on the meridional velocity. Model flow is defined by this relation and hydrostatic and continuity equations:

$$-\frac{1}{r\rho_0} \frac{\partial P}{\partial \phi} - rfv = 0, \quad (18)$$

$$-\frac{1}{\rho_0} \frac{\partial P}{\partial z} - \frac{\rho}{\rho_0} g = 0, \quad (19)$$

$$\frac{1}{r \cos \phi} \frac{\partial v \cos \phi}{\partial \phi} + \frac{\partial w}{\partial z} = 0, \quad (20)$$

where r_f is a friction coefficient (Table 2); v and w are the meridional and vertical velocity components, respectively; P is the pressure; g is gravity; and ρ is the water density, calculated using the non-linear function of temperature, salinity

and pressure according to the TEOS-10 standard (the international Thermodynamic Equation of Seawater; IOC et al., 2010) but modified for Boussinesq ocean models (Roquet et al., 2015).

Since there are no meridional boundaries at the Drake Passage, a geostrophic flow cannot be maintained above the sill depth there. To account for this feature in our simplified model, a virtual barrier against meridional flow is placed at 55° S from the surface to 2000 m depth (Fig. 2). Equatorward Ekman transport there, forced by prevailing westerly winds, is included by prescribing a net northward volume flux (E_k) in the surface layer, taken to be a total of 30 Sv injected into the South Atlantic and South Pacific sectors (msA and msP) and distributed according to the widths of these sectors. This transport, which carries Southern Ocean surface water properties, is injected into the corresponding density levels of these sectors, forming the model’s Antarctic Intermediate Waters (AAIW). Moreover, a northward surface flow of 1 Sv at 65° N is prescribed to consider the net ocean exchange between the North Pacific and the Arctic Ocean across the Bering Strait. This flow carrying surface North Pacific properties enters at the corresponding density level in the Arctic Ocean. At all other latitudes, meridional flow is set to zero in the surface layer, where exchanges rely entirely on horizontal and vertical mixing processes (Shaffer and Olsen, 2001). The zonally averaged velocity at each meridional zone boundary is related to the density field according to

$$v(z > d_w) = -\frac{g}{ar_f \rho_0} \int_0^z \frac{\partial \rho}{\partial \phi} dz - \frac{g}{ar_f} \frac{\partial \eta}{\partial \phi}, \quad (21)$$

where η is the sea level and d_w is the depth of the mixed layer or, for the Southern Ocean, the Drake Passage sill depth and, for the Arctic Ocean, the Denmark Strait sill depth. Sea levels of the model ocean zones are adjusted instantaneously to conserve mass and to form sea level gradients in Eq. (21) that lead to ocean meridional transports needed to balance the Ekman transport and atmospheric freshwater forcing at the ocean surface. Finally, the vertical flow is calculated from a continuity equation, given meridional flow, Ekman transport, atmospheric freshwater forcing and shelf exchange (see below).

The effect of wind-driven gyre mixing is parameterized by a depth-dependent, horizontal diffusivity:

$$K_h(z) = K_h^d + K_h^s \exp\left(-\frac{z}{z_g}\right), \quad (22)$$

where K_h^d and K_h^s denote the deep and surface horizontal diffusivities and z_g is an e -folding gyre depth (Table 2). At the Southern Ocean, where wind-driven gyre mixing is not important, K_h^s is decreased by 90 %. The same approach is taken at the North Pacific sector, where North Pacific Intermediate Water (NPIW) is formed with a reduction of 50 % in K_h^s .

Table 2. Ocean module physical and biogeochemical parameters as well as applied Redfield ratios.

Parameter	Symbol	Value
Ocean physics		
Meridional flow friction coefficient	r_f	$1 \times 10^{-4} \text{ s}^{-1}$
Deep-ocean horizontal diffusivity	K_b^d	$1 \times 10^3 \text{ m}^2 \text{ s}^{-1}$
Surface ocean horizontal diffusivity	K_b^s	$2.5 \times 10^4 \text{ m}^2 \text{ s}^{-1}$
e -folding depth for horizontal diffusivity scale	z_g	200 m
Total freshwater flux to the Southern Ocean shelf from melting, calving and precipitation	F_g	0.07 Sv
Sea ice export flux from Southern Ocean shelf	F_i	0.13 Sv
Ocean biochemistry		
Limitation factor (Southern Ocean/Arctic Ocean)	L_f	0.15/0.30 s^{-1}
Upper limit for rain ratio	$r_{\text{Cal,max}}$	0.35
Steepness factor for calcite production	μ	0.16
Nutrient remineralization length scale	ξ_N	833 m
Carbon remineralization length scale	ξ_C	769 m
Calcite dissolution length scale	ξ_{Cal}	2500 m
Redfield ratios		
Carbon to phosphate	r_{CP}	106
Alkalinity to phosphate	r_{AlkP}	16
Oxygen to phosphate (nutrient component)	r_{ONP}	32
Oxygen to phosphate (carbon component)	r_{OCP}	118

With this setting, the model can reproduce global-scale intermediate water masses (AAIW and NPIW) in a simple way as reported by other model studies (England, 1993; Stocker et al., 1994). This is one of the few “regional tunings” in the model. The vertical diffusivity, K_v , is modeled using a stratification-dependent form, such that

$$K_v(z) = \min \left[K_v^{\text{max}}, K_v^0 \left(\frac{N}{N_0} \right)^{-\gamma} \right] \text{ for } N > 0, \quad (23)$$

where N is the Brunt–Väisälä frequency equal to $[(g/\rho_0)(\partial\rho/\partial z)]^{1/2}$. According to Gargett and Holloway (1984), we set γ to 0.5, indicating a relatively weak dependence on stratification associated with diapycnal mixing via breaking of internal waves. Furthermore, K_v^0 and N_0 are the respective scale values of K_v and N , taken as globally representative thermocline values equal to $3 \times 10^{-5} \text{ m}^2 \text{ s}^{-1}$ and 10^{-2} s^{-1} , respectively (Kunze, 2017). For unstable stratification, K_v is equated with K_v^{max} ($8 \times 10^{-4} \text{ m}^2 \text{ s}^{-1}$), accounting for model convective adjustment.

2.3.1 Southern Ocean shelf and Antarctic Bottom Water formation

Antarctic Bottom Water (AABW) constitutes a major ocean water mass filling and ventilating the abyssal ocean on a global scale (Johnson, 2008; Orsi et al., 1999). Additionally, AABW plays a crucial role through the global overturning circulation in the transport and redistribution of heat, salt,

nutrients and carbon (among other tracers) and thus affects atmospheric CO_2 concentrations and thereby global climate (Orsi, 2010; Purkey and Johnson, 2013).

AABW originates from dense shelf water, formed by air cooling and brine rejection during sea ice formation, that can flow down the slope, reaching abyssal ocean depths (Gordon, 2019). To address this process, we include a 500 m deep Southern Ocean shelf (Heywood et al., 2014) between 69 and 70° S. Furthermore, we assume that there are enough air–sea heat exchanges on the shelf to maintain temperature there at freezing temperature T_f . Then the prognostic equation for all shelf tracers but temperature (ψ_{sh}) is

$$\frac{\partial \psi_{\text{sh}}}{\partial t} = \frac{1}{V_{\text{sh}}} \left[(F_g - F_c) \psi_g - F_i \psi_i + F_i \psi_{\text{SO}} - F_{\text{sl},0} \psi_{\text{sh}} + F_{\text{ge}} A_{\text{sh}}^{\text{if}} \right], \quad (24)$$

where V_{sh} is the shelf volume; F_g is the total freshwater flux to the Southern Ocean shelf from melting, calving and precipitation and F_c is the iceberg export from the shelf taken as 0.07 and 0.02 Sv, respectively. Furthermore, F_i is the sea ice export to the Southern Ocean, taken as 0.13 Sv (Haumann et al., 2016); F_r is the replacement flux from the Southern Ocean to the shelf; and $F_{\text{sl},0}$ is the volume flux leaving the shelf at the shelf break (see below). Each of these fluxes carry their own tracer values (ψ_g , ψ_i , ψ_{SO} and ψ_{sh}). Values of ψ_g are zero for salinity, phosphate and alkalinity tracers; $\eta_{\text{CO}_2} P^{12,13,14} \text{CO}_2$ for $\text{DI}^{12,13,14}\text{C}$; $\eta_{\text{O}_2} \text{O}_2$ for dissolved oxygen; and a constant value of -40‰ for $\delta^{18}\text{O}_w$. The latter is a

rough estimate for the mean present-day $\delta^{18}\text{O}_w$ value of ice exported from Antarctica based on snow input values and ice sheet flow (Masson-Delmotte et al., 2008). For Ψ_1 , sea ice takes the shelf water value, except for salinity, which is taken as a constant equal to 5 g kg^{-1} . Furthermore, a fraction of the freshwater flux crossing 55°S falls directly into the Southern Ocean and the rest goes to Antarctica. In a steady state, the amount going to Antarctica is equal to F_g . The last right-hand term corresponds to the air–sea gas exchange, where F_{ge} is the gas flux and A_{sh}^{if} is the ice-free surface shelf area, meant mainly to represent coastal polynyas. Here we take A_{sh}^{if} to be 20% of the total shelf area.

If it is denser than ambient Southern Ocean water, shelf water flows down along the continental slope. On a path to the deep ocean, downslope flow takes up ambient water via entrainment, typically increasing its volume to more than twice its value at the shelf break to finally fill the abyssal ocean as AABW (Orsi et al., 2002; Orsi et al., 2001). In order to include a comparable AABW formation process in our model, we address this using a simple formulation of entrainment following approaches described in Baines (2005, 2008). The governing equations for the downslope flux (F_d) and the plume height (or thickness, H) normal to the slope are

$$\frac{dF_{sd}}{ds} = E \frac{F_{sd}}{H}, \quad (25)$$

$$\frac{dH}{ds} = 2E + C_d - S_2 Ri \tan \theta, \quad (26)$$

where s is the downslope distance from the shelf break depth obtained from observed bathymetry (Amante and Eakins, 2009) and E is the entrainment coefficient equal to $E_0(1 - Ri/Ri_c)$ for $\leq Ri \leq Ri_c$ and zero otherwise. Here Ri is the Richardson number, Ri_c is a critical value for Ri , and E_0 is an amplitude parameter. Ri is defined as $G H^3 \cos \theta / F_{sd}^2$, where $G = g \Delta \rho(z) / \rho_0$ is the buoyancy, $\Delta \rho(z)$ is the difference between downflow density and the mean local ambient density, and θ is the slope angle. Values for Ri_c and E_0 are taken to be 0.25 and 0.20, respectively (Xu et al., 2006). Finally, C_d and S_2 are the drag coefficient and a constant, respectively, with values taken from the literature cited above. Initial conditions at the shelf break are taken to be $H_0 = 100 \text{ m}$ and $F_{sd,0} = H_0(G_0 H_0)^{0.5}$, with G_0 calculated as above using the Southern Ocean density at the shelf break depth. We integrate Eqs. (25) and (26) every 2 m from the shelf break until the depth where the plume and the ambient water buoyancy are close enough as defined by a threshold. Then this downslope flow enters Southern Ocean model layers in accordance with the plume height. Although other overflow approaches have been proposed (Danabasoglu et al., 2010; Xu et al., 2006), we think that this simple and fast approach is well suited to capturing the formation and insertion of AABW at depth and is a particular strength in our simplified model. In this context we note that quite a few CMIP6

models form AABW incorrectly by deep, open-ocean convection and/or by lack of plume entrainment (Heuzé, 2021).

With the above physics and for any ocean zone, the general conservation equation of any ocean tracer ψ may be written as

$$\begin{aligned} \frac{\partial \psi}{\partial t} + \frac{1}{a \cos \phi} \frac{\partial (\cos \phi v \psi)}{\partial \phi} + \frac{\partial (w \psi)}{\partial z} &= \frac{1}{a^2 \cos \phi} \\ &\frac{\partial}{\partial \phi} \left(\cos \phi K_h \frac{\partial \psi}{\partial \phi} \right) + \frac{\partial}{\partial z} \left(K_v \frac{\partial \psi}{\partial z} \right) + \Psi_S(\psi) \\ &+ \Psi_B(\psi) + \Psi_I(\psi), \end{aligned} \quad (27)$$

where Ψ_S is the air–sea exchange of heat and gases, Ψ_B is the exchange of dissolved substances with the ocean sediment, and Ψ_I are internal sources and sinks into the water column. Ocean tracers of temperature, salinity and $\delta^{18}\text{O}_w$ are forced only at the ocean surface via air–sea heat exchange and direct solar forcing for temperature and freshwater forcing for salinity and $\delta^{18}\text{O}_w$. Pacific Ocean and Atlantic Ocean model sectors between 35 and 55°S south of Africa are connected via a zonal surface-intensified mixing scheme in order to emulate the role of the Antarctic Circumpolar Current there. These specific terms are added to Eq. (27) for tracers of these sectors (msA and msP).

2.4 Ocean biogeochemical cycling

The ocean module considers the following biogeochemical ocean tracers: phosphate (PO_4), dissolved oxygen (O_2), dissolved inorganic carbon (DIC) in $^{12,13,14}\text{C}$ species and alkalinity (ALK), which are all forced by new (export) production of organic matter and biogenic calcium carbonate shells in the lighted ocean surface layers. Furthermore, PO_4 , $\text{DI}^{12,13,14}\text{C}$ and ALK are forced by river inputs and concentration/dilution of the surface layer by evaporation/precipitation. Moreover, O_2 and $\text{DI}^{12,13,14}\text{C}$ are forced by air–sea exchange. In the ocean interior, all these tracers are influenced by remineralization of organic matter and dissolution of CaCO_3 shells in the water column as well as exchange with the ocean sediment. DI^{14}C is affected by radioactive decay in all ocean layers. For simplicity, we have neglected explicit nitrogen cycling and have assumed that all biogenic matter export from the surface layer is in the form of particulate organic matter (POM) and that all CaCO_3 is in the form of calcite.

We take new (export) production of organic matter (NP) in each model surface layer to be a function of phosphorus (Maier-Reimer, 1993; Yamanaka and Tajika, 1996) and solar radiation as

$$\text{NP} = A_o^{\text{if}} z_{\text{eu}} L_f [\text{PO}_4] \frac{I}{I + I_{1/2}} \frac{[\text{PO}_4]}{[\text{PO}_4] + P_{1/2}}, \quad (28)$$

where A_o^{if} is the ice-free ocean surface area; z_{eu} is the euphotic layer depth (100 m); and $[\text{PO}_4]$ and I are phosphate content and solar radiation in the surface ocean, respectively.

$P_{1/2}$ and $I_{1/2}$ are their respective half-saturation constants equal to $1 \mu\text{mol m}^{-3}$ for phosphate and 100 W m^{-2} for light (Mutshinda et al., 2017). L_f is an efficiency coefficient (units of s^{-1}) that estimates iron and/or other limitation factors on net primary production. We take the value of L_f to be equal to 1 for most ocean zones but set to some lower value for the Southern and Arctic oceans as determined by the model fit to ocean data (Sect. 3.1.2). In the surface layer, sources and sinks due to new production for PO_4 , DI^{12}C , ALK and O_2 are $-NP$, $-r_{\text{CP}}NP$, $r_{\text{Alk}}NP$ and $(r_{\text{OCP}} + r_{\text{ONP}})NP$, respectively, where r_{CP} , r_{Alk} , r_{OCP} and r_{ONP} are the Redfield ratios of C : P, ALK : P, $(\text{O}_2)_\text{C}$: P and $(\text{O}_2)_\text{N}$: P, respectively. The subscripts C and N refer to a division of POM into “carbon” and “nutrient” parts, respectively, as explained below. We adopted the Redfield ratios used in Shaffer et al. (2008) and shown in Table 2. For $\text{DI}^{13,14}\text{C}$, the surface sink due to new production and associated isotope fractionation is $-^{13,14}\alpha_{\text{Org}}([\text{DI}^{13,14}\text{C}]/[\text{DI}^{12}\text{C}])_{\text{eu}} r_{\text{CP}}NP$. We take the fractionation factor $^{13}\alpha_{\text{Org}}$ to depend on surface ocean concentrations of dissolved carbon dioxide ($[\text{CO}_2(\text{aq})]$) and phosphate according to Pagani et al. (1999):

$$^{13}\alpha_{\text{Org}} = 25 - \frac{116.96L_f[\text{PO}_4] + 81.42}{[\text{CO}_2(\text{aq})]}, \quad (29)$$

where concentrations are in $\mu\text{mol kg}^{-1}$. As previously, $^{14}\alpha_{\text{Org}} = 1 - 2(1 - ^{13}\alpha_{\text{Org}})$.

The surface (export) production of biogenic calcite is related to new (export) production by $r_{\text{CaC}}r_{\text{CP}}NP$, where r_{CaC} is the “rain” ratio, the ratio between the production of CaCO_3 and the production of organic carbon. It is parameterized according to Maier-Reimer (1993) and Marchal et al. (1998) but with the addition of a dependence on the calcite saturation state of the ocean surface layer (Ω_S) following Shaffer et al. (2016):

$$r_{\text{CaC}} = r_{\text{CaC,max}} \frac{\exp(\mu(T_s - T_{\text{ref}}))}{1 + \exp(\mu(T_s - T_{\text{ref}}))} \frac{\Omega_S - 1}{v + (\Omega_S - 1)}, \quad (30)$$

where $r_{\text{CaC,max}}$ is a rain ratio upper limit; μ is the steepness factor; T_s and T_{ref} are the surface temperature and the reference temperature (10°C), respectively; and v is a half-saturation constant taken to be 1 (Gangstø et al., 2011). Furthermore, $\Omega_S = [\text{Ca}^{2+}][\text{CO}_3^{2-}]/K_{\text{sp}}$, with calcium concentration given as $[\text{Ca}^{2+}] = [\text{Ca}^{2+}]_m (S/S_m)$, where $[\text{Ca}^{2+}]_m$ and S_m are the global ocean mean calcium and salinity values, taken as 10.57 mol m^{-3} and 35 for the present day, respectively; S is the ocean salinity; and K_{sp} is the calcite solubility coefficient. There is no biogenic calcite production for subsaturated conditions ($r_{\text{CaC}} = 0$ for $\Omega_S \leq 1$). Values for $r_{\text{CaC,max}}$ and μ are determined by the model fit to ocean and ocean sediment data. With this, surface sinks for DI^{12}C and ALK due to biogenic calcite production are $-r_{\text{CaC}}r_{\text{CP}}NP$ and $-2r_{\text{CaC}}r_{\text{CP}}NP$, respectively. For $\text{DI}^{13,14}\text{C}$, the surface sinks due to calcite production and associated isotope fractionation are $-^{13,14}\alpha_{\text{CaC}}([\text{DI}^{13,14}\text{C}]/[\text{DI}^{12}\text{C}])_{\text{eu}} r_{\text{CaC}}r_{\text{CP}}NP$,

where $\alpha_{\text{CaC}} = 1$, assuming no carbon fractionation during biogenic calcite formation in the ocean surface layer.

Particles are assumed to sink out of the surface layer with settling speeds high enough to neglect advection and diffusion of them. This particulate flux decreases significantly with depth due to subsurface remineralization/dissolution, with only a small fraction reaching the seafloor, as shown by sediment trap data (Martin et al., 1987). To address this, we assume an exponential-type law for the vertical fraction of the particulate organic matter (POM) nutrient and carbon components, each with a distinct e -folding length (ξ_N and ξ_C) motivated mainly by results of Shaffer et al. (1999). Additionally, we also include temperature dependence (λ_Q) on remineralization rates as indicated by ocean data (Laufkotter et al., 2017; Marsay et al., 2015). Therefore, tracer sources in the water column due to the remineralization of POM, the nutrient (Φ_N) and carbon component (Φ_C), are expressed as the vertical gradient of POM:

$$\Phi_{N,C}(z) = \frac{\partial \text{POM}(z)_{N,C}}{\partial z} = \text{POM}(z)_{N,C} \frac{\lambda_Q(T_o(z))}{\xi_{N,C}}, \quad (31)$$

where λ_Q is defined as $Q_{10}^{(T_o(z) - T_{o,\text{ref}})/10}$, with Q_{10} being the biotic activity increase for a 10°C increase in T_o , $T_{o,\text{ref}}$ a reference temperature taken as the present-day global area-weighted mean observed temperature from the World Ocean Atlas 2018 database (Boyer et al., 2018) for the upper 500 m (Komar and Zeebe, 2021) and $\xi_{N,C}$ e -folding lengths for $T_o(z) = T_{o,\text{ref}} = 9.3^\circ\text{C}$. For the biogenic calcium carbonate particle flux (PCal), we take a simple exponential law with a constant e -folding length ξ_{CaC} , and, as above, tracer sources in the water column due to dissolution of CaCO_3 produced in the euphotic zone (Φ_{CaC}) are expressed as

$$\Phi_{\text{CaC}}(z) = \frac{\partial \text{PCal}(z)}{\partial z} = \frac{\text{PCal}(z)}{\xi_{\text{CaC}}}. \quad (32)$$

In Eqs. (31) and (32), POM_N , POM_C and PCal at $z = 0$ are the respective surface layer export productions, NP , $r_{\text{CP}}NP$ and $r_{\text{CaC}}r_{\text{CP}}NP$. Given the range of Q_{10} values shown by data and modeling studies (Laufkotter et al., 2017; Regaudie-de-Gioux and Duarte, 2012; Bendtsen et al., 2015) and to maintain model simplicity (see Sect. 2.6 and 2.7), we choose a constant value for Q_{10} of 2. Also for simplicity, ξ_N , ξ_C and ξ_{CaC} are taken to be constants for all ocean zones, whose values (Table 2) have been chosen to fit ocean data (Sect. 3.1.2). Thus, the vertical source and sinks in the ocean interior for PO_4 , DI^{12}C , ALK and O_2 are Φ_N , $(\Phi_C + \Phi_{\text{CaC}})$, $(2\Phi_{\text{CaC}} - r_{\text{Alk}}\Phi_N)$ and $(r_{\text{ONP}}\Phi_N + r_{\text{OCP}}\Phi_C)$, respectively. For $\text{DI}^{13,14}\text{C}$, the vertical distribution from remineralization and dissolution is $([\text{DI}^{13,14}\text{C}]/[\text{DI}^{12}\text{C}])_{\text{eu}} [^{13,14}\alpha_{\text{Org}}\Phi_C + ^{13,14}\alpha_{\text{CaC}}\Phi_{\text{CaC}}]$. All these vertical distributions are weighted by the ocean area profile $A_o(z)$ for each zone. In addition, the fluxes of P and $^{12,13,14}\text{C}$ that fall in the form of POM and/or biogenic calcite particles on the model ocean sediment surface at any depth of

each zone are calculated as the product of $dA_o(z)/dz$ there and the difference between the particulate fluxes falling out of the ocean surface layer and the remineralization/dissolution taking place down to the depth of each zone.

Non-linear ocean carbonate chemistry is calculated using the recursive formulation of Antoine and Morel (1995) as explained in detail in Shaffer et al. (2008) in the context of a DCESS-model approach. This system yields ocean distributions of $\text{CO}_2(\text{aq})$, CO_3^{2-} , HCO_3^- and hydrogen ion concentrations needed for calculations of air–sea exchange of carbon dioxide, carbon isotopic fractionation during air–sea exchange and ocean new production, dissolution of calcite in the ocean sediment, and pH (seawater scale). Profiles of carbonate saturation with respect to calcite are calculated as $K'_{\text{CaCO}_3}/([\text{Ca}^{2+}]_m S/S_m)$, where K'_{CaCO_3} is the apparent dissociation constant for calcite as function of T , S and pressure (Mucci, 1983).

2.5 Ocean sediment

For the sediment module, we adopt the approach developed by Shaffer et al. (2008), the main features of which are summarized below.

Each model ocean layer of 100 m thickness is assigned a sediment segment composed of calcite, non-calcite mineral (NCM) and reactive organic matter. The segment is a bioturbated layer (BL) that is assumed to be 10 cm thick divided into seven sublayers with the highest resolution near the sediment surface such that sublayer boundaries are 0, 0.2, 0.5, 1, 1.8, 3.2, 6 and 10 cm. Sediment segment areas are determined by model topography from each ocean zone. POM and PCal rain fluxes and ocean values of T , S , DIC, ALK, O_2 and PO_4 are taken from respective layers from ocean and ocean biogeochemistry modules. NCM fluxes (F_{NCM}) are parameterized as

$$F_{\text{NCM}} = \text{NCF} \left[1 + \text{CAF} \exp(-z/\lambda_{\text{slope}}) \right], \quad (33)$$

where NCF is the open-ocean non-calcite flux, CAF is an amplification factor at the coast (i.e., at $z = 0$) and λ_{slope} is the e -folding water depth scale representing the effect of distance from the coast associated with continental slope topography. For simplicity, we apply the same values of NCF, CAF and λ_{slope} , taken to be $0.3 \text{ g cm}^{-2} \text{ kyr}^{-1}$, 20 and 200 m, respectively, to all ocean sectors.

The sediment module is designed to address calcium carbonate (CaCO_3) dissolution and (oxic and anoxic) organic matter remineralization by calculating concentrations of reactive organic carbon (OrgC), pore-water O_2 and pore-water CO_3^{2-} for each sediment sublayer. To accomplish this, a key property is the sediment porosity (ϕ_s , not to be confused with the latitude symbol), which is parameterized as a function of the calcite dry-weight fraction, $(\text{CaCO}_3)_{\text{dwt}}$:

$$\phi_s(\zeta) = \phi_{s,\text{min}} + (1 - \phi_{s,\text{min}}) \exp(-\zeta/\alpha), \quad (34)$$

where ζ is the sediment vertical coordinate, $\phi_{s,\text{min}} = 1 - (0.483 + 0.45(\text{CaCO}_3)_{\text{dwt}})$ and $\alpha = 0.25(\text{CaCO}_3)_{\text{dwt}} + 3(1 - (\text{CaCO}_3)_{\text{dwt}})$ following Archer (1996). From sediment porosity, the sediment formation factor ($F_s = \phi_s^{-3}$) is determined in order to calculate bulk sediment diffusion coefficients of pore-water solutes.

To account for the role of benthic fauna, the bioturbation rate (D_b) is parameterized not only to depend on organic carbon rain rates but also to consider attenuation associated with very low dissolved oxygen concentrations. This is formulated as

$$D_b = D_b^0 \left(\frac{F_{\text{OrgC}}}{F_{\text{OrgC}}^0} \right)^{0.85} \frac{[\text{O}_{2,\text{ocean}}]}{[\text{O}_{2,\text{ocean}}] + \text{O}_{2,\text{low}}}, \quad (35)$$

where $[\text{O}_{2,\text{ocean}}]$ is the ocean O_2 concentration at the sediment surface and $\text{O}_{2,\text{low}}$ is taken to be 20 mmol m^{-3} . Moreover, D_b^0 and F_{OrgC}^0 are the bioturbation rate scale and the organic carbon rain rate scale, whose values are $1.38 \times 10^{-8} \text{ cm}^2 \text{ s}^{-1}$ and $1 \times 10^{-12} \text{ mol cm}^{-2} \text{ s}^{-1}$, based in part on Archer et al. (2002).

Oxygen remineralization rates in the BL are taken to scale as bioturbation rates (and thereby as organic carbon rain rates; Archer et al., 2002), such as $\lambda_{\text{ox}} = \lambda_{\text{ox}}^0 D_b/D_b^0$. Anoxic remineralization rates in the BL are slower than oxic rates and will depend upon the specific remineralization reactions involved (e.g., denitrification is faster than sulfate reduction). More organic rain would be associated with a more anoxic BL and a shift toward sulfate reduction. Therefore, we take $\lambda_{\text{anox}} = \beta \lambda_{\text{ox}}$, where β is taken to decrease for an increasing organic carbon rain rate such that $\beta = \beta_0 (F_{\text{OrgC}}/F_{\text{OrgC}}^0)^\gamma$. As described in Shaffer et al. (2008), values for λ_{ox}^0 , β_0 and γ were constrained by organic carbon burial observations to be $1 \times 10^{-9} \text{ s}^{-1}$, 0.1 and -0.3 , respectively.

Governing equations for OrgC, pore-water O_2 , and CO_3^{2-} and CaCO_3 are second-order, non-linear coupled differential equations which are solved for each sediment segment using a semi-analytical iterative approach (steady state) or time-stepping approach (time dependent) by imposing boundary conditions at the top and bottom of the BL and matching conditions at the sublayer boundaries. For simplicity we also apply the same calculated sediment remineralization rates to organic phosphorus raining on the sediment surface. Using a mass balance approach, sedimentation velocity is determined and used to calculate burial rates of phosphorus, organic carbon and carbonate carbon down and out of the base of the BL. In this way the model produces synthetic sediment cores at every depth for each of the model ocean basins. Furthermore, model solutions provide fluxes between ocean and sediment layers of PO_4 , O_2 , DIC and ALK based on concentrations of these tracers in each respective adjacent ocean layer and sediment pore-water concentrations from organic matter remineralization and calcium carbonate dissolution. A detailed description of the sediment module is given in Appendix A of Shaffer et al. (2008).

2.6 Land biosphere

Eichinger et al. (2017) defined three different dynamically varying vegetation zones to extend and improve the original DCESS I one-zone land biosphere module. The vegetation zones – a grassland–desert zone bordered equatorward and poleward by tropical forest and extratropical forest zones, respectively – were formulated by emulating the behavior of a complex land biosphere model (Gerber et al., 2004). With this approach, latitudinal boundaries of the zones could be defined as functions of global mean temperature alone, encompassing implicit dependency on precipitation. In this way, the very different carbon distributions between, say, aboveground biomass and soil for each zone and the responses of these carbon reservoirs to changing climate and atmospheric CO₂ could be addressed. For example, while most of the carbon in tropical forests is found above the ground, by far most of the carbon in extratropical forests is in the soil (Chapin et al., 2011). With this new three-zone module, the size and timing of carbon exchanges between atmosphere and land were represented much more realistically in cooling and warming experiments than with the original one-zone module (Eichinger et al., 2017). Furthermore, our three-zone approach allows for changing biosphere modulation of radiative forcing since albedo is higher for grasslands–deserts than for forests (see albedo formulations in Sect. 2.1).

Here we use the same approach but now expanded to two hemispheres. The vegetation zones are tropical forest (TF); grassland, savanna and desert (GSD); and extratropical forest (ET), which includes carbon reservoirs for leaves (M_G), wood (M_W), litter (M_D) and soil (M_S) (Shaffer et al., 2008). Latitudinal boundaries of each vegetation zone (ϕ_{TF-GSD} for the TF–GSD boundary and ϕ_{GSD-ET} for the GSD–ET boundary) are obtained using a fifth-order polynomial dependent on the deviation of hemispheric annual mean atmospheric temperature from the respective pre-industrial temperature such that $\phi(\delta T_a) = c_1 \delta T_a^5 + c_2 \delta T_a^4 + c_3 \delta T_a^3 + c_4 \delta T_a^2 + c_5 \delta T_a + c_6$, with $\delta T_a = T_a - T_{a,PI}$. Polynomial coefficients are obtained by fitting data from Gerber et al. (2004) for the Northern Hemisphere and Southern Hemisphere separately (Table 3). Poleward ET limits are the annual mean snow line for the Northern Hemisphere and the fixed position at 55°S for Southern Hemisphere (there is no land south of 55°S; see Fig. 1a). We note that the above approach is only strictly valid for $-10^\circ\text{C} < \delta T_a < 10^\circ\text{C}$, the range considered in the original experiments of Gerber et al. (2004). For warming, this corresponds to annual mean temperatures of less than about 25°C and corresponding atmospheric $p\text{CO}_2$ levels of less than about 1000–1500 ppm. For more extreme warming situations in the distant past or future, a re-evaluation of our land biosphere module would be necessary for use in model simulations.

Net primary production on land (NPP) takes up atmospheric CO₂ and is forced by seasonally varying solar ra-

diation. For each vegetation type zone, NPP is calculated according to

$$\text{NPP} = \text{NPP}_{PI} A_f f(I) \left[1 + f_{\text{CO}_2} \ln \left(\frac{p\text{CO}_2}{p\text{CO}_{2,PI}} \right) \right], \quad (36)$$

where NPP_{PI} is the pre-industrial net primary production (see Table 3); A_f is an area factor accounting for vegetation size change with respect to pre-industrial size; f_{CO_2} is the CO₂ fertilization factor equal to 0.37, a suitable value for the terrestrial biosphere (Eby et al., 2013; Zickfeld et al., 2013); $p\text{CO}_2$ is the model-calculated partial pressure of atmospheric carbon dioxide; and $f(I) = f_0 + a \exp(-((I-b)/c)^2)$ is a function fitted from model results (Hazarika et al., 2005) with coefficients a , b and c chosen to represent the seasonal cycle of solar radiation according to the specific orbital forcing parameters and f_0 chosen so that the annual mean value of $f(I)$ for each zone is equal to 1. Note that each vegetation type has its own function $f(I)$ with its respective parameters. With this formulation, NPP responds in a seasonal cycle according to $f(I)$ and to atmospheric carbon dioxide on longer timescales.

With the descriptions above and the assumptions that NPP is distributed between leaves and wood at the fixed ratio of 35 : 25, all leaf loss goes to litter, wood loss is divided between litter and soil at the fixed ratio of 20 : 5, and litter loss is divided between the atmosphere (as CO₂) and the soil at the fixed ratio of 45 : 10 (Siegenthaler and Oeschger, 1987; Shaffer et al., 2008), the conservation equations for the land biosphere reservoirs of ¹²C for leaves (M_G), wood (M_W), litter (M_D) and soil (M_S) for each of the six vegetation zones are

$$\frac{dM_G}{dt} = \frac{35}{60} \text{NPP} - \frac{35}{60} \text{NPP}_{PI} \frac{M_G}{M_{G,PI}}, \quad (37)$$

$$\frac{dM_W}{dt} = \frac{25}{60} \text{NPP} - \frac{25}{60} \text{NPP}_{PI} \frac{M_W}{M_{W,PI}}, \quad (38)$$

$$\begin{aligned} \frac{dM_D}{dt} = & \frac{35}{60} \text{NPP}_{PI} \frac{M_G}{M_{G,PI}} + \frac{20}{60} \text{NPP}_{PI} \frac{M_W}{M_{W,PI}} \\ & - \frac{55}{60} \text{NPP}_{PI} \frac{M_D}{M_{D,PI}} \lambda_Q, \end{aligned} \quad (39)$$

$$\begin{aligned} \frac{dM_S}{dt} = & \frac{5}{60} \text{NPP}_{PI} \frac{M_W}{M_{W,PI}} + \frac{10}{60} \text{NPP}_{PI} \frac{M_D}{M_{D,PI}} \lambda_Q \\ & - \frac{15}{60} \text{NPP}_{PI} \frac{M_S}{M_{S,PI}} \lambda_Q, \end{aligned} \quad (40)$$

where M_G , M_W , M_D , M_S and M_{PI} are the pre-industrial reservoir sizes (Table 3) and $\lambda_Q = Q_{10}^{(T_a - T_{a,PI})/10}$ with $Q_{10} = 2$ as above (Sect. 2.4). Atmosphere–land biosphere carbon dioxide flux from each vegetation zone is

$$F_{\text{CO}_2} = -\text{NPP} + \text{NPP}_{PI} \left[\frac{45}{60} \frac{M_D}{M_{D,PI}} + \frac{15}{60} \frac{M_S}{M_{S,PI}} \right] \lambda_Q. \quad (41)$$

Table 3. Coefficients for vegetation meridional limits, ϕ (δT_d), for the Northern Hemisphere and Southern Hemisphere and the global pre-industrial distribution of carbon storage and net primary production for all vegetation zones considered in the model.

		$c_1 (\times 10^{-5})$	$c_2 (\times 10^{-4})$	$c_3 (\times 10^{-3})$	$c_4 (\times 10^{-2})$	$c_5 (\times 10^{-1})$	c_6
ϕ_{TF-GSD}	NH	-1.803	-5.809	-5.168	4.970	10.920	11.280
	SH	8.413	7.339	-8.333	-8.764	-6.965	119.660
ϕ_{GSD-ET}	NH	1.152	-1.785	-4.557	4.156	10.170	37.770
	SH	-0.651	2.131	1.857	-4.100	-6.615	-35.630
		Tropical forest		Grassland, savanna and desert		Extratropical forests	
Leaves (Gt C)		30		50		20	
Wood (Gt C)		270		50		180	
Litter (Gt C)		16		40		64	
Soil (Gt C)		200		500		800	
NPP (Gt C yr ⁻¹)		25		20		15	

For isotopes ¹³C and ¹⁴C, Eqs. (37)–(41) are extended considering fractionation factors for photosynthesis and, for ¹⁴C, radioactive decay as described in Shaffer et al. (2008).

Finally, land biosphere methane and nitrous oxide productions (F_{CH_4} and F_{N_2O} , respectively) take place in soil and are proportional to the reservoir size and temperature dependent according to λ_Q , where again $Q_{10} = 2$ for both. In addition, we assume methane emissions only from wet areas (zones TF and ET). Thus, for each vegetation zone, fluxes of these two greenhouse gases are given as

$$F_{CH_4|N_2O} = \tau_{CH_4|N_2O,PI} \frac{M_S}{M_{S,PI}} \lambda_Q, \quad (42)$$

where $\tau_{CH_4|N_2O,PI}$ is the pre-industrial atmospheric lifetime of CH₄ and N₂O (9.5 and 150 years, respectively). Fluxes of ^{13,14}CH₄ are ^{13,14} $\alpha_M F_{CH_4,PI} \left(\frac{M_S^{13,14}}{M_{S,PI}} \right) \lambda_Q$, with ¹³ $\alpha_M = 0.97$ being the fractionation factor for CH₄ production. As above, we assume the ¹⁴C/¹²C fractionation to be twice as strong as that for ¹³C/¹²C (see Sect. 2.2). Fluxes to specific atmospheric boxes are equal to the biosphere fluxes within the latitudinal boundaries of the boxes.

2.7 Lithosphere module (rock weathering, volcanism and river input)

We follow the same approach as in the DCESS I model (Sect. 2.7 in Shaffer et al., 2008) by considering river inputs of phosphorus and carbon species, climate-dependent carbonate and silicate weathering rates, and lithosphere outgassing. However here we extend this approach to consider distributions of continents, river mouths (Dai and Trenberth, 2002) and volcanoes (NCEI Volcano Locations Database). In the following, we restrict ourselves to presenting the main features of this module (see Shaffer et al., 2008, again for more details).

Weathering rates of rocks containing phosphorus (W_P), as well as carbonate and silicate weathering rates (W_{Sil} and

W_{Cal}), are taken to depend on the deviation of mean atmospheric temperature from its pre-industrial value in the form

$$W_{P|Sil|Cal} = \lambda_Q W_{P|Sil|Cal,PI} = Q_{10}^{(T_s - T_{s,PI})/10} W_{P|Sil|Cal,PI}, \quad (43)$$

where $W_{P|Sil|Cal,PI}$ represents the pre-industrial weathering rates for phosphorus, silicate and carbonate and $Q_{10} = 2$ as for the other model components. Vegetation affects weathering rates by modifying surface pH through the production of CO₂ or organic acids or by altering the physical properties of soil such as erosion of exposed mineral areas and by water cycling content (Drever, 1994; Berner, 1995). Our model does not explicitly include these and other factors like a direct dependency of atmospheric pCO_2 levels (Krissansen-Totton and Catling, 2017). Such factors would add extra tuneable complexity and be beyond the scope and balance of our simplified model. Silicate weathering consumes 2 mol of atmospheric CO₂ per mole of silicate mineral weathered, while the carbonate weathering consumes only 1 mol of atmospheric CO₂ per mole of carbonate mineral weathered. Both types of weathering supply bicarbonate ion to ocean surface layers, modifying dissolved inorganic carbon and alkalinity concentrations. The phosphorus supply is equal to W_P . Therefore, expressions for total river inputs for PO₄, DIC and ALK tracers are

$$R_P = W_P = \lambda_Q W_{P,PI}, \quad (44)$$

$$R_{DIC} = 2(W_{Sil} + W_{Cal}) = 2\lambda_Q (W_{Sil,PI} + W_{Cal,PI}), \quad (45)$$

$$R_{ALK} = 2(W_{Sil} + W_{Cal}) - r_{ALKP} W_P = \lambda_Q [2(W_{Sil,PI} + W_{Cal,PI}) - r_{ALKP} W_{P,PI}]. \quad (46)$$

Values of $W_{P,PI}$, $W_{Cal,PI}$ and $W_{Sil,PI}$ are obtained from the assumed pre-industrial steady state equal to the global ocean burial rate of phosphate (B_{OxP}) and carbonate (B_{Cal}) and the assumption that $W_{Sil,PI}$ can be taken to be a fixed ratio of carbonate weathering: $W_{Sil,PI} = \gamma_{Sil} W_{Cal,PI}$, with $\gamma_{Sil} = 0.85$.

These total river inputs are distributed among the 12 ocean sectors according to the river mouth distributions mentioned above. For example, this leads to no river input to the model Southern Ocean sector.

Sources of carbon to the atmosphere are weathering of rocks containing old organic carbon (W_{OrgC}) and lithosphere outgassing (Vol). As above, $W_{\text{OrgC}} = \lambda_Q W_{\text{OrgC,PI}}$, and Vol may either be taken as a constant and equal to its pre-industrial value (Vol_{PI}) or be prescribed as an external forcing of the Earth system. Given the above together with assigned or calculated ^{13}C content for the different model inputs and outputs (including for example for organic carbon burial), overall steady-state conservation equations can be formulated for both ^{12}C and ^{13}C . These conservation equations can then be used to derive expressions for $W_{\text{OrgC,PI}}$ and Vol_{PI} as given in Shaffer et al. (2008) (their Eqs. 41 and 42). These total atmospheric carbon inputs are distributed among the six atmosphere sectors according to the same meridional distribution as carbonate and silicate weathering and volcano distribution mentioned above.

From the above, the pre-industrial steady-state equations for phosphorus, ^{12}C and ^{13}C are given by

$$W_P - B_{\text{Ogp}} = 0, \quad (47)$$

$$W_{\text{OrgC}} + \text{Vol} - \frac{\gamma_{\text{Su}}}{1 + \gamma_{\text{Su}}} B_{\text{Cal}} - B_{\text{OrgC}} = 0, \quad (48)$$

$$W_{\text{OrgC}} \delta^{13} C_{\text{OrgC}} + \text{Vol} \delta^{13} C_{\text{Vol}} - \frac{\gamma_{\text{Su}}}{1 + \gamma_{\text{Su}}} B_{\text{Cal}} \delta^{13} C_{\text{Cal}} - B_{\text{OrgC}} \delta^{13} C_{\text{OrgC}} = 0. \quad (49)$$

For the total oxygen content in the ocean–atmosphere system, the pre-industrial steady-state equation is

$$\frac{r_{\text{OCP}}}{r_{\text{CP}}} [B_{\text{OrgC}} - W_{\text{OrgC}} - f_{\text{old,OM}} \text{Vol}] + r_{\text{ONP}} (B_P - W_P) = 0, \quad (50)$$

where r_{ONP} , r_{OCP} and r_{CP} are as mentioned in Sect. 2.4 and $f_{\text{old,OM}}$ is the fraction of Vol originating from old organic matter that results from the above conservation calculations for ^{12}C and ^{13}C .

3 Model solution, calibration and validation

3.1 Pre-industrial steady-state solution

3.1.1 Solution procedure

The ocean module equations are discretized on a staggered grid type, with tracer values defined at the center of boxes and velocities and diffusivities determined at box edges. Centered differences are used for derivatives, diffusion and vertical advection, whereas an upwind scheme is used for the coarsely resolved meridional advection. Prognostic equations for the

atmosphere (including snow and sea ice cover), land biosphere, lithosphere and ocean modules are solved simultaneously using a fourth-order Runge–Kutta algorithm with a 2-week time step. Prognostic equations for the ocean sediment are solved by simple time stepping with a 1-year time step. The complete coupled model is written in Fortran language and runs at a speed of about 10 kyr of simulation per 30 min of computer time on a high-end personal computer.

3.1.2 Calibration procedure

For model calibration we used an approach similar to that in Shaffer et al. (2008) but here consisting of six steps. For the first step we considered the atmospheric module with atmospheric $p\text{CO}_2$, $p\text{CH}_4$ and $p\text{N}_2\text{O}$ set to their pre-industrial values (280, 0.72 and 0.27 μatm , respectively) and a slab ocean for air–sea heat exchange. We adjusted the free parameters listed in Table 1 to give a steady-state global annual mean atmospheric temperature of 15 °C and a climate sensitivity of 3 °C per doubling of CO_2 as indicated by several lines of evidence and model estimates (Meehl et al., 2020; Zelinka et al., 2020; IPCC, 2021), a poleward transport of heat and water vapor consistent with observations, and annual mean latitudes and seasonal-cycle amplitudes of sea ice lines in accordance with observed data. In the second step we couple the physics part of the ocean module to the physics part of atmosphere module, and physical ocean free parameters (Table 2) were adjusted in order to get the best fit to observed mass and heat transport as well as to temperature and salinity distributions. In the third step we couple the land biosphere to the previously calibrated “physics model” version, and we adjust free parameters of the set of functions $f(I)$ in Eq. (36) to give observed annual mean NPP values for each vegetation zone as well as their annual-cycle amplitudes from observations. This largely sets the modeled annual cycle of atmospheric carbon dioxide of each atmospheric box. In the fourth step we incorporate ocean biogeochemical tracers PO_4 , $\text{DI}^{12,13,14}\text{C}$, ALK and O_2 into the model version of step three. For calibration we start with homogeneous vertical values of 2.17×10^{-3} , 2.32 and 2.43 mol m^{-3} for PO_4 , DIC and ALK, respectively (in the following, for simplicity, DIC will be used to mean DI^{12}C). Furthermore, in this step we use a fixed atmospheric O_2 equal to 0.2095 atm, an atmospheric $\delta^{13}\text{C}$ equal to -6.5‰ and an atmospheric ^{14}C production chosen to keep $\Delta^{14}\text{C}_{\text{atm}} \sim 0\text{‰}$ (Sarmiento and Gruber, 2006; Shaffer et al., 2008). At this stage we assume that all biogenic particles falling to the ocean bottom remineralize completely there. We then made initial guesses for the values of the biogeochemical free parameters of the ocean module listed in Table 2. These choices were partially based on the DCESS I model (Shaffer et al., 2008). The atmosphere–land biosphere–ocean model was spun up with uniform atmosphere and ocean tracer distributions to a steady state after about 10 000 model years, and results were compared with atmosphere, land biosphere and ocean data. Then all param-

eter values were adjusted by trial and error in order to get steady-state solutions that better satisfied requirements described in the previous steps as well as observed global annual mean distributions of T , S , PO_4 , DIC , ALK and dissolved O_2 .

In the fifth calibration step, we coupled the sediment module to the step-four calibrated model. For conservation, the total burial rate of a tracer was added to the ocean surface layer of each sector under consideration of the present-day river distribution. After solving this new closed system for a new pre-industrial steady state, we adjusted all free parameters in order to obtain steady-state solutions that better satisfied the data-based constraints of the previous calibration steps. In the sixth and final calibration step, we coupled the lithosphere module to the step-five calibrated model, whereby river inputs are equated with tracer burial fluxes from the fifth calibration step (tracer burial fluxes are now leaving the system). In addition, weathering rates and lithosphere outgassing were calculated from the tracer burial fluxes and the assumption of the pre-industrial steady state for phosphorus and $^{12,13}\text{C}$ (Sect. 2.7). A last slight trial-and-error adjustment is made to satisfy the data-based requirements from all previous calibration steps. For this final calibration, we make a long run until a steady state is achieved such that all model components vary less than 0.001 % during 1000 model years. Resulting global annual means for atmospheric temperature and CO_2 , CH_4 and N_2O atmospheric partial pressures are 15.12 °C and 279.96, 0.72 and 0.27 μatm , respectively. For atmospheric isotopes, this final calibration gives a global mean atmospheric $\delta^{13}\text{C}$ of -6.53‰ and a ^{14}C atmospheric production of 1.66×10^4 atoms $\text{m}^{-2} \text{s}^{-1}$, respectively. Global mean ocean values are 2.16 and 145.07 mmol m^{-3} for PO_4 and dissolved O_2 , respectively, and 2.30 and 2.41 mol m^{-3} for DIC and ALK , respectively.

3.1.3 Atmosphere tracers and transport results

The steady-state, pre-industrial solution gives the annual mean atmospheric temperatures of 15.4 °C for the Northern Hemisphere and 14.8 °C for the Southern Hemisphere, whereas annual mean sea ice extensions for the Northern Hemisphere (Arctic and North Pacific sectors) and Southern Hemisphere are 66.2° N, 64.9° N and 63.2° S, respectively. While the Southern Ocean model result is close to the observed value ($\sim 64^\circ \text{S}$), our Arctic Ocean sea ice line position is about 7° too far south with respect to observational estimates (Fetterer et al., 2017). This could be attributable to ocean and sea ice dynamics that are not captured in our simplified, zonally averaged model. The Northern Hemisphere snow line is found at 58.8° N. Annual mean poleward atmospheric heat transports across 35° N/S and 55° N/S are 4.4/4.8 and 3.1/3.4 PW, and poleward water vapor transports in the atmosphere at the same latitudes are 0.76/0.82 and 0.43/0.45 Sv, respectively. These model re-

sults agree well with observational estimates (Trenberth and Caron, 2001). The seasonal cycle of sea ice is relatively well represented in the model, with a maximum (minimum) extension at the end of winter (summer) and with amplitudes of 4.7 and 9.0° for the Arctic and Southern oceans, respectively, with differences of 0.4 and 0.9° with respect to observed estimates (Fetterer et al., 2017). We believe that model–data disagreement in sea ice is not only due to the simplicity of parameterization, but also due to the anthropogenic signal in the modern-day sea ice data. The annual mean model difference in atmospheric $p\text{CO}_2$ between the Northern Hemisphere and Southern Hemisphere is only 0.7 μatm , a somewhat lower value than observations. However, much of this difference could be explained by the effect on the observations of NH anthropogenic CO_2 emissions. On the other hand, the atmospheric $p\text{CO}_2$ seasonal-cycle amplitude of 4.6 and 0.9 ppm for the Northern Hemisphere and Southern Hemisphere, respectively, agrees rather well with monthly-mean observations from the Mauna Loa and Cape Grim observatories. This annual-cycle amplitude responds strongly to the annual land vegetation dynamics as well as to the ocean–land distribution between the Northern Hemisphere and Southern Hemisphere. The Southern Ocean plays a role here as well by dampening the Southern Hemisphere cycle amplitude.

3.1.4 Ocean circulation and heat transport results

The steady-state, pre-industrial model has the large-scale ocean circulation shown in Fig. 3. There are two meridional cells in the model Atlantic Ocean. The upper clockwise cell is the Atlantic Meridional Overturning Circulation (AMOC) with a maximum transport of 19 Sv near 1000 m depth in the northern North Atlantic and a maximum depth of about 3500 m. Below 2000 m depth the flow returns southward to the Southern Ocean, where upwelling is below the Drake Passage sill depth (2000 m), largely in response to the surface northward Ekman transport at 55° S. Both the intensity and the depth penetration of modeled AMOC are in line with observed data and complex model results (Talley et al., 2003; Hirschi et al., 2020). The lower counterclockwise cell carries mainly AABW, which fills the whole abyssal Atlantic. The upper southward branch of this cell returns to the Southern Ocean and upwells there.

The Pacific Ocean overturning circulation is dominated by a counterclockwise cell carrying AABW which fills the whole deep ocean. The lower branch of the northward flow in this cell upwells in the North Pacific and returns southward in a near-surface flow. The upper branch of the northward flow in this cell upwells and returns southward to the Southern Ocean below 2000 m without crossing the Equator. There is also a second counterclockwise cell carrying Antarctic Intermediate Water (AAIW) north of the Equator above 2000 m depth. The upper southward branch of this cell joins the southward, near-surface flow of the deep counterclockwise cell described above. There is a weak clockwise

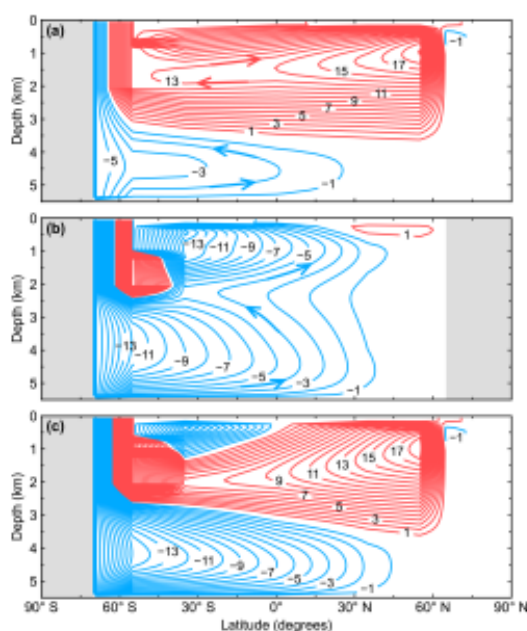


Figure 3. Pre-industrial, steady-state model representation of the meridional overturning circulation (Sv) for (a) the Atlantic Ocean, (b) the Pacific Ocean and (c) the global ocean. Red contours (positive values) represent clockwise circulation, and blue contours (negative values) represent counterclockwise circulation, as indicated schematically by arrows.

cell confined above 500 m depth in the North Pacific related in part to the imposed model outflow to the Arctic Ocean through the Bering Strait.

The mediterranean Arctic Ocean presents an estuarine-type meridional circulation of 1 Sv intensity entering at 700 m depth and flowing out at 300 m depth. This counterclockwise circulation is maintained mainly by the zonally averaged geometry and freshwater inputs from precipitation and runoff. The Southern Ocean shelf produces 5.4 Sv of overflow water, which after entrainment increases its volume to $\sim 16 Sv$ upon outflow in the deep Southern Ocean. This agrees quite well with observed estimates (Orsi et al., 2002; Gordon, 2019). Such realistic entrainment and subsequent AABW formation, as achieved in the model with the prescribed present-day Antarctic continental slope (Amante and Eakins, 2009), underline the usefulness of our simplified gravity current approach to this problem.

Northward ocean heat transport is found throughout the Atlantic Ocean, peaking at 35° N with 0.83 PW and falling subsequently to 0.75 and 0.19 PW at 55 and 65° N, respectively. The high value at 55° N is related to the maximum ocean circulation intensity there. The South Atlantic carries

0.37 and 0.34 PW northward at 35 and 55° S, respectively. The North Pacific Ocean transports heat northward, with values of 0.41 and 0.29 PW at 35 and 55° N, respectively. The South Pacific Ocean transports heat southward, peaking at 35° S with 1.21 and 0.84 PW at 55° S. At the Equator, the Atlantic and the Pacific oceans transport heat in opposite directions with 0.65 PW northward and 0.37 PW southward, respectively. All modeled ocean transports agree well with data-based estimates (Trenberth and Caron, 2001), except at 55° N, where the modeled value is greater than observations.

3.1.5 Ocean tracer and biological-production results

Model ocean profiles of T , S and $\delta^{18}O_w$ are plotted together with observational data in Fig. 4 (all observed data shown in Figs. 4–7 are from the Global Ocean Data Analysis Project version2.2022 (GLODAPv2; Lauvset et al., 2022), except for those of $\delta^{18}O_w$, where data are from the Global Seawater Oxygen-18 Database – v1.22 (Schmidt, 1999; Bigg and Rohling, 2000) have been used). In general, there is good model–data agreement, especially at mid-depths and in the deep and abyssal ocean. In the upper ocean, the model profiles are well within the observed mean range values. In particular for temperature, the model captures surface–deep-ocean transitions quite well in most of the model ocean sectors. Modeled temperatures in the Arctic Ocean below 1000 m are about 3.5 °C warmer than observations, likely reflecting the extensive ocean area covered by sea ice and/or the lack of local deepwater formation mechanisms like wintertime coastal polynyas in our simplified model. South of 35° S, model temperature falls at the warm end of the observed data.

Model salinity is quite well represented and captures prominent features of the global ocean, such as the salinity minimum at 650 and 1050 m depth for the msA and msP sectors representing the AAIW; the relative surface minimum in the mnP and hnP sectors associated with North Pacific Intermediate Water (NPIW; Sverdrup et al., 1942); and the vertical salinity structure in the Arctic Ocean with a surface salinity minimum, associated with freshwater inputs from runoff, sea ice melt and snowmelt and the strong halocline as found in observations (Aagaard et al., 1981). The lack of equatorial upwelling in our simplified model may explain the relatively warm and salty waters in the northern and southern tropical sectors. For $\delta^{18}O_w$, the model captures the vertical distribution as well as the meridional gradient in each model sector well, reflecting the global evaporation–precipitation distribution associated with isotopic fractionation of water.

Model ocean profiles of PO_4 and O_2 are plotted together with observational data in Fig. 5. The model achieves a good fit to the observed values in almost all ocean model sectors although the model results for O_2 are slightly lower than observed for the mid-depth Atlantic Ocean. Surface phosphate is strongly controlled by ocean new production. Low surface values are found in all ocean sectors, except at the South-

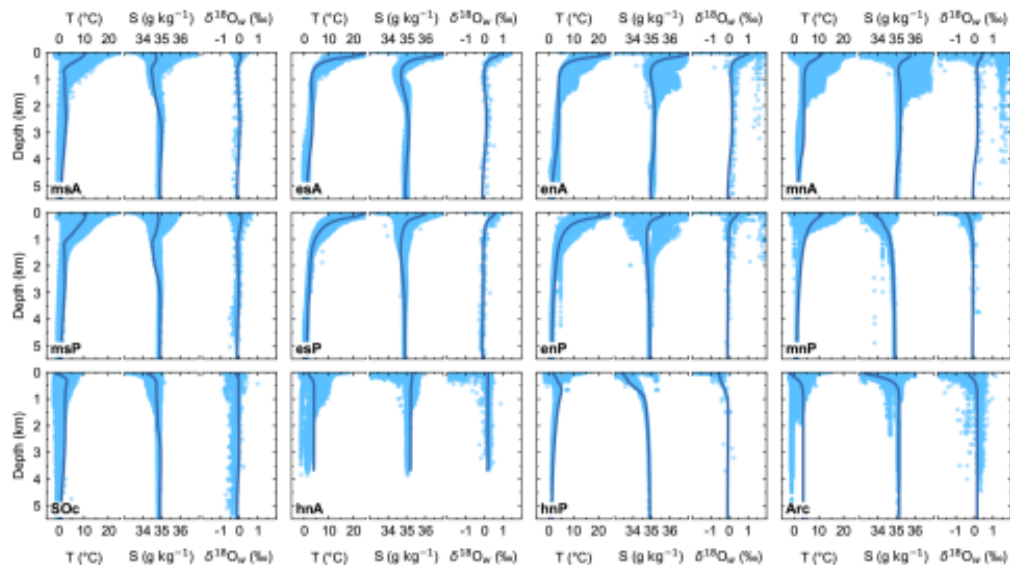


Figure 4. Pre-industrial, steady-state model ocean vertical profiles (dark-blue lines) of conservative temperature (T), absolute salinity (S) and water ^{18}O isotopic excursion ($\delta^{18}\text{O}_w$) compared to observed data (light-blue dots) for each ocean model sector shown in Fig. 1a. T and S are compared with data from the GLODAPv2 database (Lauvset et al., 2022); $\delta^{18}\text{O}_w$ values are compared with data from the Global Seawater Oxygen-18 Database – v1.22 (Schmidt, 1999; Bigg and Rohling, 2000, <https://data.giss.nasa.gov/o18data/>, last access: 23 November 2023).

ern Ocean, where the highest surface values are found due to intense upwelling and to the low biological-production efficiency, as expected from the low value of L_f in our model. Furthermore, the model captures differences between the Pacific Ocean and Atlantic Ocean basins well. These differences are largely a consequence of the large-scale ocean circulation as described above. The oldest waters are found at the North Pacific Ocean (model sectors mnP and hnP; see $\Delta^{14}\text{C}$ model profiles in Fig. 6), and consequently, the highest (lowest) values of phosphate (dissolved oxygen) in the ocean interior are found there. High dissolved O_2 values both at the surface and in the abyssal ocean are relatively well represented in the model in response to air–sea gas exchange and AABW ventilation. At the ocean interior, O_2 distributions respond mainly to organic matter remineralization and, for the msA and msP sectors for example, ventilation from AAIW. Misrepresentation of PO_4 and dissolved O_2 above 1000 m depth in the hnP sector is related to the way NPIW is treated in the model. The PO_4 (dissolved O_2) excess (deficit) in the Arctic model sector is related to the overestimation in ocean temperature there, which influences organic matter remineralization.

The ocean carbon cycle model tracers DIC and ALK are plotted together with observed DIC and ALK in Fig. 6. The comparison with observational data shows excellent model–data agreement for both DIC and ALK. Both the

vertical structure and the spatial differences among ocean model sectors are well captured by the model. Furthermore, both the depths of the DIC maximum and the slightly shallower depths of the PO_4 maximum (Fig. 5) in well-stratified ocean zones agree well with observations, indicating good ϵ -folding length choices used for model remineralization rates. These distributions reflect the interplay between the cycling of organic matter and calcite as well as the air–sea exchange of CO_2 .

Vertical distributions of carbonate ion (CO_3^{2-}), CO_3^{2-} saturation with calcite (CO_3^{2-} _{sat}) and water CO_2 are plotted in Fig. 7. The crossing point between CO_3^{2-} and CO_3^{2-} _{sat} is the calcite saturation depth (CSD), which is found to be at around 4000 m depth for the entire Atlantic Ocean and which reaches a minimum depth of around 700 m in the North Pacific sector, where the maximum water CO_2 concentration even exceeds that of CO_3^{2-} . These results showing undersaturation throughout most of the deep North Pacific Ocean would imply low values of CaCO_3 in ocean sediments there. This is confirmed by the results for modeled and observed ocean sediments presented below.

Ocean carbon isotopes ($\delta^{13}\text{C}$ and $\Delta^{14}\text{C}$) are plotted together with observational data in Fig. 8. As with DIC and ALK, there is excellent model–data agreement in nearly all model ocean zones. As light carbon is preferentially taken up during photosynthesis, export of organic matter leaves the

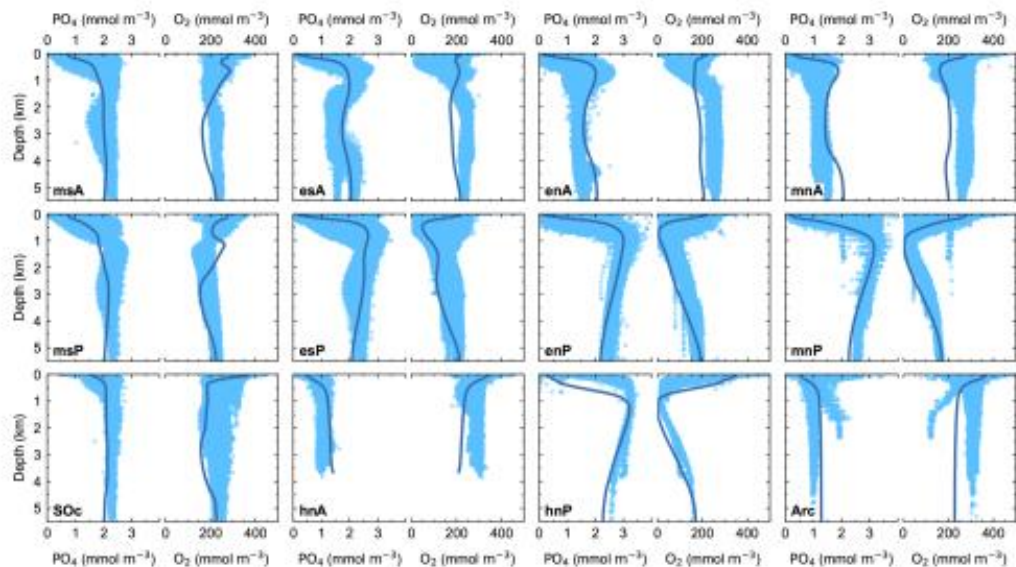


Figure 5. Pre-industrial, steady-state model ocean vertical profiles (dark-blue lines) of phosphate (PO_4) and dissolved oxygen (O_2) compared to observed data (light-blue dots) for each ocean model sector shown in Fig. 1a. Observed values are from the GLODAPv2 database (Lauvset et al., 2022).

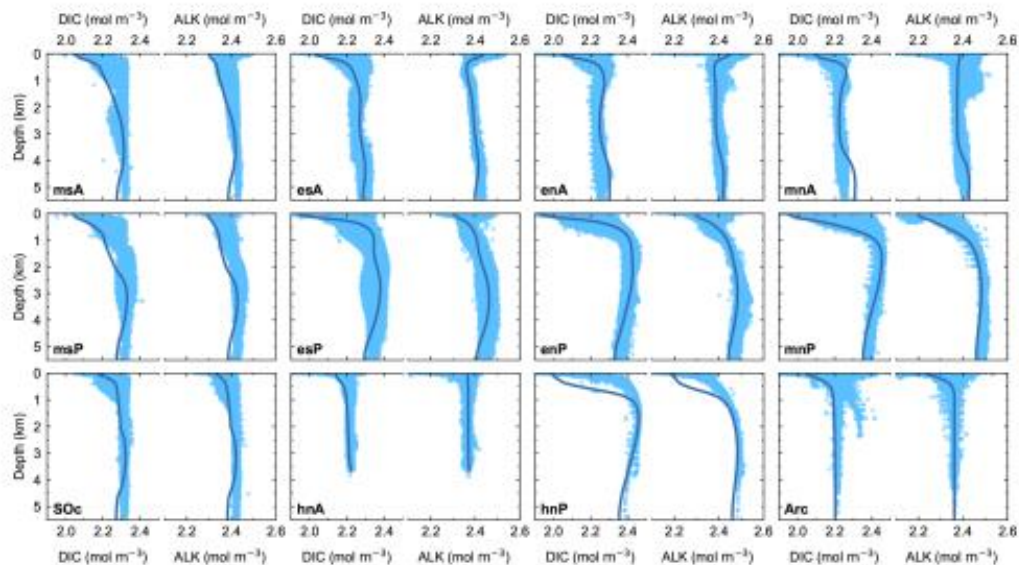


Figure 6. Pre-industrial, steady-state model ocean vertical profiles (dark-blue lines) of total dissolved inorganic carbon (DIC) and alkalinity (ALK) compared to observed data (light-blue dots) for each ocean model sector shown in Fig. 1a. Observed values are from the GLODAPv2 database (Lauvset et al., 2022).

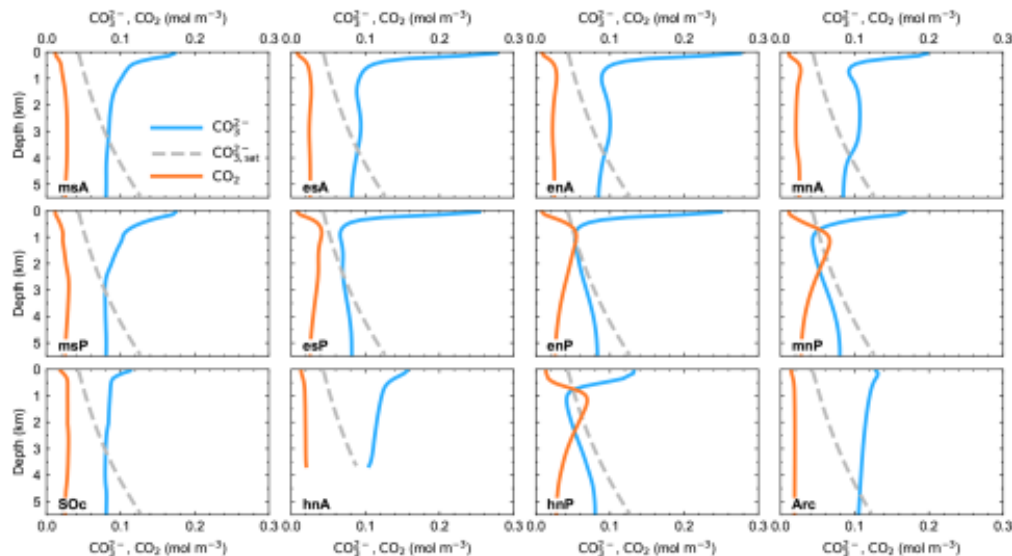


Figure 7. Pre-industrial, steady-state model ocean vertical profiles of carbonate ion (CO_3^{2-}), carbonate ion saturation with calcite (CO_3^{2-})_{sat} and water CO_2 for each ocean model sector shown in Fig. 1a.

euphotic zone enriched in ^{13}C (higher values of $\delta^{13}\text{C}$). Upon remineralization of this organic matter at depth, light carbon is released into the water column, leaving the water there depleted in ^{13}C (lower values of $\delta^{13}\text{C}$). As shown by the agreement of model $\delta^{13}\text{C}$ results with ocean as well as atmosphere data, the model deals well with this fractionation process as well as with the temperature-dependent fractionation associated with air–sea exchange of CO_2 . As for PO_4 and O_2 , meridional gradients and Pacific–Atlantic Ocean differences reflect ocean circulation, as seen clearly in the $\Delta^{14}\text{C}$ profiles. The oldest waters are found in the North Pacific and exhibit the most negative values of $\delta^{13}\text{C}$ and $\Delta^{14}\text{C}$ in the ocean interior due to a longer time for receiving light carbon from organic matter remineralization and a longer time for radioactive decay to act, respectively. Modeled surface ocean $\delta^{13}\text{C}$ values are well within the data-based estimates, with a global surface mean model result of 2.15‰. As before, the model–data disagreement of $\delta^{13}\text{C}$ in the upper 1000 m depth in the hnP sector is related to NPIW formation in the model.

With all the above and despite minor model–data disagreement, the model reproduces the main global features of both physical and biogeochemical tracers quite well. Better ocean modeled distributions of S , $\delta^{18}\text{O}_w$, DIC, ALK, $\delta^{13}\text{C}$ and $\Delta^{14}\text{C}$ are key improvements that have been made in comparison to the much simpler DCESS I model, where distributions of those tracers had shortcomings, in particular for S , $\delta^{18}\text{O}_w$ and $\delta^{13}\text{C}$ (Shaffer et al., 2008).

Model global ocean new (exported) production (NP) is $5.84 \text{ Gt C yr}^{-1}$, slightly higher than the 5.4 Gt C yr^{-1} of the DCESS I model (Shaffer et al., 2008). This new estimate is at the lower end of the estimates from Dunne et al. (2007) ($9.6 \pm 3.6 \text{ Gt C yr}^{-1}$) but almost matches a modern and possibly more robust estimate of Siegel et al. (2014) of $5.90 \text{ Gt C yr}^{-1}$. The tropical ocean model zones (35°S – 35°N) are by far the most productive model regions, accounting for more than 66 % of global exported production partitioned into 53 % and 13 % for the Pacific and Atlantic oceans, respectively. The Arctic Ocean and high-latitude northern zone of the Pacific Ocean have the lowest values of exported NP, with 0.2 % and 1.1 % of the total, respectively. The Southern Ocean also has a rather low value, with 5 % of total export production. Northern and southern mid-latitude model sectors (35 – 55°N/S) show around 22 % of total NP, with 5 % and 7 % for the mnP and mnA sectors, respectively, and 8 % and 2 % for the msP and msA sectors, respectively. This meridional distribution is also observed in the publications cited above. We believe that the lack of equatorial upwelling of nutrient-rich waters in the model probably contributed to the relatively low value of ocean NP in our model.

Global biogenic calcite production in the model is $1.25 \text{ Gt C yr}^{-1}$, and more than 65 % is produced in tropical model zones of the Pacific Ocean. Tropical zones of the Atlantic Ocean account for only 16 % of global calcium carbonate production. Extratropical ocean model zones from the Northern Hemisphere and Southern Hemisphere, combining

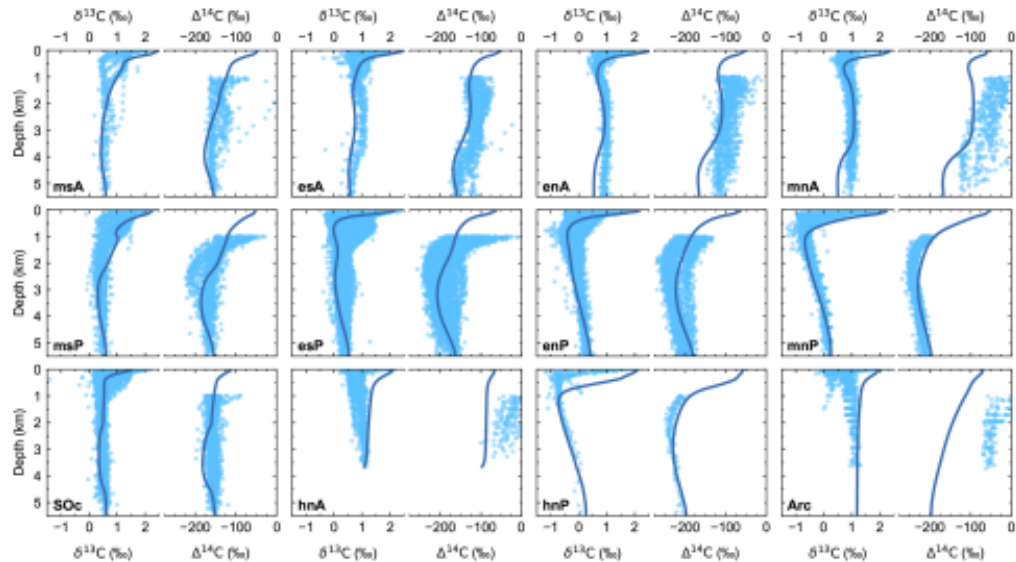


Figure 8. Pre-industrial, steady-state model ocean vertical profiles (dark-blue lines) of isotopic excursion of ^{13}C ($\delta^{13}\text{C}$) and isotopic excursion of ^{14}C ($\Delta^{14}\text{C}$) compared to observed data (light-blue dots) for each ocean model sector shown in Fig. 1a. Observed values are from the GLODAPv2 database (Lauvset et al., 2022). For $\Delta^{14}\text{C}$, only values below 1000 m depth have been plotted as shallower depths are strongly affected by the anthropogenic signal including atomic-bomb ^{14}C inputs. Note that bomb ^{14}C also affects deeper levels in the North Atlantic and Arctic sectors (mnA, hnA and Arc).

the Pacific and Atlantic sectors, represent only 15 % of total biogenic calcite production. Table 4 shows values for organic matter and calcite production for each ocean model sector.

Our estimates are well into the observed range of 0.5–1.6 Gt C yr^{-1} of Berelson et al. (2007) but slightly higher than more recent estimates of $0.91 \pm 0.14 \text{ Gt C yr}^{-1}$ (Sulpis et al., 2021). Overall, our model result of new (exported) production is well into the range of CMIP6 models (Planchat et al., 2023), but our biogenic calcite production is at the upper end of those model estimates. However, we note that CMIP6 ensemble results tend to globally underestimate the exported inorganic carbon compared to observational estimates (Planchat et al., 2023).

The calcite carbon-to-organic carbon flux ratio is similar for the Pacific/Atlantic oceans, with ratios of 0.6/0.5, 0.9/0.7 and 1.2/1.1 in the tropical model sectors at 1000, 2000 and 3000 m depth, respectively, and ratios of 0.2, 0.3 and 0.5 for northern-latitude sectors of those basins at these depths. These ratios are somewhat lower than those estimated from sediment trap data (Berelson et al., 2007). The longer e -folding scale ξ_{Ca} than ξ_{C} and the temperature effect on organic matter remineralization and on the CaCO_3 rain ratio (see Sect. 2.4) help explain these results.

3.1.6 Sediment results

In the model pre-industrial steady state, 0.11 Gt C yr^{-1} of organic carbon is buried in ocean sediments. This represents 12 % of total organic carbon falling on the sediment surface; the remaining 88 % is remineralized to DIC, which returns to the water column. This modeled value is well within the range of data-based estimations (Bernier, 1982; Hedges and Keil, 1995; Cartapanis et al., 2018). However, the higher ends of some of these estimates may include contributions from estuaries and delta environments that our model does not consider. Other modeled results are in the range of 0.02–0.09 Gt C yr^{-1} (Bernier, 1991; Munhoven, 2007; Willeit et al., 2023). More than 90 % of our modeled burial takes place at water depths shallower than 1000 m such that 0.011 Gt C yr^{-1} is buried below this depth, in agreement with deep-sea burial estimates (Hayes et al., 2021). The highest modeled burial rates for organic carbon per ocean sector are found in the tropical Pacific Ocean and the North Atlantic Ocean (35–65°N) sectors with over 40 % and 27 %, respectively, of the total organic carbon burial. The global inventory of bioturbated-layer (BL) organic carbon is 122 Gt C , somewhat higher than that found in the pre-industrial DCESS I model simulation (92 Gt C).

For calcite, the global annual mean burial rate is 0.21 Gt C yr^{-1} , and more than 57 % takes place in the tropi-

Table 4. Pre-industrial organic matter and biogenic calcite ocean production estimates. All values are given in Gt C yr^{-1} .

Ocean limits	Atlantic Ocean		Pacific Ocean	
	Organic matter	Biogenic calcite	Organic matter	Biogenic calcite
65–55° N	0.20	0.01	0.07	3.52×10^{-3}
55–35° N	0.38	0.06	0.30	0.04
35° N–0°	0.43	0.12	1.34	0.35
0°–35° S	0.35	0.09	1.80	0.47
35–55° S	0.15	0.02	0.47	0.07
	Southern Ocean (55–70° S)		Arctic Ocean (90–65° N)	
	0.31	0.01	0.02	5.43×10^{-4}

cal Pacific sectors and 23 % is buried at the combined northern tropical and mid-latitude Atlantic Ocean sectors. Our global result compares well with data-based estimations and model results in the range of $0.13\text{--}0.45 \text{ Gt C yr}^{-1}$ (Milliman and Droessler, 1995; Cartapanis et al., 2018; Hayes et al., 2021; Willeit et al., 2023). Of the total annual mean burial rate of CaCO_3 in the Pacific and Atlantic oceans (0.14 and $0.07 \text{ Gt C yr}^{-1}$, respectively), 49 % and 45 % of calcite, respectively, is buried at depths greater than 1000 m in these basins. Other estimates also show such a nearly half-and-half shelf-slope vs. deep-ocean division (Milliman, 1993). The modeled global ocean mean calcite dry-weight fraction $(\text{CaCO}_3)_{\text{dwt}}$ is 0.349, whereas the Pacific and Atlantic oceans present mean values of $(\text{CaCO}_3)_{\text{dwt}}$ of 0.353 and 0.440, respectively, where the highest values are found in the tropical South Pacific and North Atlantic sectors, with values of 0.459 and 0.553, respectively. The model global inventory of bioturbated-layer calcite carbon is 767 Gt C, somewhat lower than the DCESS I pre-industrial estimate (1010 Gt C) but in good agreement with the 800 Gt C data-based estimate from Archer (1996). Of this, 503 Gt C is found in the Pacific Ocean BL and 249 Gt C in the Atlantic Ocean one, equivalent to 66 % and 32 % of the total, respectively. The results above highlight how the model captures ocean carbon cycle differences between the Pacific and Atlantic oceans.

Figure 9 shows the dry-weight fractions of organic matter $(\text{OM})_{\text{dwt}}$ and calcite $(\text{CaCO}_3)_{\text{dwt}}$ as well as the sediment velocity out of the bottom of the BL (w_{sed}) for each ocean model sector. In general, relatively high $(\text{OM})_{\text{dwt}}$, relatively low $(\text{CaCO}_3)_{\text{dwt}}$ and rapid sedimentation rates are found at shallow depths. This can be explained mainly by the high prescribed flux of non-calcite minerals at such depths that (1) fill the BL mainly with such minerals and (2) rapidly flush the BL, thereby promoting high $(\text{OM})_{\text{dwt}}$ burial since relatively little organic matter is remineralized in the BL on such short timescales. At intermediate depths above the model's CSD, $(\text{CaCO}_3)_{\text{dwt}}$ is higher, $(\text{OM})_{\text{dwt}}$ is lower and sedimentation rates are more moderate. This results not only from enhanced CaCO_3 accumulation in sediments bounded by ocean layers supersaturated with carbonate ion (see Fig. 7), but

also from much lower non-calcite mineral and organic matter rain rates, leading to slower BL flushing that allows more complete organic matter remineralization. At those intermediate depths, the modeled effect of dissolved oxygen on organic matter remineralization can be seen in the North Pacific model sectors, where this remineralization is slowed down considerably as ocean layers there become nearly suboxic/anoxic. This also leads to a local increase in sediment rates. In the deep ocean below the model's CSD, rapid decreases in CaCO_3 content, very low organic matter contents and slower sedimentation rates are the result of calcite dissolution combined with low constant non-calcite rain rates and still lower organic matter rain rates. The Arctic Ocean model sediment is almost completely composed of non-calcite mineral because the sediment flux of biogenic material falling on the sediment surface is very small due to the extremely limited surface new production. In the Southern Ocean, model sediment is also composed mainly of non-calcite minerals but contains larger fractions of $(\text{OM})_{\text{dwt}}$ and $(\text{CaCO}_3)_{\text{dwt}}$ than in the Arctic Ocean. The water depth of the calcite compensation depth (CCD), defined operationally where $(\text{CaCO}_3)_{\text{dwt}}$ equals 0.1, is found at around 4800 m for both the tropical Pacific and the tropical Atlantic Ocean sectors. In contrast, there are major differences between the North Atlantic and North Pacific sectors, with CCD depths of around 4400 and 2100 m depth, respectively.

3.1.7 Lithosphere results

Table 5 lists model weathering and burial rates for the pre-industrial steady state. From weathering–burial steady-state balances outlined in Sect. 2.7 and global mean values of ^{13}C isotope excursions for organic carbon ($\delta^{13}\text{C}_{\text{OrgC}} = -22.06\text{‰}$) and carbonate ($\delta^{13}\text{C}_{\text{Carb}} = 2.22\text{‰}$) obtained from the fifth calibration step, modeled outgassing from volcanoes is found to be $0.140 \text{ Gt C yr}^{-1}$, in good agreement with modern-day data-based estimates (IPCC, 2021). Results for carbonate and silicate weathering rates are similar to those found with the DCESS I model, 0.109 and $0.092 \text{ Gt C yr}^{-1}$, respectively (Shaffer et al., 2008). Our carbonate weathering

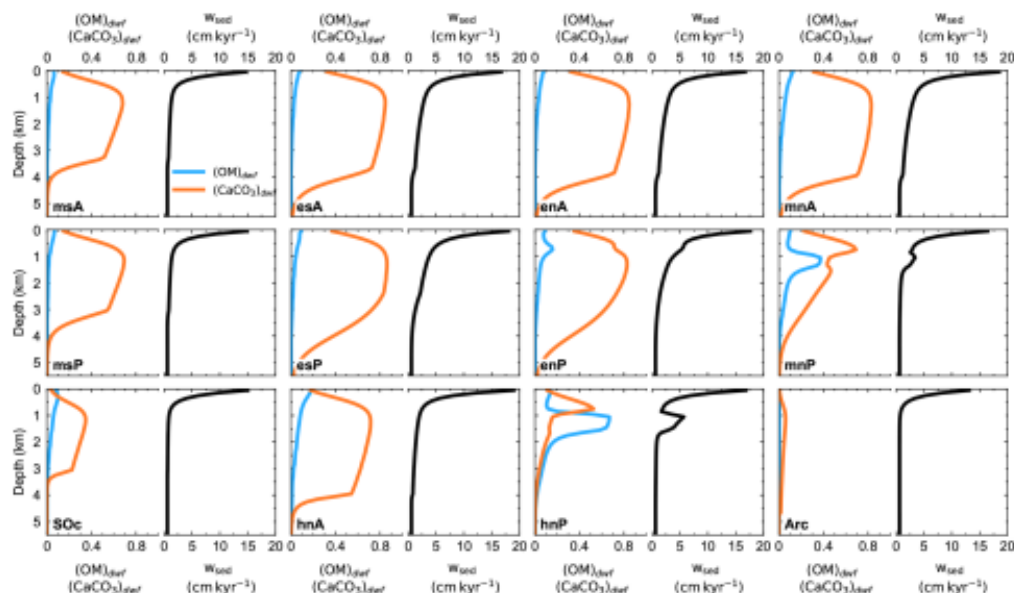


Figure 9. Pre-industrial, steady-state model sediment vertical profiles of dry-weight fractions of organic matter, $(OM)_{dwf}$, and calcite, $(CaCO_3)_{dwf}$, as well as sedimentation velocity (w_{sed}), all at the base of the bioturbated layer of each ocean model sector shown in Fig. 1a.

rate is well into the range of other observational and model estimates, $0.088\text{--}0.241\text{ Gt C yr}^{-1}$, but our silicate weathering rates are somewhat lower than other corresponding estimates, $0.122\text{--}0.236\text{ Gt C yr}^{-1}$ (Gaillardet et al., 1999; Ludwig et al., 1999; Munhoven, 2002; Hartmann et al., 2009; Lenton et al., 2018; Willeit et al., 2023). Phosphorus weathering rates are higher than those found in the DCESS I model, $1.663 \times 10^3\text{ mol P s}^{-1}$, but are in better agreement with observational estimates, $2.019 \times 10^3\text{--}3.071 \times 10^3\text{ mol P s}^{-1}$ (Filippelli, 2002; Paytan and McLaughlin, 2007). Organic carbon weathering rates agree well with recent estimations of $0.068\text{ Gt C yr}^{-1}$ (Zondervan et al., 2023). Based on these results, although simple, our continental weathering–climate relationship gives reasonable results when compared against models with more complicated relationships.

The modeled river input of total inorganic carbon is 0.43 Gt C yr^{-1} , a value close to that found in the DCESS I model (0.40 Gt C yr^{-1}) and close to the 0.41 Gt C yr^{-1} from data-based estimates (Li et al., 2017). More than 51 % of this river input flux is delivered to the Atlantic Ocean, while 40 % drains into the Pacific Ocean and the rest into the Arctic Ocean. The Southern Ocean does not receive inorganic carbon from rivers. With the results above, modeled steady-state, pre-industrial global ocean outgassing of CO_2 is 0.11 Gt C yr^{-1} , which is balanced by net uptake of atmospheric CO_2 that is expressed as $2W_{SiL,PI} + W_{CaL,PI} - (Vol_{PI} + W_{OrgC,PI})$.

Table 5. Weathering, lithosphere outgassing and burial estimates for pre-industrial, steady-state balances.

Property	Symbol	Estimated value
Phosphorus weathering	$W_{P,PI}$	$2.507 \times 10^3\text{ mol P s}^{-1}$
Organic carbon weathering	$W_{OrgC,PI}$	$0.064\text{ Gt C yr}^{-1}$
Carbonate weathering	$W_{CaL,PI}$	$0.115\text{ Gt C yr}^{-1}$
Silicate weathering	$W_{SiL,PI}$	$0.098\text{ Gt C yr}^{-1}$
Lithosphere outgassing	Vol_{PI}	$0.140\text{ Gt C yr}^{-1}$
Organic carbon burial	$B_{OrgC,PI}$	$0.106\text{ Gt C yr}^{-1}$
Carbonate burial	$B_{CaL,PI}$	$0.213\text{ Gt C yr}^{-1}$

3.2 Testing the model

We carry out two simple experiments to test model performance. In the first experiment (Exp 1), we force the model with an imposed, time-dependent function of northward Ekman transport out of the Southern Ocean at 55°S . We considered two cases for this experiment, doubling (Exp 1a) and halving (Exp 1b) this transport value on a timescale of 1500 years. With this, we try to emulate the role of Southern Ocean westerly winds in large-scale ocean circulation as it has been hypothesized that intensity and position shifts of these winds may drive global-scale climate changes on glacial–interglacial timescales (Gray et al., 2023; Lee et al., 2011; Toggweiler et al., 2006). In the second

experiment (Exp 2), we force the model with an imposed, time-dependent function of freshwater input to the Southern Ocean shelf to emulate a melting pulse of the Antarctic ice sheet. We “melt” the equivalent of $2.5 \times 10^{15} \text{ m}^3$ of freshwater (equivalent to 5 m sea level rise) over two different timescales: a fast pulse to get a sea level rise of 1 m (Exp 2a) and a slow pulse to get a 0.1 m rise (Exp 2b) after 250 years of model simulation. This is consistent with modeled assessments about Antarctic ice sheet retreats in the present climate context (Ruckert et al., 2017; DeConto and Pollard, 2016). In both experiments, we focus on changes in large-scale ocean circulation and their impact on ocean tracer distributions as well as on the global climate.

3.2.1 Southern Ocean Ekman transport forcing

The forcing and model results are presented in Fig. 10. With the increase in northward Ekman transport (Exp 1a) across 55° S , there is more upwelling in the Southern Ocean sector (Fig. 10b). However, this Southern Hemisphere forcing does not significantly impact AMOC intensity in the North Atlantic Ocean, as shown by the streamline evolution at 55° N at 1000 m depth (Fig. 10e). Rather, this forcing leads to the appearance of a clockwise recirculation cell between 55 and 40° S confined between 1000 and 2000 m depth for both the Atlantic and the Pacific oceans, as indicated by the vertical flux (defined as positive upward) in the msA and msP sectors at 1500 m depth shown in Fig. 10c–d. In Exp 1b, a decrease in northward Ekman transport across 55° S causes a decrease in the Southern Ocean upwelling (Fig. 10b). In this experiment there is an increase in the upward flux above 2000 m depth in msA and a decrease in the downward flux below 1000 m depth in msP, fluxes that subsequently join the upper-ocean northward flow and the deep southward flow in the Atlantic and Pacific oceans, respectively. The insensitivity of North Atlantic AMOC intensity as well as of intermediate-depth Southern Hemisphere recirculation to increased westerly forcing has also been reported in other modeled experiments (Jochum and Eden, 2015; Rahmstorf and England, 1997).

These ocean interior circulation changes lead to a denser (lighter) water being upwelled in the Southern Ocean for Exp 1a and Exp 1b, respectively, leading to less (more) entrainment and consequently decreasing (increasing) amounts of AABW reaching the abyssal ocean for these experiments (Fig. 10f). More (less) upwelling together with this Southern Hemisphere recirculation enhances (reduces) ocean new production in the Southern Ocean, as more (fewer) nutrients are carried to the surface there (Fig. 10g). These changes in Southern Ocean NP are not reflected in surface ocean $\delta^{13}\text{C}$ values (Fig. 10h, as well as in msA and msP) in this zone of low model new-production efficiency. Rather, the decrease (increase) in $\delta^{13}\text{C}$ values in Exp 1a (Exp 1b) is associated with a lighter (heavier) signal of ^{13}C from more (less) upwelling of deeper water originating from northern latitudes

of Atlantic and Pacific model zones. Air–sea exchange of CO_2 with the Southern Ocean reflects changes in the upwelling rates there as more or less carbon-rich deeper water is carried to surface layers there. More (less) outgassing there leads to an increase (decrease) in atmospheric CO_2 concentration (Fig. 10i) and a resulting rise (fall) in atmospheric temperature (Fig. 10j). Such a Southern Hemisphere westerly wind intensity–atmospheric CO_2 relationship has also been reported in another modeled experiment (d’Orgeville et al., 2010). Changes in atmospheric CO_2 content are nearly uniform in all atmospheric boxes due to the rapid turnover time of the atmosphere. The temperature change in the southern polar atmospheric box is around 2.5 and -1.8° C for Exp 1a and Exp 1b, respectively. However, this warming (cooling) signal decreases rapidly farther northward such that mean Southern Hemisphere atmospheric temperature changes are around 0.7 and -0.5° C for Exp 1a and 1b, respectively. Finally, our Exp 1a results are in line with the importance of Southern Hemisphere westerly winds for deglacial atmospheric CO_2 rise as found in models and proxy-data reconstructions (Mayr et al., 2013; Menviel et al., 2018).

3.2.2 Antarctic ice sheet melt freshwater forcing

Forcing and model results for this experiment are shown in Fig. 11. The rapid freshwater pulse to the Southern Ocean shelf (Exp 2a) produces a greater and more abrupt decrease in AABW fluxes flowing down off the shelf break ($F_{sl,0}$), as well as in the abyssal ocean, F_{sl} (Fig. 11b). For Exp 2a, $F_{sl,0}$ and F_{sl} reach minimum values of 3.5 and 11 Sv, respectively, i.e., around 30 % less than the pre-industrial values. In Exp 2b, modest declines of 0.7 and 2 Sv are obtained for $F_{sl,0}$ and F_{sl} , representing a decrease of only 13 % compared to modern-day values (Gordon, 2019). Such an effect on AABW production rates due to Antarctic meltwater on the Southern Ocean shelf has been observed in similar Antarctic-meltwater experiments using more complex models (Fogwill et al., 2015; Silvano et al., 2018; Li et al., 2023). Consequently, the abyssal counterclockwise circulation decreases its intensity by more than 11 and 2 Sv for fast and slow freshwater pulses, respectively, as shown by the northward streamline evolution at 4500 m depth crossing 55° S (Fig. 11c). Such behavior has been reported for numerous model experiments including a multi-model ensemble of CMIP6 model experiments (Park and Latif, 2019; Mackie et al., 2020; Chen et al., 2023). This corresponds to a 75 % decrease compared to only a 14 % decrease for the fast and slow freshwater pulses, respectively, underlining the sensitivity of model AABW circulation to not only the size but also the speed of the Antarctic ice sheet meltwater pulse. Such lower AABW ventilation rates lead to the decline in dissolved O_2 content of the abyssal northern sectors of the Pacific and Atlantic oceans (Fig. 11d–e). This suggests aging of the abyssal ocean, also reported in Li et al. (2023). A greater AMOC penetration depth, as a consequence of weak-

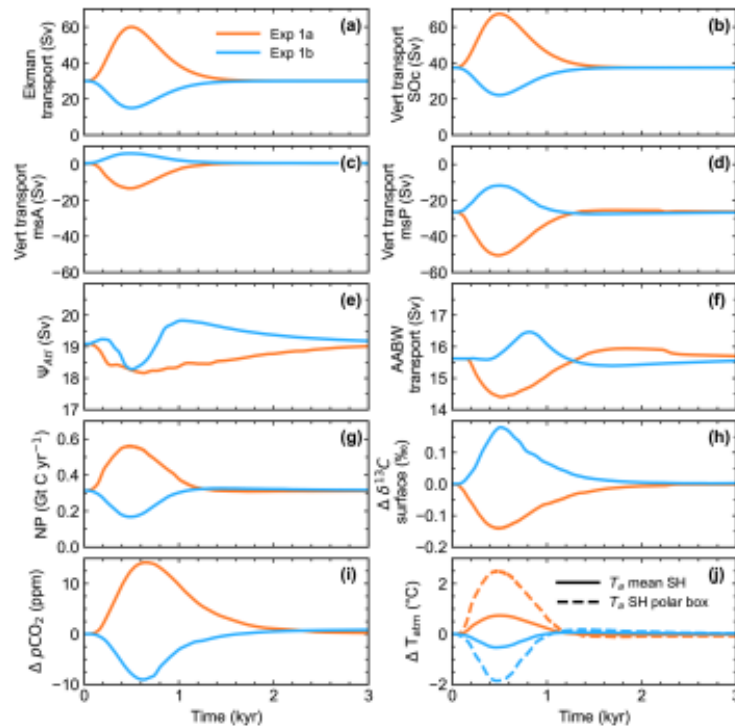


Figure 10. Results for 3000-year simulations for two different choices of northward Ekman transport across 55°S. (a) Applied Ekman transport evolutions; (b–d) vertical transport (Vert transport, defined as positive upward) at 1500 m depth for the Southern Ocean, msA and msP sectors, respectively; (e) northward transport across 55°N above 1000 m depth in the Atlantic Ocean; (f) AABW transport reaching the abyssal Southern Ocean; (g–h) Southern Ocean new-production evolution and Southern Ocean surface $\delta^{13}\text{C}$ change; and (i–j) changes in atmospheric CO_2 and atmospheric temperature (solid lines denote Southern Hemisphere mean T_a , and dashed lines denote T_a for the atmospheric southern polar zone, 55–90°S).

ened AABW abyssal circulation, may inhibit a further decrease in the abyssal O_2 content of the North Atlantic Ocean as more atmospheric oxygen is carried to those depths.

Opposite behaviors are observed in the abyssal ocean $\Delta^{14}\text{C}$ content for the northernmost model sectors of the North Atlantic and North Pacific oceans (hnA and hnP, respectively). The increase in the hnA sector (Fig. 11f) is caused by deeper AMOC penetration depth as the AABW cell gets weaker, leading to increased transport of near-surface ^{14}C to the abyssal ocean. In the hnP sector, the decrease in ^{14}C content stems from longer residence times due to the reduced AABW ventilation there, leading to more radioactive decay. The ^{18}O signature in the abyssal ocean is quite sensitive to the freshwater forcing to the Southern Ocean shelf as meltwater from the Antarctica ice sheet comes with an isotopic signal of -40‰ in the model. This is shown in Fig. 11h–i, where similar changes are observed in the sectors directly north of the Southern Ocean (msA

and msP) at 4500 m depth, with changes of around -0.17‰ and -0.09‰ for fast and slow forcing experiments, respectively. This demonstrates the model’s ability to capture the $\delta^{18}\text{O}_w$ signal from Antarctic ice sheet melting, shown to be a better indicator of such melting than ocean salinity changes (Kim and Timmermann, 2024). Despite all these ocean interior changes, Exp 2a and Exp 2b forcings lead only to small changes in atmospheric CO_2 of around 1 ppm or less in both experiments. As a consequence, there is nearly no change in the global atmospheric temperature although small sea-ice-dynamics-driven oscillations of a 20-year period are found in the southern polar atmospheric temperature (not shown). We stress that this simplified experiment was carried out mainly to test the model performance under isolated freshwater forcing. A comprehensive study of the global climate system response to Antarctic ice sheet melting would also require consideration of the climatic effects leading to the melting in the

first place, i.e., a coupling of the climate system and the ice sheet.

4 Discussion and conclusions

We have described and tested a new Earth system model of intermediate complexity, DCESS II, which has been calibrated to the pre-industrial Earth system. For this relatively simple model, efforts were made to limit the number of model free parameters and to constrain their values as much as possible using observations. At the end of this process, despite model limitations, we generally find excellent agreement with available modern observations. When compared with results from the DCESS I model, a number of improvements in our new model stand out, as described below.

Some key features of the physical part of the model, like the horizontal resolution, a simplified dynamical scheme for large-scale ocean circulation, stratification-dependent vertical diffusion, a gravity current approach to the formation of Antarctic Bottom Water and a dynamical formulation for sea ice, have helped us to achieve good agreement with observed data like atmospheric heat and water vapor transport and ocean temperature and salinity distributions (Lauvset et al., 2022) with a space and time resolution not possible using the original DCESS I model. These improvements, together with updates in ocean biogeochemistry such as a light dependence on the surface new (exported) production of organic matter, dependence on the calcite saturation state for the biogenic carbonate production and local temperature dependence on organic matter remineralization, result in accurate model representations of ocean biogeochemical tracers, highlighted by excellent model–data agreement with regard to marine carbon cycle species, well beyond that achieved with the DCESS I model, in particular with respect to ^{13}C (Shaffer et al., 2008). Furthermore, the incorporation of a new land biosphere module with three different vegetation types and a light–atmospheric CO_2 dependence on net primary production on land, as well as ocean sediment and lithosphere modules applied to multiple ocean and land sectors, makes results of the new model much more amenable to comparison with data than is the case for the DCESS I model. All the above improvements help make the DCESS II model an excellent yet economical tool for studying and gaining short- as well as long-term understanding of the global carbon cycle.

Two experiments were conducted in order to explore and test model performance. In the first experiment (Exp 1) we forced the model in a way that emulates the role of the Southern Hemisphere westerly winds in large-scale ocean circulation. In the second experiment (Exp 2) we introduced (at two different rates) a freshwater melt volume equivalent to a global sea level rise of 5 m onto the shelf surrounding Antarctica. In both experiments, model results show important physical and biogeochemical changes in the ocean driv-

ing perturbations in the global carbon cycle. This is reflected in responses of atmospheric CO_2 as well as of abyssal ocean $\Delta^{14}\text{C}$ and dissolved O_2 content. These experiments serve to demonstrate how the model captures the global role that Southern Hemisphere westerly winds and Antarctic Bottom Water play in the Earth system. Our Exp 1 supports the role of the Southern Hemisphere westerly winds in modulating past glacial–interglacial atmospheric carbon dioxide variations, while our Exp 2 points toward the impact that future Antarctic ice sheet melting would have on the formation of Antarctic Bottom Water and on the deep global ocean in general.

The development and calibration of the DCESS II model as described here have also set the stage for future work. For example, coupling of the model to an Antarctic ice sheet (AIS) model will provide a more realistic Earth system simulation when compared to our idealized experiment 2 described above. For this work an extended and improved version of the simple, well-tested DAIS model (Shaffer, 2014) will be used. In another example, planned incorporation of methane, nitrogen and sulfur cycles into the next DCESS II update will significantly improve its ability to deal realistically with deep-time global warming events associated with massive carbon inputs to the Earth system. Under such conditions, suboxic/anoxic ocean conditions may arise, leading, for example, to denitrification and sulfate reduction that must be addressed in such an update. Groundwork for this step has already been done in as much as these global biogeochemical cycles and suboxic/anoxic processes have been incorporated into the DCESS I model (Shaffer et al., 2017). In addition, other potential model applications include the study of different global climatic events like Dansgaard–Oeschger oscillations or longer climatic events like the Eocene–Oligocene transition or even the assessment of deep-time mass extinction events by taking advantage of the relative simplicity of the model for setting proper boundary conditions like orbital forcing and continental distribution. In this regard, when such deep-time model applications with quite different boundary conditions from today are to be made, careful consideration should be made in choosing the few (only two) regional tunings of the model.

In conclusion, we have presented, validated and tested a simple and fast new Earth system model of intermediate complexity intended to be a flexible, comprehensive and economical Earth system modeling platform. Despite its limitations like relatively low horizontal resolution and multiple parameterizations, the model represents most Earth system components quite well, especially the global-scale carbon cycle. Due to its simplicity, it could be easily modified in terms of boundary conditions to address specific past epochs. Thus, we find DCESS II to be a useful tool for studies of past, present and future global change on timescales of years to millions of years while not needing substantial computational resources.

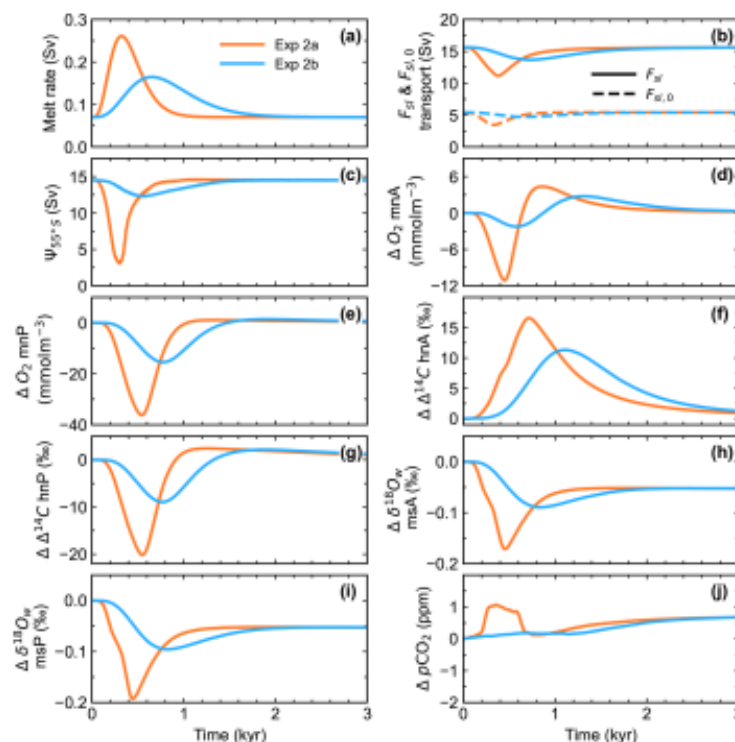


Figure 11. Results for 3000-year simulations for two different choices of Antarctic ice sheet melt rate. (a) Applied melt rates evolutions, (b) AABW transport flowing off the Southern Ocean shelf ($F_{SI,0}$) and reaching abyssal depths (F_{SI}), (c) total northward transport (combined Atlantic and Pacific) crossing 55° S below 4500 m depth, (d–e) changes in dissolved O_2 content in the ocean at 4500 m depth for northern sectors of the Atlantic and the Pacific Ocean, respectively (mNA and mNP), (f–g) ocean $\Delta^{14}C$ change at 4500 m depth for the northernmost sectors of the Atlantic and the Pacific Ocean, respectively (55–65° N, hnA and hnP), (h–i) $\delta^{18}O_w$ change at 4500 m depth for ocean sectors directly north of the Southern Ocean (msA and msP) and (j) global mean atmospheric pCO_2 change.

Code availability. The code for the DCESS II model v1.0 is archived on Zenodo (<https://doi.org/10.5281/zenodo.13738105>, Fernández Villanueva, 2024) as well as at <https://www.dcess.dk/> (last access: 20 June 2024).

Data availability. The observed ocean data used in Figs. 4–6 and in Fig. 8 are from the Global Ocean Data Analysis Project version 2.2022 (GLODAPv2.2022; Lauvset et al., 2022) database and can be accessed at the National Oceanic and Atmospheric Administration (NOAA) National Centers for Environmental Information (NCEI) under <https://doi.org/10.25921/114w-0t92>. Observed values of seawater ^{18}O shown in Fig. 4 are from the Global Seawater Oxygen-18 Database – v1.22 and can be accessed at <https://data.giss.nasa.gov/o18data/> (Schmidt, 1999; Bigg and Rohling, 2000). Sea ice observations are from the Sea Ice Index, Version 3, of the National Snow and Ice Data Center, Boulder, Colorado, USA (Fetterer et al., 2017), and can be accessed at <https://doi.org/10.7265/N5K072F8>. The World Ocean At-

las database (Boyer et al., 2018) used for calculation of the reference temperature for organic matter remineralization can be accessed at NOAA NCEI under <https://www.ncei.noaa.gov/archive/accession/NCEI-WOA18> (last access: 23 August 2023). Southern Hemisphere atmospheric CO_2 data were obtained from the Cape Grim Baseline Air Pollution Station belonging to the Commonwealth Scientific and Industrial Research Organisation (CSIRO) Oceans and Atmosphere and the Australian Bureau of Meteorology. These data can be freely downloaded at https://capegrim.csiro.au/GreenhouseGas/data/CapeGrim_CO2_data_download.csv (CSIRO and Bureau of Meteorology, 2023). Northern Hemisphere atmospheric CO_2 data were obtained from the Mauna Loa Observatory belonging to the NOAA Earth System Research Laboratories (ESRL). These data can be freely downloaded at <https://gml.noaa.gov/ccgg/trends/> (NOAA and GML, 2021). Present-day volcano distributions were obtained from the Volcano Locations Database belonging to NOAA NCEI. These data can be freely downloaded from <https://www.ngdc.noaa.gov/hazel/view/hazards/volcano/loc-data> (last access: 17 November 2023). Reference wind values for air–sea exchange are

from the NOAA/CIRES/DOE 20th Century Reanalysis (V3) dataset provided by NOAA PSL, Boulder, Colorado, USA, at https://www.psl.noaa.gov/data/gridded/data.20thC_ReanV3.html (NOAA, 2022).

Author contributions. EF and GS designed the work. EF led the development of the new model and code, to which GS contributed. EF wrote the original draft and, together with GS, discussed model concepts and results and wrote the final article.

Competing interests. The contact author has declared that neither of the authors has any competing interests.

Disclaimer. Publisher's note: Copernicus Publications remains neutral with regard to jurisdictional claims made in the text, published maps, institutional affiliations, or any other geographical representation in this paper. While Copernicus Publications makes every effort to include appropriate place names, the final responsibility lies with the authors.

Acknowledgements. We thank Yasuto Watanabe and the anonymous reviewer as well as the editor for their very constructive comments that helped us improve the article. We are indebted to the Chilean Agencia Nacional de Investigación y Desarrollo (ANID) for financial support of this work, which was largely supported through the ANID/CONICYT-PFCHA/Doctorado Nacional/2017-21171747 and FONDECYT 1190230 grants but also through FONDECYT grant 1230534 and the ANID Millennium Science Initiative Program (Millennium Institute of Oceanography AIM23-0003). In addition, we thank Roberto Rondanelli of the University of Chile, who helped us with cross-equatorial heat transport parameterization. Finally, we would like to extend special thanks to Donald Canfield, who invited Esteban Fernández Villanueva to spend time at his lab at the University of Southern Denmark and whose valuable comments and discussions helped us with the formulation of the ocean biogeochemistry module.

Financial support. This research has been supported by the Chilean Agencia Nacional de Investigación y Desarrollo (grant nos. ANID/CONICYT-PFCHA/Doctorado Nacional/2017-21171747, FONDECYT 1190230, FONDECYT 1230534 and the ANID Millennium Science Initiative Program (Millennium Institute of Oceanography AIM23-0003)).

Review statement. This paper was edited by Olivier Marti and reviewed by Yasuto Watanabe and one anonymous referee.

References

- Aagaard, K., Coachman, L. K., and Carmack, E.: On the halocline of the Arctic Ocean, *Deep-Sea Res. Pt. 1*, 28, 529–545, [https://doi.org/10.1016/0198-0149\(81\)90115-1](https://doi.org/10.1016/0198-0149(81)90115-1), 1981.
- Amante, C. and Eakins, B. W.: ETOPO1 1 Arc-Minute Global Relief Model: Procedures, Data Sources and Analysis, NOAA Technical Memorandum NESDIS NGDC-24, National Geophysical Data Center, NOAA, <https://www.ncsl.noaa.gov/products/etopo-global-relief-model> (last access: 30 May 2019), 2009.
- Antoine, D. and Morel, A.: Modelling the seasonal course of the upper ocean pCO₂ (I). Development of a one-dimensional model, *Tellus B*, 47, 103–121, <https://doi.org/10.1034/j.1600-0889.47.issue1.11.x>, 1995.
- Archer, D. E.: An atlas of the distribution of calcium carbonate in sediments of the deep sea, *Global Biogeochem. Cy.*, 10, 159–174, <https://doi.org/10.1029/95GB03016>, 1996.
- Archer, D. E., Morford, J. L., and Emerson, S. R.: A model of suboxic sedimentary diagenesis suitable for automatic tuning and gridded global domains, *Global Biogeochem. Cy.*, 16, 17-1–17-21, <https://doi.org/10.1029/2000GB001288>, 2002.
- Baines, P. G.: Mixing regimes for the flow of dense fluid down slopes into stratified environments, *J. Fluid Mech.*, 538, 245–267, <https://doi.org/10.1017/S0022112005005434>, 2005.
- Baines, P. G.: Mixing in Downslope Flows in the Ocean - Plumes versus Gravity Currents, *Atmos-Ocean*, 46, 405–419, <https://doi.org/10.3137/ao.460402>, 2008.
- Bendtsen, J.: Climate sensitivity to changes in solar insolation in a simple coupled climate model, *Clim. Dynam.*, 18, 595–609, <https://doi.org/10.1007/s00382-001-0198-4>, 2002.
- Bendtsen, J., Hilligsoe, K. M., Hansen, J. L. S., and Richardson, K.: Analysis of remineralisation, lability, temperature sensitivity and structural composition of organic matter from the upper ocean, *Prog. Oceanogr.*, 130, 125–145, <https://doi.org/10.1016/j.pocean.2014.10.009>, 2015.
- Berelson, W. M., Balch, W. M., Najjar, R., Feely, R. A., Sabine, C., and Lee, K.: Relating estimates of CaCO₃ production, export, and dissolution in the water column to measurements of CaCO₃ rain into sediment traps and dissolution on the sea floor: A revised global carbonate budget, *Global Biogeochem. Cy.*, 21, GB1024, <https://doi.org/10.1029/2006gb002803>, 2007.
- Berger, A. and Loutre, M. F.: Insolation values for the climate of the last 10 million years, *Quaternary Sci. Rev.*, 10, 297–317, [https://doi.org/10.1016/0277-3791\(91\)90033-Q](https://doi.org/10.1016/0277-3791(91)90033-Q), 1991.
- Berner, R. A.: Burial of organic carbon and pyrite sulfur in the modern ocean; its geochemical and environmental significance, *Am. J. Sci.*, 282, 451–473, <https://doi.org/10.2475/ajs.282.4.451>, 1982.
- Berner, R. A.: A model for atmospheric CO₂ over Phanerozoic time, *Am. J. Sci.*, 291, 339–376, <https://doi.org/10.2475/ajs.291.4.339>, 1991.
- Berner, R. A.: Chemical weathering and its effect on atmospheric CO₂ and climate, in: *Chemical Weathering Rates of Silicate Minerals*, edited by: White, A. F. and Brantley, S. L., De Gruyter, Berlin, Boston, 565–584, <https://doi.org/10.1515/9781501509650-015>, 1995.
- Berner, R. A.: GEOCARBSULF: A combined model for Phanerozoic atmospheric O₂ and CO₂, *Geochim. Cosmochim. Ac.*, 70, 5653–5664, <https://doi.org/10.1016/j.gca.2005.11.032>, 2006.

- Bigg, G. R. and Rohling, E. J.: An oxygen isotope data set for marine water, *J. Geophys. Res.*, 105, 8527–8535, <https://doi.org/10.1029/2000JC900005>, 2000.
- Bonan, G. B.: Forests and Climate Change: Forcings, Feedbacks, and the Climate Benefits of Forests, *Science*, 320, 1444–1449, <https://doi.org/10.1126/science.1155121>, 2008.
- Boyer, T. P., García, H. E., Locarnini, R. A., Zweng, M. M., Mishonov, A. V., Reagan, J. R., Weathers, K. A., Baranova, O. K., Paver, C. R., Seidov, D., and Smolyar, I. V.: World Ocean Atlas 2018, NOAA National Centers for Environmental Information [data set], <https://www.ncei.noaa.gov/archive/accession/NCEI-WOA18> (last access: 23 August 2023), 2018.
- Budyko, M. I.: Effect of Solar Radiation Variations on Climate of Earth, *Tellus*, 21, 611–619, <https://doi.org/10.3402/tellusa.v21i5.10109>, 1969.
- Byrne, B. and Goldblatt, C.: Radiative forcing at high concentrations of well-mixed greenhouse gases, *Geophys. Res. Lett.*, 41, 152–160, <https://doi.org/10.1002/2013gl058456>, 2014.
- Cartapanis, O., Galbraith, E. D., Bianchi, D., and Jaccard, S. L.: Carbon burial in deep-sea sediment and implications for oceanic inventories of carbon and alkalinity over the last glacial cycle, *Clim. Past*, 14, 1819–1850, <https://doi.org/10.5194/cp-14-1819-2018>, 2018.
- Chapin III, S. F., Matson, P. A., and Vitousek, P.: Principles of terrestrial ecosystem ecology, Springer, New York, NY, USA, <https://doi.org/10.1007/978-1-4419-9504-9>, 2011.
- Chen, J. J., Swart, N. C., Beadling, R., Cheng, X., Hattermann, T., Jüling, A., Li, Q., Marshall, J., Martin, T., Muilwijk, M., Pauling, A. G., Purich, A., Smith, I. J., and Thomas, M.: Reduced deep convection and bottom water formation due to Antarctic meltwater in a multi-model ensemble, *Geophys. Res. Lett.*, 50, e2023GL106492, <https://doi.org/10.1029/2023gl106492>, 2023.
- CSIRO and Bureau of Meteorology (Australia): Cape Grim Greenhouse Gas Data, CSIRO and Bureau of Meteorology [data set], https://capegrim.csiro.au/GreenhouseGas/data/CapeGrim_CO2_data_download.csv, last access: 29 September 2023.
- Dai, A. and Trenberth, K. E.: Estimates of Freshwater Discharge from Continents: Latitudinal and Seasonal Variations, *J. Hydrometeorol.*, 3, 660–687, [https://doi.org/10.1175/1525-7541\(2002\)003<0660:EOFDFC>2.0.CO;2](https://doi.org/10.1175/1525-7541(2002)003<0660:EOFDFC>2.0.CO;2), 2002.
- Danabasoglu, G., Large, W. G., and Briegleb, B. P.: Climate impacts of parameterized Nordic Sea overflows, *J. Geophys. Res.*, 115, C11005, <https://doi.org/10.1029/2010JC006243>, 2010.
- DeConto, R. M. and Pollard, D.: Contribution of Antarctica to past and future sea-level rise, *Nature*, 531, 591–597, <https://doi.org/10.1038/nature17145>, 2016.
- Dey, D. and Döös, K.: Atmospheric Freshwater Transport From the Atlantic to the Pacific Ocean: A Lagrangian Analysis, *Geophys. Res. Lett.*, 47, e2019GL086176, <https://doi.org/10.1029/2019GL086176>, 2020.
- d’Orgeville, M., Sijp, W. P., England, M. H., and Meissner, K. J.: On the control of glacial-interglacial atmospheric CO₂ variations by the Southern Hemisphere westerlies, *Geophys. Res. Lett.*, 37, L21703, <https://doi.org/10.1029/2010gl045261>, 2010.
- Drever, J. I.: The effect of land plants on weathering rates of silicate minerals, *Geochim. Cosmochim. Ac.*, 58, 2325–2332, [https://doi.org/10.1016/0016-7037\(94\)90013-2](https://doi.org/10.1016/0016-7037(94)90013-2), 1994.
- Dunne, J. P., Sarmiento, J. L., and Gnanadesikan, A.: A synthesis of global particle export from the surface ocean and cycling through the ocean interior and on the seafloor, *Global Biogeochem. Cy.*, 21, GB4006, <https://doi.org/10.1029/2006gb002907>, 2007.
- Eby, M., Weaver, A. J., Alexander, K., Zickfeld, K., Abe-Ouchi, A., Cimadoribus, A. A., Cressin, E., Drijfhout, S. S., Edwards, N. R., Eliseev, A. V., Feulner, G., Fichefet, T., Forest, C. E., Goosse, H., Holden, P. B., Joos, F., Kawamiya, M., Kicklighter, D., Kienert, H., Matsumoto, K., Mokhov, I. I., Monier, E., Olsen, S. M., Pedersen, J. O. P., Perrette, M., Philippon-Berthier, G., Ridgwell, A., Schlosser, A., Schneider von Deimling, T., Shaffer, G., Smith, R. S., Spahni, R., Sokolov, A. P., Steinacher, M., Tachiiri, K., Tokos, K., Yoshimori, M., Zeng, N., and Zhao, F.: Historical and idealized climate model experiments: an intercomparison of Earth system models of intermediate complexity, *Clim. Past*, 9, 1111–1140, <https://doi.org/10.5194/cp-9-1111-2013>, 2013.
- Eichinger, R., Shaffer, G., Albarrán, N., Rojas, M., and Lambert, F.: An improved land biosphere module for use in the DCESS Earth system model (version 1.1) with application to the last glacial termination, *Geosci. Model Dev.*, 10, 3481–3498, <https://doi.org/10.5194/gmd-10-3481-2017>, 2017.
- England, M. H.: Representing the Global-Scale Water Masses in Ocean General Circulation Models, *J. Phys. Oceanogr.*, 23, 1523–1552, [https://doi.org/10.1175/1520-0485\(1993\)023<1523:RTGSWM>2.0.CO;2](https://doi.org/10.1175/1520-0485(1993)023<1523:RTGSWM>2.0.CO;2), 1993.
- Fernández Villanueva, E.: DCESS II model v1.0, Zenodo [code], <https://doi.org/10.5281/zenodo.13738105>, 2024.
- Fetterer, F., Knowles, K., Meier, W. N., Savoie, M., and Windnagel, A. K.: Sea Ice Index, Version 3, National Snow and Ice Data Center, Boulder, Colorado USA [data set], <https://doi.org/10.7265/N5K072F8>, 2017.
- Filippelli, G. M.: The Global Phosphorus Cycle, *Rev. Miner. Geochem.*, 48, 391–425, <https://doi.org/10.2138/rmg.2002.48.10>, 2002.
- Fogwill, C. J., Phipps, S. J., Turney, C. S. M., and Golledge, N. R.: Sensitivity of the Southern Ocean to enhanced regional Antarctic ice sheet meltwater input, *Earth’s Future*, 3, 317–329, <https://doi.org/10.1002/2015ef000306>, 2015.
- Gaillardet, J., Dupré, B., Louvat, P., and Allègre, C. J.: Global silicate weathering and CO₂ consumption rates deduced from the chemistry of large rivers, *Chem. Geol.*, 159, 3–30, [https://doi.org/10.1016/S0009-2541\(99\)00031-5](https://doi.org/10.1016/S0009-2541(99)00031-5), 1999.
- Gangstø, R., Joos, F., and Gehlen, M.: Sensitivity of pelagic calcification to ocean acidification, *Biogeosciences*, 8, 433–458, <https://doi.org/10.5194/bg-8-433-2011>, 2011.
- Gargett, A. E. and Holloway, G.: Dissipation and diffusion by internal wave breaking, *J. Mar. Res.*, 42, 15–27, 1984.
- Gerber, S., Joos, F., and Prentice, I. C.: Sensitivity of a dynamic global vegetation model to climate and atmospheric CO₂, *Glob. Change Biol.*, 10, 1223–1239, <https://doi.org/10.1111/j.1529-8817.2003.00807.x>, 2004.
- Gordon, A. L.: Bottom Water Formation, in: Encyclopedia of Ocean Sciences, 3rd Edn., edited by: Cochran, J. K., Bokuniewicz, H. J., and Yager, P. L., Academic Press, Oxford, 120–126, <https://doi.org/10.1016/B978-0-12-409548-9.04019-7>, 2019.
- Gray, W. R., De Lavergne, C., Jnglin Wills, R. C., Menviel, L., Spence, P., Holzer, M., Kageyama, M., and Michel, E.: Poleward Shift in the Southern Hemisphere Westerly Winds Synchronous With the Deglacial Rise in CO₂, *Paleoceanogr. Paleoclim.*, 38, e2023PA004666, <https://doi.org/10.1029/2023pa004666>, 2023.

- Gröger, M. and Mikolajewicz, U.: Note on the CO₂ air-sea gas exchange at high temperatures, *Ocean Model.*, 39, 284–290, <https://doi.org/10.1016/j.ocemod.2011.05.003>, 2011.
- Haney, R. L.: Surface Thermal Boundary Condition for Ocean Circulation Models, *J. Phys. Oceanogr.*, 1, 241–248, [https://doi.org/10.1175/1520-0485\(1971\)001<0241:Stbcfo>2.0.Co;2](https://doi.org/10.1175/1520-0485(1971)001<0241:Stbcfo>2.0.Co;2), 1971.
- Harper, D. T., Hönisch, B., Zeebe, R. E., Shaffer, G., Haynes, L. L., Thomas, E., and Zachos, J. C.: The Magnitude of Surface Ocean Acidification and Carbon Release During Eocene Thermal Maximum 2 (ETM-2) and the Paleocene-Eocene Thermal Maximum (PETM), *Paleoceanogr. Paleoclim.*, 35, e2019PA003699, <https://doi.org/10.1029/2019pa003699>, 2020.
- Hartmann, D. L.: *Global Physical Climatology*, 2nd Edn., Elsevier Press, Amsterdam, Netherlands, <https://doi.org/10.1016/C2009-0-00030-0>, 2016.
- Hartmann, J., Jansen, N., Dürr, H. H., Kempe, S., and Köhler, P.: Global CO₂-consumption by chemical weathering: What is the contribution of highly active weathering regions?, *Global Planet. Change*, 69, 185–194, <https://doi.org/10.1016/j.gloplacha.2009.07.007>, 2009.
- Haumann, F. A., Gruber, N., Münnich, M., Frenger, I., and Kern, S.: Sea-ice transport driving Southern Ocean salinity and its recent trends, *Nature*, 537, 89–92, <https://doi.org/10.1038/nature19101>, 2016.
- Hayes, C. T., Costa, K. M., Anderson, R. F., Calvo, E., Chase, Z., Demina, L. L., Dutay, J. C., German, C. R., Heimbürgen-Bouvida, L. E., Jaccard, S. L., Jacobel, A., Köhfeld, K. E., Kravchishina, M. D., Lippold, J., Mekik, F., Missiaen, L., Pavia, F. J., Paytan, A., Pedrosa-Pamies, R., Petrova, M. V., Rahman, S., Robinson, L. F., Roy-Barman, M., Sanchez-Vidal, A., Shiller, A., Tagliabue, A., Tessin, A. C., Van Hulten, M., and Zhang, J.: Global ocean sediment composition and burial flux in the deep sea, *Global Biogeochem. Cy.*, 35, e2020GB006769, <https://doi.org/10.1029/2020gb006769>, 2021.
- Hazarika, M. K., Yasuoka, Y., Ito, A., and Dye, D.: Estimation of net primary productivity by integrating remote sensing data with an ecosystem model, *Remote Sens. Environ.*, 94, 298–310, <https://doi.org/10.1016/j.rse.2004.10.004>, 2005.
- Hedges, J. I. and Keil, R. G.: Sedimentary organic matter preservation: an assessment and speculative synthesis, *Mar. Chem.*, 49, 81–115, [https://doi.org/10.1016/0304-4203\(95\)00008-F](https://doi.org/10.1016/0304-4203(95)00008-F), 1995.
- Heuzé, C.: Antarctic Bottom Water and North Atlantic Deep Water in CMIP6 models, *Ocean Sci.*, 17, 59–90, <https://doi.org/10.5194/os-17-59-2021>, 2021.
- Heywood, K. J., Schmidtko, S., Heuzé, C., Kaiser, J., Jickells, T. D., Queste, B. Y., Stevens, D. P., Wadley, M., Thompson, A. F., Fielding, S., Guihen, D., Creed, E., Ridley, J. K., and Smith, W.: Ocean processes at the Antarctic continental slope, *Philos. T. R. Soc. A*, 372, 20130047, <https://doi.org/10.1098/rsta.2013.0047>, 2014.
- Hirschi, J. J. M., Barnier, B., Böning, C., Biastoch, A., Blaker, A. T., Coward, A., Danilov, S., Drijfhout, S., Getzlaff, K., Griffies, S. M., Hasumi, H., Hewitt, H., Iovino, D., Kawasaki, T., Kiss, A. E., Koldunov, N., Marzocchi, A., Mecking, J. V., Moat, B., Molines, J. M., Myers, P. G., Penduff, T., Roberts, M., Treguier, A. M., Sein, D. V., Sidorenko, D., Small, J., Spence, P., Thompson, L., Weijer, W., and Xu, X.: The Atlantic Meridional Overturning Circulation in High-Resolution Models, *J. Geophys. Res.-Oceans*, 125, e2019JC015522, <https://doi.org/10.1029/2019jc015522>, 2020.
- IOC, SCOR, IAPSO: The international thermodynamic equation of seawater – 2010: Calculation and use of thermodynamic properties, Intergovernmental Oceanographic Commission, Manuals and Guides No. 56, UNESCO, 196 pp., <https://doi.org/10.25607/OBP-1338>, 2010.
- Jochum, M. and Eden, C.: The Connection between Southern Ocean Winds, the Atlantic Meridional Overturning Circulation, and Indo-Pacific Upwelling, *J. Climate*, 28, 9250–9257, <https://doi.org/10.1175/jcli-d-15-0263.1>, 2015.
- Johnson, G. C.: Quantifying Antarctic Bottom Water and North Atlantic Deep Water volumes, *J. Geophys. Res.*, 113, C05027, <https://doi.org/10.1029/2007jc004477>, 2008.
- IPCC: *Climate Change 2021: The Physical Science Basis. Contribution of Working Group I to the Sixth Assessment Report of the Intergovernmental Panel on Climate Change*, edited by: Masson-Delmotte, V., Zhai, P., Pirani, A., Connors, S. L., Péan, C., Berger, S., Caud, N., Chen, Y., Goldfarb, L., Gomis, M. L., Huang, M., Leitzell, K., Lonnoy, E., Matthews, J. B. R., Maycock, T. K., Waterfield, T., Yelekçi, O., Yu, R., and Zhou, B., Cambridge University Press, Cambridge, United Kingdom and New York, NY, USA, <https://doi.org/10.1017/9781009157896>, 2021.
- Joos, F., Roth, R., Fuglestedt, J. S., Peters, G. P., Enting, I. G., von Bloh, W., Brovkin, V., Burke, E. J., Eby, M., Edwards, N. R., Friedrich, T., Frölicher, T. L., Halloran, P. R., Holden, P. B., Jones, C., Kleinen, T., Mackenzie, F. T., Matsumoto, K., Meinshausen, M., Plattner, G.-K., Reisinger, A., Segsneider, J., Shaffer, G., Steinacher, M., Strassmann, K., Tanaka, K., Timmermann, A., and Weaver, A. J.: Carbon dioxide and climate impulse response functions for the computation of greenhouse gas metrics: a multi-model analysis, *Atmos. Chem. Phys.*, 13, 2793–2825, <https://doi.org/10.5194/acp-13-2793-2013>, 2013.
- Keeling, R. F., Stephens, B. B., Najjar, R. G., Doney, S. C., Archer, D., and Heimann, M.: Seasonal variations in the atmospheric O₂/N₂ ratio in relation to the kinetics of air-sea gas exchange, *Global Biogeochem. Cy.*, 12, 141–163, <https://doi.org/10.1029/97gb02339>, 1998.
- Kim, H. and Timmermann, A.: Seawater oxygen isotopes as a tool for monitoring future meltwater from the Antarctic ice-sheet, *Commun. Earth Environ.*, 5, 343, <https://doi.org/10.1038/s43247-024-01514-4>, 2024.
- Komar, N. and Zeebe, R. E.: Reconciling atmospheric CO₂, weathering, and calcite compensation depth across the Cenozoic, *Sci. Adv.*, 7, eabd4876, <https://doi.org/10.1126/sciadv.abd4876>, 2021.
- Krissansen-Totton, J. and Catling, D. C.: Constraining climate sensitivity and continental versus seafloor weathering using an inverse geological carbon cycle model, *Nat. Commun.*, 8, 15423, <https://doi.org/10.1038/ncomms15423>, 2017.
- Kunze, E.: Internal-Wave-Driven Mixing: Global Geography and Budgets, *J. Phys. Oceanogr.*, 47, 1325–1345, <https://doi.org/10.1175/jpo-d-16-0141.1>, 2017.
- Laufkötter, C., John, J. G., Stock, C. A., and Dunne, J. P.: Temperature and oxygen dependence of the remineralization of organic matter, *Global Biogeochem. Cy.*, 31, 1038–1050, <https://doi.org/10.1002/2017gb005643>, 2017.

- Lauvset, S. K., Lange, N., Tanhua, T., Bittig, H. C., Olsen, A., Kozyr, A., Alin, S. R., Álvarez, M., Azetsu-Scott, K., Barbero, L., Becker, S., Brown, P. J., Carter, B. R., Cotrim da Cunha, L., Feely, R. A., Hoppema, M., Humphreys, M. P., Ishii, M., Jeansson, E., Jiang, L. Q., Jones, S. D., Lo Monaco, C., Murata, A., Müller, J. D., Pérez, F. F., Pfeil, B., Schirnick, C., Steinfeldt, R., Suzuki, T., Tilbrook, B., Ulfso, A., Velo, A., Woosley, R. J., and Key, R. M.: Global Ocean Data Analysis Project version 2.2022 (GLODAPv2.2022), NOAA National Centers for Environmental Information [data set], <https://doi.org/10.25921/1f4w-0t92>, 2022.
- Lee, S. Y., Chiang, J. C. H., Matsumoto, K., and Tokos, K. S.: Southern Ocean wind response to North Atlantic cooling and the rise in atmospheric CO₂: Modeling perspective and paleoceanographic implications, *Paleoceanography*, 26, PA1214, <https://doi.org/10.1029/2010pa002004>, 2011.
- Lenton, T. M., Daines, S. J., and Mills, B. J. W.: COPSE reloaded: An improved model of biogeochemical cycling over Phanerozoic time, *Earth-Sci. Rev.*, 178, 1–28, <https://doi.org/10.1016/j.earscirev.2017.12.004>, 2018.
- Li, M., Peng, C., Wang, M., Xue, W., Zhang, K., Wang, K., Shi, G., and Zhu, Q.: The carbon flux of global rivers: A re-evaluation of amount and spatial patterns, *Ecol. Indic.*, 80, 40–51, <https://doi.org/10.1016/j.ecolind.2017.04.049>, 2017.
- Li, Q., England, M. H., Hogg, A. M., Rintoul, S. R., and Morrison, A. K.: Abyssal ocean overturning slowdown and warming driven by Antarctic meltwater, *Nature*, 615, 841–847, <https://doi.org/10.1038/s41586-023-05762-w>, 2023.
- Lohmann, G. and Lorenz, S.: On the hydrological cycle under paleoclimatic conditions as derived from AGCM simulations, *J. Geophys. Res.*, 105, 17417–17436, <https://doi.org/10.1029/2000JD900189>, 2000.
- Ludwig, W., Amiotte-Suchet, P., and Probst, J.-L.: Enhanced chemical weathering of rocks during the last glacial maximum: a sink for atmospheric CO₂?, *Chem. Geol.*, 159, 147–161, [https://doi.org/10.1016/S0009-2541\(99\)00038-8](https://doi.org/10.1016/S0009-2541(99)00038-8), 1999.
- MacDougall, A. H., Frölicher, T. L., Jones, C. D., Rogelj, J., Matthews, H. D., Zickfeld, K., Arora, V. K., Barrett, N. J., Brovkin, V., Burger, F. A., Eby, M., Eliseev, A. V., Hajima, T., Holden, P. B., Jeltsch-Thömmes, A., Koven, C., Mengis, N., Menviel, L., Michou, M., Mokhov, I. I., Oka, A., Schwinger, J., Séférian, R., Shaffer, G., Sokolov, A., Tachiiri, K., Tjiputra, J., Wiltshire, A., and Ziehn, T.: Is there warming in the pipeline? A multi-model analysis of the Zero Emissions Commitment from CO₂, *Biogeosciences*, 17, 2987–3016, <https://doi.org/10.5194/bg-17-2987-2020>, 2020.
- Mackie, S., Smith, I. J., Ridley, J. K., Stevens, D. P., and Langhorne, P. J.: Climate response to increasing Antarctic iceberg and ice shelf melt, *J. Climate*, 33, 8917–8938, <https://doi.org/10.1175/jcli-d-19-0881.1>, 2020.
- Maier-Reimer, E.: Geochemical cycles in an ocean general circulation model. Preindustrial tracer distributions, *Global Biogeochem. Cy.*, 7, 645–677, <https://doi.org/10.1029/93gb01355>, 1993.
- Marchal, O., Stocker, T. F., and Joos, F.: A latitude-depth, circulation-biogeochemical ocean model for paleoclimate studies. Development and sensitivities, *Tellus B*, 50, 290–316, <https://doi.org/10.3402/tellush.v50i3.16130>, 1998.
- Marsay, C. M., Sanders, R. J., Henson, S. A., Pabortsava, K., Achterberg, E. P., and Lampitt, R. S.: Attenuation of sinking particulate organic carbon flux through the mesopelagic ocean, *P. Natl. Acad. Sci. USA*, 112, 1089–1094, <https://doi.org/10.1073/pnas.1415311112>, 2015.
- Martin, J. H., Knauer, G. A., Karl, D. M., and Broenkow, W. W.: VERTEX: carbon cycling in the northeast Pacific, *Deep-Sea Res. Pt. I*, 34, 267–285, [https://doi.org/10.1016/0198-0149\(87\)90086-0](https://doi.org/10.1016/0198-0149(87)90086-0), 1987.
- Masson-Delmotte, V., Hou, S., Ekaykin, A., Jouzel, J., Aristarain, A., Bernardo, R. T., Bromwich, D., Cattani, O., Delmotte, M., Falourd, S., Frezzotti, M., Gallée, H., Genoni, L., Isaksen, E., Landais, A., Helsen, M. M., Hoffmann, G., Lopez, J., Morgan, V., Motoyama, H., Noone, D., Oerter, H., Petit, J. R., Royer, A., Uemura, R., Schmidt, G. A., Schlosser, E., Simões, J. C., Steig, E. J., Stenni, B., Stievenard, M., Van Den Broeke, M. R., Van De Wal, R. S. W., Van De Berg, W. J., Vimeux, F., and White, J. W. C.: A Review of Antarctic Surface Snow Isotopic Composition: Observations, Atmospheric Circulation, and Isotopic Modeling, *J. Climate*, 21, 3359–3387, <https://doi.org/10.1175/2007jcli2139.1>, 2008.
- Mayr, C., Lücke, A., Wagner, S., Wissel, H., Ohlendorf, C., Habertzell, T., Oehlerich, M., Schäbitz, F., Wille, M., Zhu, J., and Zolitschka, B.: Intensified Southern Hemisphere westerlies regulated atmospheric CO₂ during the last deglaciation, *Geology*, 41, 831–834, <https://doi.org/10.1130/G34335.1>, 2013.
- Meehl, G. A., Senior, C. A., Eyring, V., Flato, G., Lamarque, J.-F., Stouffer, R. J., Taylor, K. E., and Schlund, M.: Context for interpreting equilibrium climate sensitivity and transient climate response from the CMIP6 Earth system models, *Sci. Adv.*, 6, eaba1981, <https://doi.org/10.1126/sciadv.aba1981>, 2020.
- Menviel, L., Spence, P., Yu, J., Chamberlain, M. A., Matear, R. J., Meissner, K. J., and England, M. H.: Southern Hemisphere westerlies as a driver of the early deglacial atmospheric CO₂ rise, *Nat. Commun.*, 9, 2503, <https://doi.org/10.1038/s41467-018-04876-4>, 2018.
- Milliman, J. and Droessler, A.: Calcium carbonate sedimentation in the global ocean: Linkages between the neritic and pelagic environments, *Oceanography*, 8, 92–94, <https://doi.org/10.5670/oceanog.1995.04>, 1995.
- Milliman, J. D.: Production and accumulation of calcium carbonate in the ocean: Budget of a nonsteady state, *Global Biogeochem. Cy.*, 7, 927–957, <https://doi.org/10.1029/93GB02524>, 1993.
- Mucci, A.: The solubility of calcite and aragonite in seawater at various salinities, temperatures, and one atmosphere total pressure, *Am. J. Sci.*, 283, 780–799, <https://doi.org/10.2475/ajs.283.7.780>, 1983.
- Munhoven, G.: Glacial–interglacial changes of continental weathering: estimates of the related CO₂ and HCO₃⁻ flux variations and their uncertainties, *Global Planet. Change*, 33, 155–176, [https://doi.org/10.1016/S0921-8181\(02\)00068-1](https://doi.org/10.1016/S0921-8181(02)00068-1), 2002.
- Munhoven, G.: Glacial–interglacial rain ratio changes: Implications for atmospheric CO₂ and ocean–sediment interaction, *Deep-Sea Res. Pt. II*, 54, 722–746, <https://doi.org/10.1016/j.dsr2.2007.01.008>, 2007.
- Mutshinda, C., Finkel, Z., Widdicombe, C., and Irwin, A.: Phytoplankton traits from long-term oceanographic time-series, *Mar. Ecol. Prog. Ser.*, 576, 11–25, <https://doi.org/10.3354/meps12220>, 2017.

- National Oceanic and Atmospheric Administration (NOAA) and Global Monitoring Laboratory (GML): Mauna Loa CO₂ monthly mean data, NOAA and GML [data set], <https://gml.noaa.gov/ccgg/trends/>, last access: 28 January 2021.
- NOAA: NOAA-CIRES-DOE Twentieth Century Reanalysis Project version 3, NOAA PSL [data set], Boulder, Colorado, USA, https://www.psl.noaa.gov/data/gridded/data.20thC_ReanV3.html, last access: 18 November 2022.
- Olsen, S. M., Shaffer, G., and Bjerrum, C. J.: Ocean oxygen isotope constraints on mechanisms for millennial-scale climate variability, *Paleoceanogr. Paleoclim.*, 20, PA1014, <https://doi.org/10.1029/2004PA001063>, 2005.
- Oort, A. H. and Peixoto, J. P.: Global Angular-Momentum and Energy-Balance Requirements from Observations, *Adv. Geophys.*, 25, 355–490, [https://doi.org/10.1016/S0065-2687\(08\)60177-6](https://doi.org/10.1016/S0065-2687(08)60177-6), 1983.
- Orsi, A. H.: Recycling bottom waters, *Nat. Geosci.*, 3, 307–309, <https://doi.org/10.1038/ngeo854>, 2010.
- Orsi, A. H., Johnson, G. C., and Bullister, J. L.: Circulation, mixing, and production of Antarctic Bottom Water, *Prog. Oceanogr.*, 43, 55–109, [https://doi.org/10.1016/S0079-6611\(99\)00004-X](https://doi.org/10.1016/S0079-6611(99)00004-X), 1999.
- Orsi, A. H., Jacobs, S. S., Gordon, A. L., and Visbeck, M.: Cooling and ventilating the Abyssal Ocean, *Geophys. Res. Lett.*, 28, 2923–2926, <https://doi.org/10.1029/2001gl012830>, 2001.
- Orsi, A. H., Smethie, W. M. J., and Bullister, J. L.: On the total input of Antarctic waters to the deep ocean: A preliminary estimate from chlorofluorocarbon measurements, *J. Geophys. Res.*, 107, 31–1–31–14, <https://doi.org/10.1029/2001JC000976>, 2002.
- Pagani, M., Arthur, M. A., and Freeman, K. H.: Miocene evolution of atmospheric carbon dioxide, *Paleoceanography*, 14, 273–292, <https://doi.org/10.1029/1999pa900006>, 1999.
- Park, W. and Latif, M.: Ensemble global warming simulations with idealized Antarctic meltwater input, *Clim. Dynam.*, 52, 3223–3239, <https://doi.org/10.1007/s00382-018-4319-8>, 2019.
- Paytan, A. and McLaughlin, K.: The oceanic phosphorus cycle, *Chem. Rev.*, 107, 563–576, <https://doi.org/10.1021/cr0503613>, 2007.
- Planchat, A., Kwiatkowski, L., Bopp, L., Torres, O., Christian, J. R., Butenschön, M., Lovato, T., Séférian, R., Chamberlain, M. A., Aumont, O., Watanabe, M., Yamamoto, A., Yool, A., Ilyina, T., Tsujino, H., Krumhardt, K. M., Schwinger, J., Tjiputra, J., Dunne, J. P., and Stock, C.: The representation of alkalinity and the carbonate pump from CMIP5 to CMIP6 Earth system models and implications for the carbon cycle, *Biogeosciences*, 20, 1195–1257, <https://doi.org/10.5194/bg-20-1195-2023>, 2023.
- Purkey, S. G. and Johnson, G. C.: Antarctic Bottom Water Warming and Freshening: Contributions to Sea Level Rise, Ocean Freshwater Budgets, and Global Heat Gain, *J. Climate*, 26, 6105–6122, <https://doi.org/10.1175/JCLI-D-12-00834.1>, 2013.
- Rahmstorf, S. and England, M. H.: Influence of Southern Hemisphere Winds on North Atlantic Deep Water Flow, *J. Phys. Oceanogr.*, 27, 2040–2054, [https://doi.org/10.1175/1520-0485\(1997\)027<2040:IOSHWO>2.0.CO;2](https://doi.org/10.1175/1520-0485(1997)027<2040:IOSHWO>2.0.CO;2), 1997.
- Regaudie-de-Gioux, A. and Duarte, C. M.: Temperature dependence of planktonic metabolism in the ocean, *Global Biogeochem. Cy.*, 26, GB1015, <https://doi.org/10.1029/2010gb003907>, 2012.
- Rodriguez, J. M., Johns, T. C., Thorpe, R. B., and Wiltshire, A.: Using moisture conservation to evaluate oceanic surface freshwater fluxes in climate models, *Clim. Dynam.*, 37, 205–219, <https://doi.org/10.1007/s00382-010-0899-7>, 2011.
- Roquet, F., Madec, G., McDougall, T. J., and Barker, P. M.: Accurate polynomial expressions for the density and specific volume of seawater using the TEOS-10 standard, *Ocean Model.*, 90, 29–43, <https://doi.org/10.1016/j.ocemod.2015.04.002>, 2015.
- Ruckert, K. L., Shaffer, G., Pollard, D., Guan, Y., Wong, T. E., Forest, C. E., and Keller, K.: Assessing the Impact of Retreat Mechanisms in a Simple Antarctic Ice Sheet Model Using Bayesian Calibration, *PLOS ONE*, 12, e0170052, <https://doi.org/10.1371/journal.pone.0170052>, 2017.
- Sarmiento, J. L. and Gruber, N.: *Ocean Biogeochemical Dynamics*, Princeton University Press, Princeton, New Jersey, USA, <https://doi.org/10.2307/j.ctt3fgxqx>, 2006.
- Schmidt, G. A.: Forward modeling of carbonate proxy data from planktonic foraminifera using oxygen isotope tracers in a global ocean model, *Paleoceanography*, 14, 482–497, <https://doi.org/10.1029/1999PA900025>, 1999.
- Shaffer, G.: Long-term effectiveness and consequences of carbon dioxide sequestration, *Nat. Geosci.*, 3, 464–467, <https://doi.org/10.1038/ngeo896>, 2010.
- Shaffer, G.: Formulation, calibration and validation of the DAIS model (version 1), a simple Antarctic ice sheet model sensitive to variations of sea level and ocean subsurface temperature, *Geosci. Model Dev.*, 7, 1803–1818, <https://doi.org/10.5194/gmd-7-1803-2014>, 2014.
- Shaffer, G. and Lambert, F.: In and out of glacial extremes by way of dust—climate feedbacks, *P. Natl. Acad. Sci. USA*, 115, 2026–2031, <https://doi.org/10.1073/pnas.1708174115>, 2018.
- Shaffer, G. and Olsen, S. M.: Sensitivity of the thermohaline circulation and climate to ocean exchanges in a simple coupled model, *Clim. Dynam.*, 17, 433–444, <https://doi.org/10.1007/pl00013739>, 2001.
- Shaffer, G., Bendtsen, J., and Ulloa, O.: Fractionation during remineralization of organic matter in the ocean, *Deep-Sea Res. Pt. I*, 46, 185–204, [https://doi.org/10.1016/S0967-0637\(98\)00061-2](https://doi.org/10.1016/S0967-0637(98)00061-2), 1999.
- Shaffer, G., Malskaer Olsen, S., and Pepke Pedersen, J. O.: Presentation, calibration and validation of the low-order, DCESS Earth System Model (Version 1), *Geosci. Model Dev.*, 1, 17–51, <https://doi.org/10.5194/gmd-1-17-2008>, 2008.
- Shaffer, G., Olsen, S. M., and Pedersen, J. O. P.: Long-term ocean oxygen depletion in response to carbon dioxide emissions from fossil fuels, *Nat. Geosci.*, 2, 105–109, <https://doi.org/10.1038/ngeo420>, 2009.
- Shaffer, G., Huber, M., Rondanelli, R., and Pepke Pedersen, J. O.: Deep time evidence for climate sensitivity increase with warming, *Geophys. Res. Lett.*, 43, 6538–6545, <https://doi.org/10.1002/2016gl069243>, 2016.
- Shaffer, G., Fernández Villanueva, E., Rondanelli, R., Pedersen, J. O. P., Olsen, S. M., and Huber, M.: Implementation of methane cycling for deep-time global warming simulations with the DCESS Earth system model (version 1.2), *Geosci. Model Dev.*, 10, 4081–4103, <https://doi.org/10.5194/gmd-10-4081-2017>, 2017.
- Siegel, D. A., Buesseler, K. O., Doney, S. C., Salliey, S. F., Behrenfeld, M. J., and Boyd, P. W.: Global assessment of ocean carbon export by combining satellite observations and

- food-web models, *Global Biogeochem. Cy.*, 28, 181–196, <https://doi.org/10.1002/2013gb004743>, 2014.
- Siegenthaler, U. and Oeschger, H.: Biospheric CO₂ emissions during the past 200 years reconstructed by deconvolution of ice core data, *Tellus B*, 39B, 140–154, <https://doi.org/10.1111/j.1600-0889.1987.tb00278.x>, 1987.
- Silvano, A., Rintoul, S. R., Peña-Molino, B., Hobbs, W. R., van Wijk, E., Aoki, S., Tamura, T., and Williams, G. D.: Freshening by glacial meltwater enhances melting of ice shelves and reduces formation of Antarctic Bottom Water, *Sci. Adv.*, 4, eaap9467, <https://doi.org/10.1126/sciadv.aap9467>, 2018.
- Stocker, T. F., Broecker, W. S., and Wright, D. G.: Carbon uptake experiments with a zonally-averaged global ocean circulation model, *Tellus B*, 46, 103–122, <https://doi.org/10.3402/tellusb.v46i2.15756>, 1994.
- Stone, P. H. and Miller, D. A.: Empirical relations between seasonal changes in meridional temperature gradients and meridional fluxes of heat, *J. Atmos. Sci.*, 37, 1708–1721, [https://doi.org/10.1175/1520-0469\(1980\)037<1708:ERBSC1>2.0.CO;2](https://doi.org/10.1175/1520-0469(1980)037<1708:ERBSC1>2.0.CO;2), 1980.
- Sulpis, O., Jeansson, E., Dinuier, A., Lauvset, S. K., and Middelburg, J. J.: Calcium carbonate dissolution patterns in the ocean, *Nat. Geosci.*, 14, 423–428, <https://doi.org/10.1038/s41561-021-00743-y>, 2021.
- Sverdrup, H. U., Johnson, M. W., and Fleming, R. H.: *The Oceans: Their physics, chemistry, and general biology*, Prentice Hall, Inc., New York, USA, 1942.
- Talley, L. D., Reid, J. L., and Robbins, P. E.: Data-based meridional overturning streamfunctions for the global ocean, *J. Climate*, 16, 3213–3226, [https://doi.org/10.1175/1520-0442\(2003\)016<3213:Dmostf>2.0.Co;2](https://doi.org/10.1175/1520-0442(2003)016<3213:Dmostf>2.0.Co;2), 2003.
- Toggweiler, J. R., Russell, J. L., and Carson, S. R.: Mid-latitude westerlies, atmospheric CO₂, and climate change during the ice ages, *Paleoceanography*, 21, PA2005, <https://doi.org/10.1029/2005pa001154>, 2006.
- Trenberth, K. E. and Caron, J. M.: Estimates of Meridional Atmosphere and Ocean Heat Transports, *J. Climate*, 14, 3433–3443, [https://doi.org/10.1175/1520-0442\(2001\)014<3433:eomaao>2.0.co;2](https://doi.org/10.1175/1520-0442(2001)014<3433:eomaao>2.0.co;2), 2001.
- Wang, X. L., Stone, P. H., and Marotzke, J.: Global thermohaline circulation. Part II: Sensitivity with interactive atmospheric transports, *J. Climate*, 12, 83–91, [https://doi.org/10.1175/1520-0442\(1999\)012<0083:GTCPIP>2.0.CO;2](https://doi.org/10.1175/1520-0442(1999)012<0083:GTCPIP>2.0.CO;2), 1999.
- Wanninkhof, R.: Relationship between wind speed and gas exchange over the ocean, *J. Geophys. Res.*, 97, 7373–7382, <https://doi.org/10.1029/92JC00188>, 1992.
- Weiss, R. F.: The solubility of nitrogen, oxygen and argon in water and seawater, *Deep-Sea Res. Ocean. Abstr.*, 17, 721–735, [https://doi.org/10.1016/0011-7471\(70\)90037-9](https://doi.org/10.1016/0011-7471(70)90037-9), 1970.
- Weiss, R. F.: Carbon dioxide in water and seawater: the solubility of a non-ideal gas, *Mar. Chem.*, 2, 203–215, [https://doi.org/10.1016/0304-4203\(74\)90015-2](https://doi.org/10.1016/0304-4203(74)90015-2), 1974.
- Willeit, M., Ilyina, T., Liu, B., Heinze, C., Perrette, M., Heineemann, M., Dalmonech, D., Brovkin, V., Munhoven, G., Börker, J., Hartmann, J., Romero-Mujalli, G., and Ganopolski, A.: The Earth system model CLIMBER-X v1.0 – Part 2: The global carbon cycle, *Geosci. Model Dev.*, 16, 3501–3534, <https://doi.org/10.5194/gmd-16-3501-2023>, 2023.
- Xu, X. B., Chang, Y. S., Peters, H., Ozgokmen, T. M., and Chassignet, E. P.: Parameterization of gravity current entrainment for ocean circulation models using a high-order 3D nonhydrostatic spectral element model, *Ocean Model.*, 14, 19–44, <https://doi.org/10.1016/j.ocemod.2006.02.006>, 2006.
- Yamanaka, Y. and Tajika, E.: The role of the vertical fluxes of particulate organic matter and calcite in the oceanic carbon cycle: Studies using an ocean biogeochemical general circulation model, *Global Biogeochem. Cy.*, 10, 361–382, <https://doi.org/10.1029/96gb00634>, 1996.
- Zhang, J., Quay, P. D., and Wilbur, D. O.: Carbon isotope fractionation during gas-water exchange and dissolution of CO₂, *Geochim. Cosmochim. Ac.*, 59, 107–114, [https://doi.org/10.1016/0016-7037\(95\)91550-D](https://doi.org/10.1016/0016-7037(95)91550-D), 1995.
- Zelinka, M. D., Myers, T. A., McCoy, D. T., Po-Chedley, S., Caldwell, P. M., Ceppi, P., Klein, S. A., and Taylor, K. E.: Causes of higher climate sensitivity in CMIP6 models, *Geophys. Res. Lett.*, 47, e2019GL085782, <https://doi.org/10.1029/2019gl085782>, 2020.
- Zickfeld, K., Eby, M., Weaver, A. J., Alexander, K., Cressin, E., Edwards, N. R., Eliseev, A. V., Feulner, G., Fichefet, T., Forest, C. E., Friedlingstein, P., Goosse, H., Holden, P. B., Joos, F., Kawamiya, M., Kicklighter, D., Kienert, H., Matsumoto, K., Mokhov, I. I., Monier, E., Olsen, S. M., Pedersen, J. O. P., Perrette, M., Philippon-Berthier, G., Ridgwell, A., Schlosser, A., Schneider Von Deimling, T., Shaffer, G., Sokolov, A., Spahni, R., Steinacher, M., Tachiiri, K., Tokos, K. S., Yoshimori, M., Zeng, N., and Zhao, F.: Long-Term Climate Change Commitment and Reversibility: An EMIC Intercomparison, *J. Climate*, 26, 5782–5809, <https://doi.org/10.1175/jcli-d-12-00584.1>, 2013.
- Zondervan, J. R., Hilton, R. G., Dellinger, M., Clubb, F. J., Roylands, T., and Ogrič, M.: Rock organic carbon oxidation CO₂ release offsets silicate weathering sink, *Nature*, 623, 329–333, <https://doi.org/10.1038/s41586-023-06581-9>, 2023.

4.2. Chapter 2: “Role of mid- and high-latitude, Southern Hemisphere processes for ushering in the Middle Pleistocene Transition”. Submitted to *Paleoceanography and Paleoclimatology*.

Abstract

Glacial-interglacial cycles increased in length from about 41 to 100 thousand years during the Middle Pleistocene Transition (MPT) about 1.5 to 0.8 million years ago. This took place in step with strong global cooling after several million years of weaker cooling. Such strong MPT cooling likely set the stage for longer ice age cycles by, for example, facilitating Northern Hemisphere ice sheet growth. Here we use simulations with a newly-developed Earth System model of Intermediate Complexity together with sea surface temperature reconstructions to evaluate possible causes of the MPT cooling. In particular, we concentrate on the effects of changes in 1. Southern West Wind strength and position, 2. Sea ice and iceberg export from the Antarctic shelf, 3. Dust fertilization of the Southern Ocean and 4. Northern Hemisphere ice sheet extent. We find that weakened, equatorward-shifted Southern West Winds in combination with increased sea ice and iceberg export from the Antarctic Shelf can explain much of the strong MPT cooling. Our simulations suggest that these changes caused the cooling by decreasing heat and carbon exchange between the upper and deep Southern Ocean and increasing deep recirculation in the ocean, leading to deep ocean isolation and carbon storage together with atmospheric CO₂ drawdown. Dust-driven iron fertilization further enhanced this storage and drawdown while Northern Hemisphere ice sheet growth contributed mainly to regional cooling while promoting land biomass reduction that releases CO₂ to the atmosphere.

Role of mid- and high-latitude, Southern Hemisphere processes for ushering in the Middle Pleistocene Transition

G. Shaffer¹, E. Fernández Villanueva² and C. Karas³

¹Niels Bohr Institute, University of Copenhagen, 2100 Copenhagen Ø, Denmark

²Graduate Program in Oceanography, Department of Oceanography, Faculty of Natural Sciences and Oceanography, University of Concepción, P.O. Box 160-C, Concepción, Chile

³ Universidad de Santiago de Chile, Av. Bernardo O'Higgins 3363, Santiago, Chile

Corresponding author: Gary Shaffer (gs@nbi.ku.dk)

Key Points:

- Changes in Southern West Winds and Antarctic shelf sea ice and iceberg export explain much of the strong cooling across the MPT.
- Strong, MPT deep recirculation from entrainment into AABW on the Antarctic slope forms a deep, isolated, carbon-rich ocean water mass.
- Increased Southern Ocean dust fertilization draws down atmospheric CO₂ but also helps decrease total ocean new production across the MPT.

Abstract

Glacial-interglacial cycles increased in length from about 41 to 100 thousand years during the Middle Pleistocene Transition (MPT) about 1.5 to 0.8 million years ago. This took place in step with strong global cooling after several million years of weaker cooling. Such strong MPT cooling likely set the stage for longer ice age cycles by, for example, facilitating Northern Hemisphere ice sheet growth. Here we use simulations with a newly-developed Earth System model of Intermediate Complexity together with sea surface temperature reconstructions to evaluate possible causes of the MPT cooling. In particular, we concentrate on the effects of changes in 1. Southern West Wind strength and position, 2. Sea ice and iceberg export from the Antarctic shelf, 3. Dust fertilization of the Southern Ocean and 4. Northern Hemisphere ice sheet extent. We find that weakened, equatorward-shifted Southern West Winds in combination with increased sea ice and iceberg export from the Antarctic Shelf can explain much of the strong MPT cooling. Our simulations suggest that these changes caused the cooling by decreasing heat and carbon exchange between the upper and deep Southern Ocean and increasing deep recirculation in the ocean, leading to deep ocean isolation and carbon storage together with atmospheric CO₂ drawdown. Dust-driven iron fertilization further enhanced this storage and drawdown while Northern Hemisphere ice sheet growth contributed mainly to regional cooling while promoting land biomass reduction that releases CO₂ to the atmosphere.

1. Introduction

The Middle Pleistocene Transition (MPT), for present purposes considered to occur between 1.5 and 0.8 million years ago (Ma), was a period of transition from ~41 kyr glacial–interglacial cycles paced by obliquity to longer ~100 kyr cycles influenced by eccentricity-modulated, precessional pacing (Clark et al., 2006; Elderfield et al., 2012; Lisiecki & Raymo, 2005). Pre-MPT cycles were relatively symmetric and weak whereas post-MPT cycles were stronger and more asymmetric with longer glacials and shorter interglacials (Medina-Elizalde & Lea, 2005; von der Heydt et al., 2021). This shift occurred without major changes in orbital forcing characteristics, pointing toward explanations in terms of Earth system properties and feedbacks (An et al., 2024; Clark et al., 2006; Raymo et al., 2006; Ruddiman et al., 1986; Tziperman & Gildor, 2003; Willeit et al., 2019).

A major change across the MPT was the expansion of Northern Hemisphere (NH) ice sheets (Ao et al., 2023; Lisiecki & Raymo, 2005; Batchelor et al., 2009), which merged together, enabling ice sheet survival even during insolation maxima (Bintanja & van de Wal, 2008). Larger ice sheets promoted feedbacks like increased surface albedo and adiabatic cooling with increasing height, leading to further growth (Berends et al., 2021; Clark and Pollard, 1998). Furthermore, larger NH ice sheets become more susceptible to mechanisms favoring longer, asymmetrical ~100 kyr cycles like bedrock depression and calving (Abe-Ouchi et al., 2013, Clark and Pollard, 1998). A number of other mechanisms like regolith removal and ocean circulation change have been proposed for explaining glacial cycle evolution across the MPT (Behrends et al., 2021; Clark et al., 2006; Herbert, 2023).

The MPT was a period of strong global cooling, following more than two million years of weaker cooling (Lisiecki & Raymo, 2005, Westerhold et al., 2020). Whatever combination of processes are evoked to explain MPT ice age cycle lengthening, such strong MPT cooling likely preconditioned the system for such cycle lengthening by, for example, driving NH ice sheet expansion. Benthic $\delta^{18}\text{O}$ records have been used to infer changes in global ice volume and deep ocean temperature changes but this requires additional information to separate temperature and sea water contributions (Lisiecki & Raymo, 2005; Rohling et al., 2021). A more direct approach involves sea surface temperature (SST) reconstructions based on alkenones, foraminiferal Mg/Ca and faunal proxies from ocean sediment data (Fedorov et al., 2013; Fedorov et al., 2015; Snyder 2016).

Figure 1 presents global and regional mean SSTs from 4 Ma to the present from a recent application of this approach based on 127 published records (Clark et al., 2024) but here adjusted to present-day SSTs. For running means over 400 kyr, there is uniform, global mean SST cooling by 2.9°C from 4 to 1.5 Ma. Moderate cooling by 0.6°C is observed from 1.5 to 1.2 Ma, followed by strong cooling by 1.5°C from 1.2 to 0.8 Ma. Global mean SST remains rather uniform afterward (Figure 1a). However, significant trend differences between the hemispheres are observed (Figure 1 b-d): 1. From 4 to 2 Ma, strong mean Northern Hemisphere (NH) and extratropical NH cooling by 2.5 and 3.8°C, respectively, contrasted with weaker Southern Hemisphere (SH) and extratropical SH cooling then by 1.7 and 0.9°C, 2. From 2 to 0.8 Ma, strong mean SH and extratropical SH cooling by 3.2 and 4.0°C and 3. From 2 to 1.2 Ma,

moderate mean NH and extratropical NH cooling by 1.0 and 1.5°C, followed by intensified cooling there from 1.2 to 0.8 Ma by 0.9 and 1.3°C, respectively.

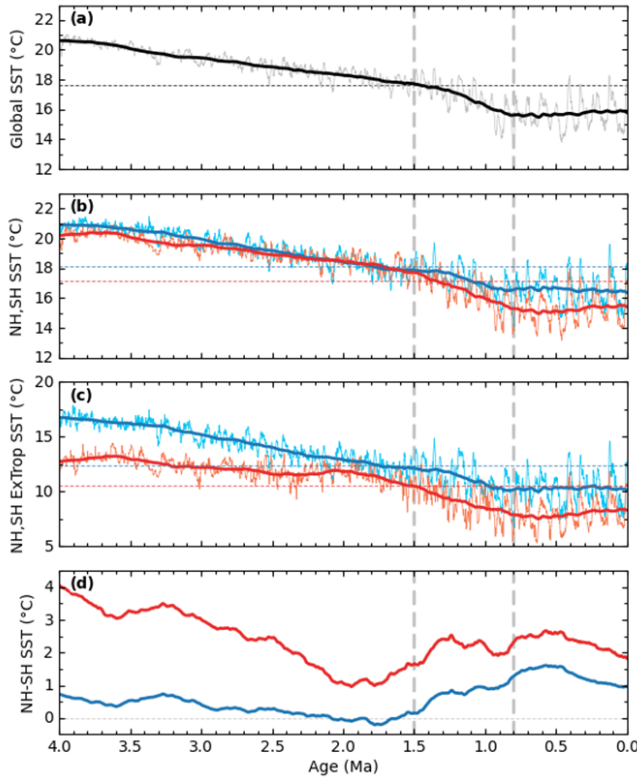


Figure 1. Sea surface temperature (SST) over the past 4 Myr. **A.** Global mean, **b.** Northern (blue) and Southern (red) hemisphere means, **c.** Extra-tropical, Northern (blue) and Southern (red) hemisphere means and **d.** Northern-Southern hemisphere (blue) and extra-tropical (red) differences. Data from Clark et al. (2024) adjusted to present-day SSTs of 17.62, 18.14, 17.12, 12.40 and 10.53°C, respectively. (horizontal dashed lines in **a.**, **b.** and **c.**). Data for this calculation is from

<https://www.ncei.noaa.gov/products/extended-reconstructed-sst-for-the-period-1940-to-1970>; extra-tropical data is from 35 – 55°. Thin lines are 1 kyr resolution results; thick lines are 400 kyr running means. Vertical dashed lines mark the MPT range used here (1.5 to 0.8 Ma).

This pattern indicates some global process to force the mean global cooling – likely reduced greenhouse gas forcing - combined with processes that redistribute heat between the hemispheres, like changes in Atlantic Meridional Overturning Circulation (AMOC) strength and/or processes leading to hemispheric cooling, such as albedo increases due to ice sheet and sea ice expansion. Strong, SH cooling from 2 Ma onward has been linked to Antarctic Ice Sheet growth and associated sea ice expansion (An et al., 2024). However, the temperature patterns shown in Figure 1b-d would also support an interpretation of AMOC weakening up to 2 Ma followed by strengthening up to 1.5 Ma as stronger/weaker AMOC leads to more/less SH to NH heat transfer.

In this study, we compare model simulations with proxy data across the MPT to explore forcing mechanisms for explaining the observed strong global and regional cooling during this time period. We also address the period of long, weaker global cooling before the MPT. In Section 2,

we describe our model and its application across the Pliocene-Pleistocene-MPT interval. We identify key forcings to be considered and choose their values for a standard case, MPT solution. In Section 3, we present standard case model results, compare model outputs with the SST reconstructions in Figure 1, and interpret modelled Earth system property evolutions before and during the MPT. We also analyse the relative importance of individual forcings and their interactions and discuss results of extensive sensitivity studies to varying forcing. Finally, Section 4 provides a summary and discussion of the findings.

2. Methods

2.1 DCESS II model

We use the new Danish Center for Earth System Science model (DCESS II), a simplified but comprehensive Earth System model of intermediate complexity containing atmosphere, land biosphere, ocean, ocean sediment and lithosphere modules (Fernández & Shaffer, 2025). DCESS II represents a substantial advancement over its predecessor, DCESS I (Shaffer et al., 2008), featuring significantly improved spatial and temporal resolution as well as expanded and improved representations of Earth system processes. The new model includes 6 atmosphere sectors spanning both hemispheres with sector limits at 55°S, 35°S, 0°, 35°N and 55°N and 12 ocean sectors encompassing Atlantic, Indo-Pacific (denoted Pacific below), Arctic and Southern Oceans with sector limits at 70°S, 55°S, 35°S, 0°, 35°N, 55°N and 65°N. It features prescribed northward Ekman transport across 55°S to mimic effects of the Southern West Winds, an improved sea ice formulation, a dynamic formulation for large-scale ocean overturning circulation and stratification-dependent vertical diffusivity. The land biosphere features three dynamically-varying vegetation types whereby net primary production depends on light and atmospheric CO₂. Ocean new production depends on light and nutrients and the remineralization rate for ocean organic matter is temperature-dependent.

Ocean sediment and the lithosphere formulations in DCESS II are adopted from DCESS I but are now applied to the multiple ocean and land regions. As in its predecessor, DCESS II maintains fine, 100 m vertical resolution in the ocean, but it now incorporates observed ocean topography for each ocean sector, with corresponding sediment segment areas also resolved at 100-meter intervals. Tracers of the atmospheric module are temperature, nitrous oxide, methane

($^{12,13}\text{C}$ isotopes), carbon dioxide ($^{12,13,14}\text{C}$ isotopes) and atmospheric oxygen. Tracers included in the ocean module are conservative temperature, absolute salinity, water ^{18}O , phosphate, dissolved inorganic carbon ($^{12,13,14}\text{C}$ isotopes), alkalinity and dissolved oxygen. A limitation factor for ocean new production is applied to the Arctic and the Southern Ocean (south of 35°S) to account for effects like dust fertilization. Biogenic calcite production in the ocean surface layer depends on new production, temperature and calcite saturation state. With these expanded formulations, improved spatial resolution, and modest computational demands, DCESS II is well-suited for simulating the evolution of the global climate–carbon cycle system over multimillion-year timescales.

Antarctic shelf processes and Antarctic Bottom Water (AABW) formation are features of special importance for this study. AABW originates mainly from dense Antarctic Shelf Water (ASW) that flows down the Antarctic slope entraining surrounding water as it descends into the deep ocean (Gordon, 2019; Orsi, et al., 2002). To address this, the model starts with a 500 m deep, Southern Ocean shelf between 69°S and 70°S (Heywood et al., 2014), maintained at freezing temperature by air-sea heat exchanges there. The salinity—and thus the density—of ASW is controlled by two key processes: (1) brine rejection during sea ice formation, which leaves behind salt-enriched water, and (2) freshwater input from iceberg calving off the Antarctic Ice Sheet and ice shelves (Nicholls et al., 2009; Portela et al., 2022; Silva et al., 2006; Tournadre et al., 2016). Both processes are prescribed in the model using observational data and reconstructions (Depoorter et al., 2013; Haumann et al., 2016; Rignot et al., 2013). When ASW becomes denser than adjacent Southern Ocean water, it flows downslope as a gravity current, entraining ambient water in certain depth ranges to become AABW. This process is addressed using a simple gravity current, entrainment formulation following Baines (2005, 2008), based on two coupled governing equations: one for downslope flow rate (F) and another for the height of the descending plume (H). These equations are numerically integrated downslope, given initial conditions at the 500 m depth shelf break, with the density difference between the plume and ambient water ($\Delta\rho$) updated at every time step. Entrainment occurs only when the Richardson number (Ri) - a measure of buoyancy divided by kinetic energy - is below 0.25, and increases as Ri values decrease. Ri is formulated as a function of H , $\Delta\rho$, and F and is proportional to the cosine of the slope angle. As a result, entrainment is centered on the steeper segments of the Antarctic slope, particularly between 1000 and 3000 m depth (Fig. S1). AABW

enters the deep Southern Ocean at a depth where its density matches that of the ambient water. Details can be found in (Fernández & Shaffer, 2025) where a pre-industrial calibration exhibited ASW and AABW values in agreement with observational estimates (Gordon, 2019; Orsi et al., 2002). It is worth noting that many, more complex models, including several in CMIP6, incorrectly simulate AABW formation through deep, open-ocean convection or omit downslope entrainment processes (Heuzé, 2021).

2.2. Pliocene-Pleistocene-MPT modelling approach

We use the DCESS II model to reproduce long term, global SST changes over the past 4 million years, characterized by uniform slow cooling up until about 1.5 Ma followed by more rapid cooling across the MPT until about 0.8 Ma (Figure 1a). The initial slow cooling phase is likely attributable to slowly decreasing greenhouse gas forcing and associated carbon-climate feedbacks. After some minor model modifications (Supporting Information), we start by deriving an initial condition for 4 Ma. We use estimated ocean calcium content and ocean carbon dissociation constants at that time (Zeebe & Tyrrell, 2019) and set atmospheric CO₂ concentration to be 400 ppm then (Bartoli et al., 2011; Köhler, 2023, LaRiviere et al., 2012; Sosdian et al., 2018). For this CO₂ level and pre-industrial (PI) CO₂ of 280 ppm, we find that our model climate sensitivity must be increased to 5°C per CO₂ doubling to achieve a observed mean global ocean SST ~3.0°C higher than its observed PI value (Figure 1a). Finally, for these conditions, we hold lithosphere outgassing at our model PI value (Fernández & Shaffer, 2024) and adjust model weathering of carbonate, silicate, old organic carbon and phosphate such as to achieve a 4 Ma, steady-state balance with model ocean sediment burial of calcium carbonate and organic matter. An alternative would have been to change lithosphere outgassing as in other, related work (Willeit et al., 2019) but we choose to focus on weathering, which is thought to control long-term cooling over the Pliocene-Pleistocene (Bayon et al., 2018; Chiang et al., 2024; Martin et al., 2023).

From this 4 Ma initial state, we tune parameters in our weathering formulation until our simulation reproduces the observed, uniform global mean SST decrease from 4 to 1.5 Ma (Figure 1a). Weathering is formulated as

$$W(t) = \text{fwth}(t) \times Q_{10}^{(T_a(t) - T_{a,\text{ref}})/10} \times W_0 \quad (1)$$

where W is the weathering rate, t is time in myr, W_0 is W at 4 Ma, $T_a(t)$ is the mean atmosphere temperature, $T_{a,\text{ref}}$ is T_a at 4 Ma, Q_{10} is the weathering increase for a 10°C increase in T_a , and $\text{fwth}(t)$ is a weatherability factor representing non-temperature-dependent weathering changes due to factors like mountain building. The same formulation was used in Fernández and Shaffer (2025) for the PI case with $Q_{10} = 2$ and $\text{fwth}(t) = 1$. After a number of simulations from our 4 Ma initial condition, using prescribed time evolution of ocean calcium content and ocean carbon dissociation constants (Zeebe & Tyrrell, 2019) and the incorporation of orbital forcing with values for eccentricity, obliquity, and longitude of perihelion from Berger and Loutre (1991), we found an excellent fit to observed, 4 to 1.5 Ma global mean SST cooling (Clark et al., 2024) using $Q_{10} = 1.5$ and $\text{fwth}(t) = 1 + 0.0687 \times t$.

We then extend the simulation across the MPT with this weathering formulation and orbital forcing, but now we also account for prescribed changes in four additional processes that likely contributed to the observed acceleration in global cooling: 1. Northward Ekman transport in the Southern Ocean, driven by shifts in the strength and latitudinal position of the Southern Westerly Winds (SWW) and affecting vertical exchange of heat, nutrient and carbon there; 2. Sea ice and iceberg export from the Antarctic shelf, which influences ASW (and, consequently, AABW formation) as well as Southern Ocean surface layers; 3. Dust fertilization of the Southern Ocean, enhancing marine productivity there and; 4. Equatorward extent of Northern Hemisphere ice sheets, affecting albedo and land biomass. Changes in these four forcings are prescribed to occur linearly in time over two intervals: from 1.5 to 1.2 Ma (accounting for 10% of the total MPT-era change) and from 1.2 to 0.8 Ma (90% of the total change). This two-step implementation reflects the structure of the observed SST transition (Figure 1a). For simplicity, these four forcings are held constant in the simulations at their PI values (Fernández & Shaffer, 2025) until 1.5 Ma and at their 0.8 Ma values from 0.8 Ma to the present. The post-0.8 Ma period is simulated for completeness only and will not be discussed further here.

Specific assumptions made regarding the MPT forcing are: 1. The pre-existing trend of the weatherability factor is continued across the MPT as the simplest assumption with no expected climate-related impact on it; 2. Influence of the SWWs is extended to include possible Ekman

transport across 35°S. Weakened, northward shifted SWWs would be expected across cooling intervals like the MPT (Toggweiler et al., 2006, PO, Anderson et al., 2009, Science, Vanugopal et al., 2023), 3. Increased sea ice production and export from the Antarctic shelf as well as increased Iceberg export/less Antarctic meltwater there in connection with MPT cooling (Shin & Liu, 2003, GRL; Starr et al., 2021). 4. Dust deposition and associated Southern Ocean fertilization are assumed to increase due to a drier climate and northward-shifted SWWs, exposing more continental dust sources (Shaffer & Lambert, 2018; Martinez-Garcia et al., 2011; Lamy et al., 2014), and 5. Northern Hemisphere ice sheets grew and expanded equatorward across the MPT as shown in geological reconstructions (Ao et al., 2023; Hodell & Channell, 2016). Table 1 lists the prescribed values and time evolution of the weatherability factor and the four additional forcings used in the standard Pliocene–Pleistocene–MPT simulation.

	4 to 1.5 Ma	1.2 Ma	0.8 to 0 Ma
Weatherability factor (<i>fwth</i>)	1 to 1.172	1.193	1.22
Northward Ekman transport at 55°S, 35°S (<i>Ekman</i>)	30 Sv, 0 Sv	28 Sv, 1 Sv	10 Sv, 10 Sv
Antarctic shelf sea ice export, Iceberg export (<i>Fice, fSO</i>)	0.13 Sv, 50%	0.143 Sv, 55%	0.26 Sv, 100%
Southern Ocean (35°S - 70°S) new production limitation factor (<i>LfSO</i>)	0.15	0.165	0.3
Latitude of Northern Hemisphere Ice sheet extent (<i>fgNH</i>)	70°N	68.85°N	58.5°N

Table 1. Applied forcings for the standard case simulation. The weatherability factor increases linearly from 4 to 0.8 Ma and is taken constant afterwards. For the remaining forcings, changes were applied linearly in time over two steps: 1.5 to 1.2 Ma and 1.2 to 0.8 Ma whereby 10% and 90% of the total 1.5 - 0.8 Ma changes were applied in the first and second step, respectively. Iceberg export percentage is defined to encompass the part of atmospheric water vapor transport southward across 69°S that is transported north of 69°S as icebergs. Abbreviations in italics are used in Figures 6 and 7. The Southern Ocean new production limitation factor emulates dust fertilization in the model.

3. Results

3.1. Standard case simulation

3.1.1. SST model-data comparison

Figure 2 presents results of our standard case simulation over the past 4 million years together with the SST reconstructions of Clark et al., 2024. There is a somewhat smaller decrease in

simulated global atmospheric temperature up to 1.5 Ma compared to the Clark et al., 2024 result (Figure 2a) that, however, is also model-dependent, based on model Ta - SST relationships. On the other hand, our model reproduces the observed slow, rather uniform global SST decrease over the 4 – 1.5 Ma range (Figure 1b) that has been our target for model calibration. The model underestimates NH cooling rates and overestimates SH cooling rates during the pre-MPT period (Figure 2c–f). This part of the simulation lacks sufficient interhemispheric redistribution discussed above to explain these observed hemispheric differences. However, from 1.5 to 0.8 Ma across the MPT, the model captures rather well the enhanced global SST cooling seen in the Clark et al., 2024 reconstruction. Furthermore, the magnitude of this simulated cooling greatly exceeds that produced by weathering forcing alone (indicated by the red lines in Figure 2). The simulation also reproduces key features of the observed MPT transition, including 1.1°C stronger SH SST cooling compared to NH SST cooling as well as amplified cooling in extratropical regions. We return to this modeled MPT structure in detail below, where we explore the mechanisms underlying these results.

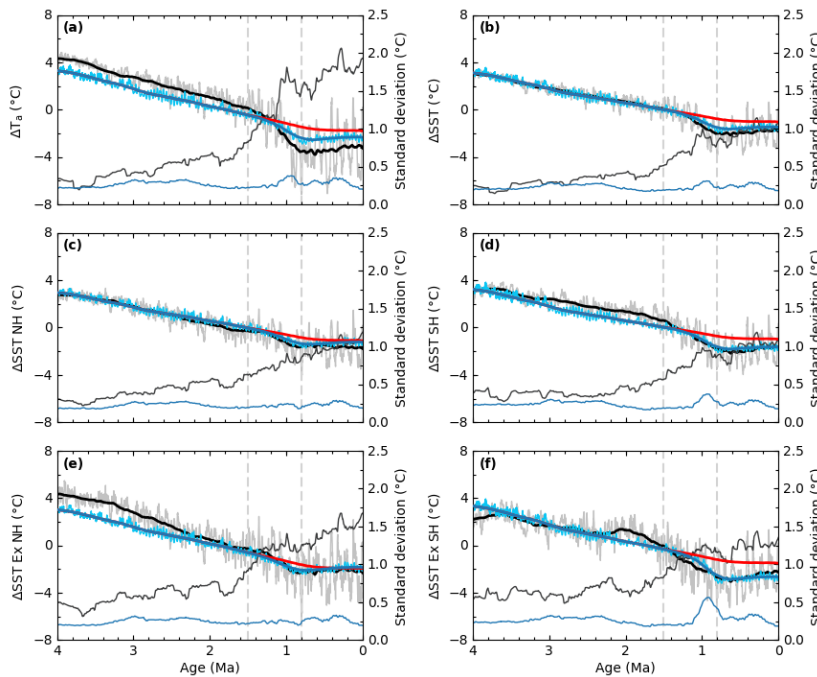


Figure 2. Comparisons of standard case model results with reconstructions of Clark et al. (2024) High-resolution (light thin lines) and 400 kyr running means (dark thick lines) for model results (blue) and reconstructions (black). Also shown are 400 kyr running means from 1.5 Ma onwards for changing weathering forcing only (thick red lines) **a.** Global mean temperature deviation from present day as well as SST deviations from present day for **b.** Global ocean, **c.** Northern Hemisphere (NH), **d.** Southern Hemisphere

(SH), **e.** Extra-tropical NH (ExNH) and **f.** Extra-tropical SH (ExSH). Model extra-tropical zones are the 35°- 55° model sectors. Also shown are standard deviations of high-resolution, model results (thin blue lines) and reconstructions (thin black lines). Vertical dashed lines mark the MPT range used here (1.5 to 0.8 Ma).

Figure 2 also shows the temporal evolution of standard deviations (SD) between high-resolution, standard case model results and the high-resolution, Clark et al. (2024) reconstructions (thin blue and black lines). Prior to 2 Ma, model SDs are comparable to observed SDs for global mean, NH, and SH SSTs (Fig 2b-d), although observed, extra-tropical SST variability is about twice model variability in this time range (Figure 2e,f). This suggests that, in the absence of large ice sheets, the model's response to orbital forcing broadly resembles the real-world climate response, albeit with less polar amplification. After 2 Ma, observed high-resolution variability increases steadily up to and across the MPT. This rise in variability reflects the progressive growth of ice sheets in both hemispheres and their interaction with the rest of the climate system. Our model lacks dynamic ice sheets and thus can not capture the post-2 Ma increase in observed variability.

3.1.2. Model pre-MPT property evolutions

Figure 3 provides a more comprehensive overview of our standard case, Pliocene-Pleistocene-MPT simulation. Weathering rates remain fairly constant leading up to the MPT (Figure 3a), reflecting an approximate balance between the effects of the applied increasing weatherability factor, as discussed in Section 2, and gradual global cooling (Equation 1). Weathering is ultimately responsible for an atmospheric CO₂ decline of 400 to 259 ppm from 4 to 1.5 Ma (Figure 3b), a change that also is influenced by model Earth system feedbacks. Such feedbacks include temperature-dependent, ocean remineralization and a decline in land biomass mainly driven by the CO₂ decline (Figure 3f). The modelled, pre-MPT cooling (Figure 2) is forced by the combined effect of greenhouse gas reductions in CO₂, CH₄, and N₂O (Figure 3b,d) along with increased surface albedo from expanding snow and sea ice cover (Figure 3c) and land biosphere changes. Less air-sea gas exchange from expanding sea ice cover explains the $\Delta^{14}\text{C}$ decrease in the deep ocean up to 1.5 Ma but this decrease is limited in the deep Atlantic by slightly increasing AMOC (figure 3g,k).

Despite a mean ocean phosphate increase from 2.025 to 2.185 mmol m⁻³ (not shown), ocean new production decreases modestly over this interval (Figure 3e). This counterintuitive result is due to the model's temperature-dependent remineralization scheme, that shifts phosphate farther down from the lighted ocean surface layer in response to ocean cooling. Deeper remineralization

also helps explain the modest, pre-MPT decline in deep ocean O_2 (Figure 3i). The modelled deepening of the carbonate compensation depth (CCD) from 4 to 1.5 Ma (Figure 3h) is broadly consistent with records from the Equatorial Pacific (Pälike et al., 2012,) and global-scale estimates based on sea water composition reconstructions (Zeebe & Tyrrell, 2019). Finally, our modelled DIC decrease in the deep ocean (Figure 3j) is representative for the global mean ocean, pre-MPT decrease of 0.113 mol m^{-3} over this period (not shown), consistent with enhanced burial of carbonate in ocean sediments (indicated by the CCD deepening) and net removal of carbon from the ocean.

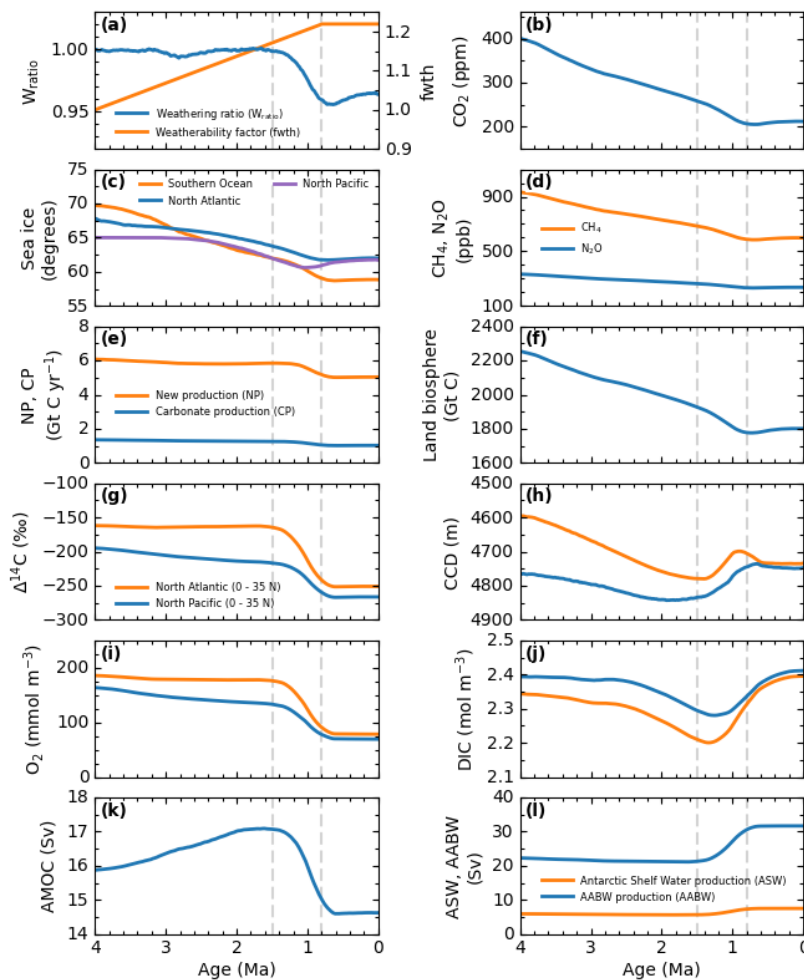


Figure 3. Forcing and property evolutions from 4 to 0 Ma for the standard case, model simulation. **a.** Applied weatherability factor and ratio of weathering rate to weathering at 4Ma, **b.** Atmospheric CO_2 concentration, **c.** Sea ice line position in the model Southern, North Atlantic and North Pacific Oceans, **d.** Atmospheric methane and nitrous oxide concentrations, **e.** Total ocean, new and calcium carbonate production, **f.** Total land biosphere biomass, **g.** $\Delta^{14}C$ at 4000 m depth of Atlantic and Pacific, 0 - 35°N model sectors. Values calculated with atmospheric $\Delta^{14}C$ held at 0 ‰, **h.** Carbonate Compensation Depth for Atlantic and Pacific, 0 - 35°N model sectors, **i.**

Dissolved oxygen concentration at 4000 m depth of Atlantic and Pacific, 0 - 35°N model sectors, **j.** Dissolved inorganic carbon concentration at 4000 m depth of Atlantic and Pacific, 0 - 35°N model sectors, **k.** Atlantic Meridional Overturning Current strength at 35°N in Sverdrup (Sv, $10^6 \text{ m}^3/\text{s}$), and **l.** Antarctic Shelf Water (ASW) and Antarctic Bottom Water (AABW) production. The weatherability factor and the weathering ratio apply to all forms of model weathering: silicate, carbonate, old organic carbon and phosphorus for which 4 Ma weathering rates are $0.0786 \text{ GtC yr}^{-1}$, $0.0924 \text{ GtC yr}^{-1}$, $0.0228 \text{ GtC yr}^{-1}$ and $0.00122 \text{ GtP yr}^{-1}$, respectively.

3.1.3. Model MPT property evolutions

Weathering decreases across the MPT as the effect from more rapid MPT cooling overcomes that from a continued weatherability factor increase (Figure 3a). The rate of atmospheric CO₂ drawdown accelerates then, reflecting the combined influence of weathering and the additional climate–carbon cycle processes listed in Table 1 and discussed in more detail below. By 0.8 Ma, atmospheric CO₂ falls to 207.4 ppm, not so far below the updated mean Antarctic ice core value of 216.4 ppm for the 0.8 - 0.65 Ma interval (Bereiter et al. 2015). Sea ice expands and methane/nitrous oxide concentrations decrease faster in response to intensified MPT cooling (Figure 3c,d). The land biosphere loses biomass more rapidly (Figure 3f) as CO₂ fertilization weakens and biosphere land cover declines due to the prescribed equatorward advance of the NH ice sheets (Table 1).

Global ocean new production also declines more sharply across the MPT (Figure 3e) despite enhanced dust fertilization prescribed in the Southern Ocean (Table 1). This apparent paradox can be reconciled through a closer look at model results and feedbacks. New production in the Southern Ocean (all of the ocean south of 35°S) indeed increases in response to the enhanced dust fertilization but this gain is modest, 0.15 GtC yr⁻¹, limited in part by more extensive ice cover there (Figure 3c). This gain outweighed by more substantial declines of 0.75 GtC yr⁻¹ in the phosphate-limited ocean zone between 35°S and 35°N (Table S1). Less phosphate is upwelled into the Southern Ocean surface layer from the applied reduction of Ekman transport across 55°S (Table 1). At the same time, enhanced uptake from dust-stimulated production further reduces surface layer phosphate there. As a consequence, water subducted into northward-flowing Antarctic Intermediate Water is more phosphate-depleted. This leads to less phosphate at intermediate depths farther northward, less phosphate transport into lighted surface layers there and less new production. In addition, as discussed above, deeper remineralization from colder ocean water shifts phosphate farther down from the lighted ocean surface layer. It should be noted here that decreased new production in macronutrient-limited ocean areas – in our model everywhere outside the Southern Ocean - has limited effect on atmospheric CO₂ due to Redfield coupling of nutrients and carbon in new production and remineralization (Sarmiento & Toggweiler, 1984; Shaffer, 1993).

The application of the standard case forcings across the MPT (Table 1) produces major changes in deep ocean properties. These include significant decreases in $\Delta^{14}\text{C}$ and dissolved oxygen, CCD shoaling, DIC rise and increasing homogenization between the Atlantic and Pacific basins (Figure 3g–j). Taken together, these trends describe a progressively older, more acidic, and more uniform deep water mass—despite a pronounced increase in AABW formation (Figure 3l). This apparent contradiction can be explained with the help of simulation results in Figure 4.

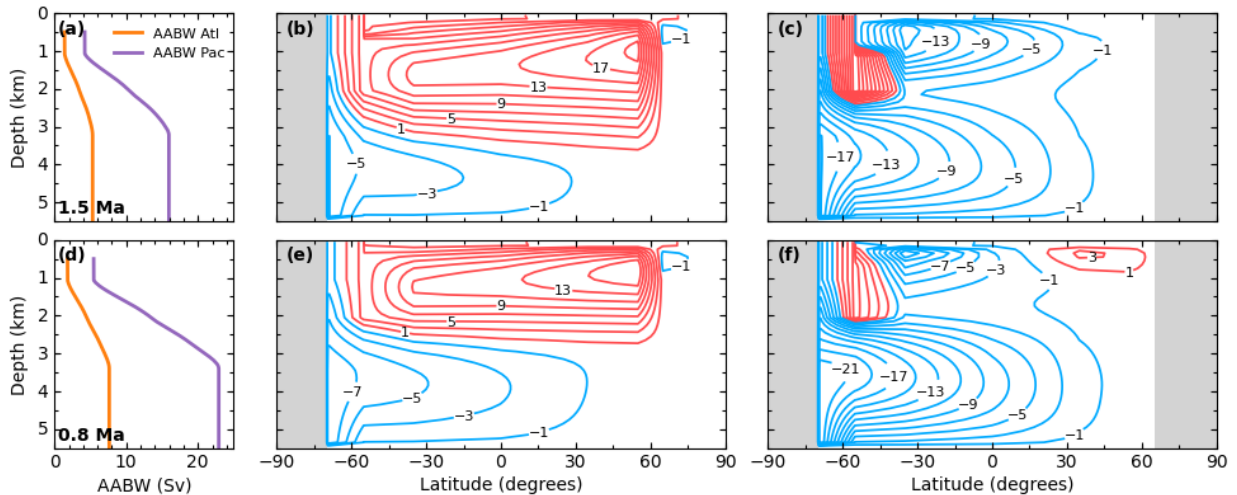


Figure 4. Standard case simulation, overturning circulations and Antarctic Bottom Water details at the beginning and end of the MPT. **a.** Depth distribution of AABW transport in the Atlantic (orange) and Pacific (violet) sectors, **b.** Atlantic overturning circulation and **c.** Pacific overturning circulation, all at 1.5 Ma. **d.-f.** As above but for 0.8 Ma. Total Antarctic Shelf Water, entrainment and AABW have been partitioned between model Atlantic and Pacific in the ratio 1:3.

The large increase in AABW formation across the MPT is initiated by the production of denser Antarctic Shelf Water due to brine rejection from the prescribed increase in sea ice and iceberg export from the shelf (Table 1). However, the bulk of the AABW transport increase arises not directly from shelf processes but rather from entrainment of ambient waters at $\sim 1000\text{--}3000$ m depth. This can be seen by comparing the AABW increases at 500 m from Fig. 4a to Fig. 4d with increases in the $\sim 1000\text{--}3000$ m depth range from Fig. 4a to Fig. 4d. This entrainment increase leads to enhanced deep ocean recirculation, isolated from the atmosphere (Figure 4b,c,e,f), which explains the decline in $\Delta^{14}\text{C}$ despite increased AABW flow. When effects of increased Southern Ocean dust fertilization and deeper remineralization are added, there is also a large increase in deep ocean remineralization. This further lowers dissolved oxygen and

acidifies the water mass, enhancing sediment CaCO_3 dissolution and, thereby, CCD shoaling. The associated rise in carbonate ion concentration from dissolution reduces oceanic dissolved CO_2 , and through air-sea gas exchange, contributes to atmospheric CO_2 drawdown. At the same time, combined carbon inputs from deep remineralization and CaCO_3 dissolution explain the modelled DIC rise across the MPT. These changes are consistent with multiple lines of paleoceanographic evidence for the development of a low-oxygen, carbon-rich deep water mass across the MPT (Farmer et al., 2019; Lear et al., 2016; Thomas et al., 2022). Importantly, the development of this isolated, deep water mass stems from strong, deep AABW recirculation and not, as might be thought, from weaker AABW formation.

Modelled changes in Atlantic overturning circulations across the MPT show that the increase in deep, AABW circulation leads to AMOC shoaling and weakening (Figure 4b,e; Figure 3k). Significant changes also occur in the Pacific overturning circulation including the emergence of a shallow, clockwise overturning cell in the North Pacific forming North Pacific Intermediate

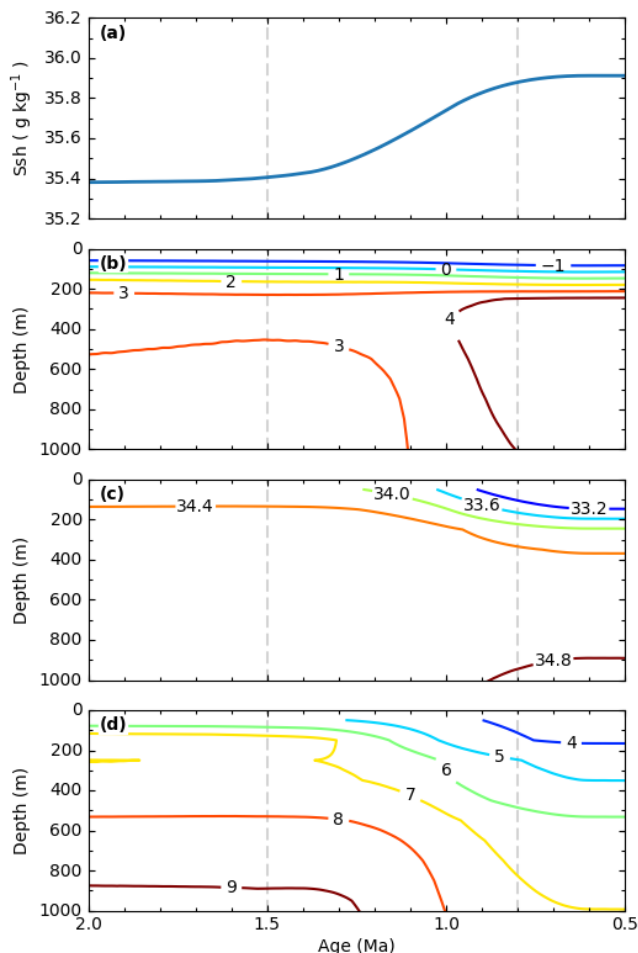


Figure 5. Standard case model property changes in the high southern latitude ocean from 2 to 0.5 Ma. **a.** Antarctic shelf salinity as well as **b.** Temperature ($^{\circ}\text{C}$), **c.** Salinity and **d.** Vertical diffusivity ($10^{-5} \text{ m}^2/\text{s}$) changes in the upper 1000 m of the $55^{\circ} - 69^{\circ}\text{S}$ model sector.

water, as has been inferred for the MPT from benthic $\delta^{18}\text{O}$ data (Kender et al., 2018). Northward, near surface heat transport associated with this cell likely explains the simulated northward retreat of the North Pacific sea ice edge at the end of the MPT (Figure 3c).

Our prescribed increase in sea ice and iceberg export from the Antarctic shelf across the MPT not only raises shelf salinity by way of brine rejection (Figure

5a) but also helps to freshen the upper Southern Ocean as this ice melts (Figure 5c). This freshening is also facilitated by less upwelling there of relatively-salty North Atlantic Deep Water due to the prescribed decrease in Ekman transport. This leads to increased upper ocean stratification there and, as a consequence, decreased model vertical diffusivity (Figure 5d). The associated decline in upward diffusive heat flux helps to warm intermediate waters in the Southern Ocean (Figure 5b). This decline, when compounded with less upward advective heat transport from weakened, equatorward-shifted SWWs (Table 1) and less air-sea heat exchange from more extensive sea ice cover, can explain much of the observed, amplified Southern Hemisphere cooling across the MPT (Figure 1b,c). Likewise, these changes severely narrow the Southern Ocean “window” to the atmosphere, helping to trap CO₂ in the ocean and draw down atmospheric CO₂.

3.2. Sensitivities to individual MPT forcings

3.2.1. Isolated impacts of standard case forcings

To better understand the drivers of simulated climate changes across the MPT, we examine here the individual contributions and interactions of the applied forcings. Figures 6 and 7 present SST and property responses to individual MPT forcing components outlined in Table 1.

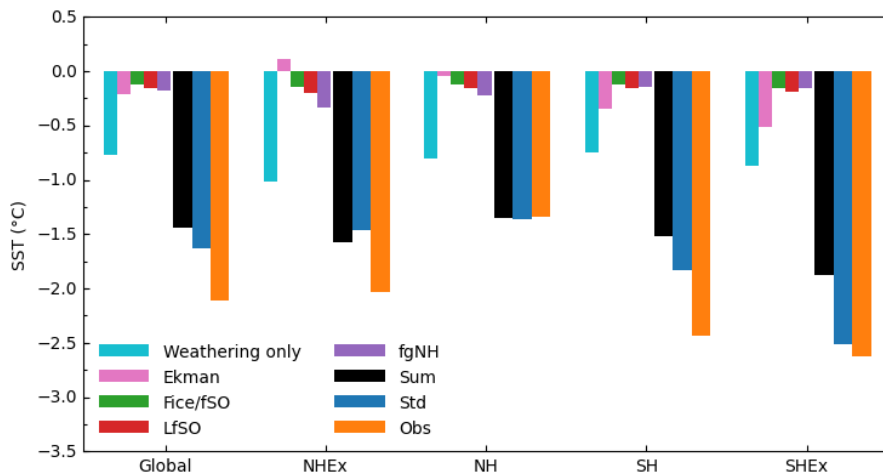


Figure 6. Comparison of modelled to observed SST change from 1.5 to 0.8 Ma including model results for individual forcings listed in Table 1. Ekman, Fice/fSO, LfSO and fgNH results are changes relative to the weathering-only simulation for simulations forced by weathering and each

specific process. Sum is for the five processes (including weathering-only), Std is for the standard case simulation and Obs are observed changes from Clark et al. (2024). Global, NHEX, NH, SH and SHEX are as in figure 2. All results are for 400 kyr running means.

Among all forcings, the largest individual contribution to SST cooling during the MPT comes from weathering. Remember that here we assumed a continued increase in the non-temperature-

dependent weatherability factor (fwth in Equation 1) at the same rate applied prior to the MPT (Figure 3a). To isolate the effects of each forcing, we performed four additional MPT simulations. In each, we include weathering along with one of the other four forcings: 1. Southern West Wind strength and position (Ekman), 2. sea ice/iceberg export from the Antarctic shelf (Fice/fSO), 3. Southern Ocean dust fertilization (LfSO) or 4. Northern Hemisphere ice sheet extent (fgNH).

Figure 6 shows that individual forcings produce distinct magnitudes and patterns of SST cooling. For example, Southern Ocean dust fertilization leads to moderate, relatively uniform global cooling, driven by atmospheric CO₂ drawdown from enhanced new production there (Figure 7). In contrast, changes in SWWs yield strong cooling in high southern latitudes, falling off to slight warming in the extra-tropical NH. This pattern arises from reduced upwelling of warm, CO₂-rich, subsurface water in the Southern Ocean and a modest AMOC strengthening (Figure 7). Sea ice and iceberg export from the Antarctic shelf largely accounts for enhanced ASW and AABW formation, which in turn contributes to a weakened AMOC (Figure 7). SST cooling from sea ice/iceberg export alone is relatively weak, with slight enhancement at extra-tropical latitudes in both hemispheres (Figure 6). This modest cooling is linked to reduced heat and CO₂ exchange in the upper SO, due to enhanced upper ocean stratification and reduced

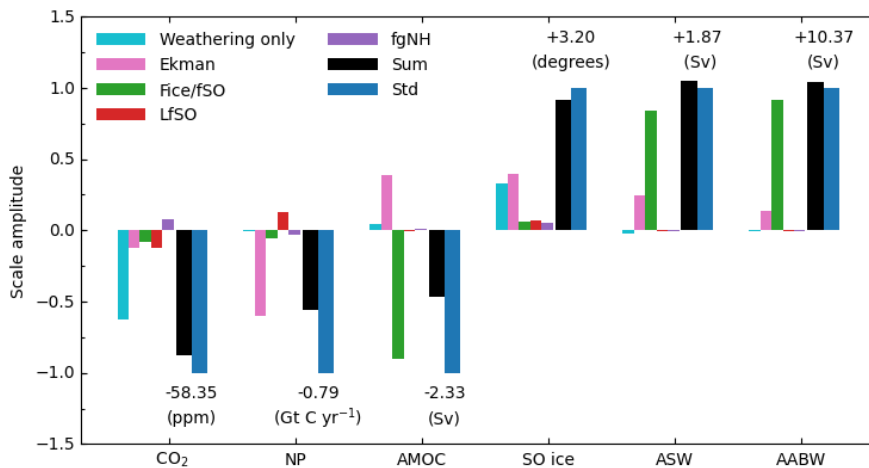


Figure 7. Comparison of modelled to observed property change from 1.5 to 0.8 Ma including model results for individual processes (listed in Table 1). Properties considered are atmospheric CO₂, ocean new production (NP), Atlantic Meridional

Overturning Current (AMOC) strength at 35°N, northward sea ice extent in the Southern Ocean, Antarctic Shelf Water (ASW) production and Antarctic Bottom Water (AABW) production. The results are changes relative to the weathering-only simulation for simulations forced by weathering and each specific process. Sum and Std as in Figure 6. All results are for 400 kyr running means, here normalized to a value of 1 for Std results (Std property values are also shown).

vertical diffusivity in the model as discussed above. The cooling structure is further influenced by the redistribution of heat between hemispheres from the weakened AMOC. Equatorward extension of NH ice sheets induces cooling through increased surface albedo but also warming from atmospheric CO₂ input from a shrinking land biomass. As shown in Figure 6, the albedo effect dominates in the model with SST cooling decreasing from north to south.

Comparisons between the summed effects of individual forcings and the standard case simulation results (black and blue bars, respectively; Figures 6 and 7) help show if the forcings interact to produce the final model results and if so, how they interact. Summed NH SST decreases match standard case results, suggesting little interaction between forcings. This outcome is not unexpected, given that our analysis focuses primarily on SH forcing and the only NH forcing considered does not directly interact with the ocean. In the Southern Hemisphere, the summed SST changes fall short of the standard case results, indicating that interactions among forcings are essential for reproducing the standard case cooling. A notable example, discussed earlier, is the combined effect of surface freshening from sea ice and iceberg melt with SWW-driven reductions in upwelling. Together, these processes suppress vertical exchange in the Southern Ocean, enhancing SST cooling. For ASW and AABW formation, the individual sums align well with the standard case results, as these changes are mainly driven by sea ice and iceberg export (Figure 7). However, for variables like ocean new production and AMOC strength, the summed individual contributions fall well short of the standard case results, underlining the importance of forcing interactions. As discussed earlier, the combined effects of dust fertilization and reduced upwelling in the Southern Ocean lower phosphate concentrations at intermediate depths in much of the ocean, thereby decreasing global new production.

3.2.2 Impacts of forcing changes

To further assess model sensitivity to applied MPT forcing we carried out a large number of additional simulations from 1.5 to 0.8 Ma (Figures S2-S7). These simulations started with standard case results at 1.5 Ma, used standard case weatherability and maintained the prescribed time structure of the remaining forcings (10% up to 1.2 Ma and the rest up to 0.8 Ma; Table 1). For each run, we varied the 0.8 Ma value of one of the forcings/forcings combinations while maintaining the others at their standard case values (Table 1).

In the presence of other MPT forcings, there was a particularly strong SH and global SST cooling, as well as atmospheric CO₂ lowering, for a reduction in Ekman transport across 55°S from 15 to 10 Sv (Figure S2a,c,d,f). In contrast, for this case, extra-tropical, Northern Hemisphere SST increased slightly, which can be attributed to a weaker AMOC (Figures S2e and S3c). Ocean new production drops considerably for a decrease in this Ekman transport from 20 to 10 Sv (Figure S3a). Rates of SH and global cooling as well as atmospheric CO₂ lowering are particularly sensitive to standard case, Antarctic shelf, sea ice export of 0.15 to 0.3 Sv; further increases in this forcing lead to considerably less change (Figure S4a,c,d,f). While the rate of ASW production increase slows with more ice export, AABW formation continues to accelerate (Figure S5b, d). This reflects feedbacks from fresher water at SO intermediate depths (Figure 5) affecting properties of water flowing onto the shelf and rates and locations of entrainment into the downflowing AABW plume. Dust fertilization contributes to atmospheric CO₂ drawdown but at a rate that diminishes with increasing fertilization intensity (Figure S6b). Enhanced rates of cooling and CO₂ increase with the equatorward expansion of NH ice sheets - via associated changes in albedo and land biosphere biomass - are primarily due to the increasing land area per degree of latitudinal extension (Figure S7a-d).

Finally, results in Figures S2-S7 can be used to tune the model for an improved fit to observed SST drops across the MPT (orange bars in Figure 6). For example, extension of the NH ice sheets to 55°N (from the standard case, 0.8 Ma value of 58.5°N) would enhance model cooling, particularly for the extra-tropical NH, while raising atmospheric CO₂ to be more in line with ice core observations (Bereiter et al. 2015).

4. Discussion

Here we applied the DCESS II Earth System model (Fernandez & Shaffer 2025) to better understand the strong, observed cooling across the Middle Pleistocene Transition from about 1.5 to 0.8 million years ago. During the MPT, glacial-interglacial cycles became longer, stronger and more asymmetric. Various underlying causes for this transition have been proposed (An et al., 2024; Clark et al., 2006; Clark et al., 2024; Raymo et al., 2006; Ruddiman et al., 1986; Tziperman & Gildor, 2003; Willeit et al., 2019) but it appears clear that the strong cooling laid

the groundwork this for system change by, for example, forcing Northern Hemisphere ice sheet growth.

We devised a standard-case simulation that reproduces main features of observed global and regional SST trends over the last 4 million years (Clark et al., 2024), including relatively uniform global cooling from 4 to 1.5 Ma, followed by accelerated and regionally variable cooling across the MPT. To match observed SST and atmospheric CO₂ at 4 Ma, we needed to use a high-end, climate-sensitivity of 5°C per CO₂ doubling (See above and Supporting Information). Then initial, simulated pre-MPT cooling was ultimately forced by an applied, linearly-increasing weatherability, representing non-temperature-dependent weathering changes from factors like mountain building. Since weatherability as so defined would not be expected to be climate-dependent, we applied this same calibrated rate increase across the MPT, explaining part of the cooling there. To address the remaining MPT cooling and inspired by recent analyses indicating the importance of Southern Hemisphere processes then (Clark et al., 2024; An et al., 2024), we considered three Southern Hemisphere forcings: 1. Southern West Wind strength and position, 2. Sea ice and iceberg export from the Antarctic shelf, 3. Southern Ocean dust fertilization and add as an additional forcing, 4. Northern Hemisphere ice sheet extent.

In the standard case simulation, CO₂ declined from 400 ppm at 4 Ma to 259 ppm at 1.5 Ma and then by 0.8 Ma fell to 207.4 ppm, a value in reasonable agreement with ice core results (Bereiter et al. 2015). There were significant decreases in deep ocean $\Delta^{14}\text{C}$ and dissolved oxygen across the MPT. When combined with modelled CCD shoaling, DIC rise and increasing homogenization between the Atlantic and Pacific basins, these trends show the development of an older, carbon-rich, more acidic and more uniform deep water mass, as in reconstructions (Farmer et al., 2019; Lear et al., 2016; Thomas et al., 2022). This followed a large increase in Antarctic Bottom Water (AABW) formation across the MPT, initiated by more formation of denser Antarctic Shelf Water from greater brine rejection due to the prescribed increase in sea ice and iceberg export from the shelf (Table 1). However, the most of the AABW transport increase comes from enhanced entrainment of deeper waters as the AABW plume in our gravity current approach flows down the Antarctic slope. This leads to enhanced deep ocean recirculation, isolated from the atmosphere, and explains the deep water mass mentioned above

and, thereby, much of the atmospheric CO₂ decrease across the MPT that was not explained by weathering.

The prescribed increase in sea ice and iceberg export from the Antarctic shelf also freshened the upper Southern Ocean as this ice melted (Figure 5c). Together with less upwelling of relatively-salty water carried by the Atlantic Meridional Overturning Circulation, due to the prescribed weaker, equatorward- displaced Southern West Winds, this led to increased upper ocean stratification and decreased model vertical diffusivity there. Less upward heat transport from mixing and advection and less air-sea heat exchange from more extensive Southern Ocean sea ice cover explained much of the observed, amplified Southern Hemisphere SST cooling across the MPT. Likewise, this combination further trapped carbon in the deep ocean, helping to draw down atmospheric CO₂.

Dust fertilization in the Southern Ocean enhanced ocean new production there, thereby contributing 6-7 ppm to MPT CO₂ decline for a fertilization doubling, whether applied alone or together with the other MPT forcings. Our sensitivity studies showed saturation of CO₂ drawdown for still more fertilization. This could be explained by the redistribution of ocean phosphate to deeper layers, tending to self-limit Southern Ocean new production. In addition, Southern Ocean dust fertilization led to less phosphate in northward-flowing Antarctic Intermediate Water and, therefore, at intermediate depths in the global ocean. Together with the vertical redistribution effect, this led to reduced global new production. These results point toward a more modest role of dust fertilization in CO₂ drawdown and global cooling than found in other work (Martinez-Garcia et al., 2009; Shaffer & Lambert 2018).

Our standard case simulation is able to explain most of the size and structure of observed SST cooling across the MPT, but some of the cooling remains unaccounted for. Our sensitivity studies showed that surface albedo increase from more applied equatorward expansion of Northern Hemisphere ice sheets could help out. However, some of the remaining cooling is likely explained by other processes and interactions not considered, nor indeed addressable, by our simplified model. For example, longer, stronger and more asymmetric glacial-interglacial cycles developed across the MPT with longer glacial and shorter interglacial periods. Mean temperatures across such cycles would show more cooling because of this asymmetry alone.

Our analysis underlines the importance of modelling AABW formation in agreement with observations that show AABW to originate from dense Antarctic Shelf Water, formed by brine-rejection, and that this precursor flows down the Antarctic slope entraining surrounding water as it descends into the deep ocean to become AABW (Gordon, 2019; Orsi, et al., 2002). Our DCESS II model uses a simplified gravity current - entrainment formulation to capture this chain of events (Fernández and Shaffer, 2025). Deep recirculation that follows from this formulation was a key factor in our modelled atmospheric CO₂ drawdown across the MPT but such deep recirculation would be missed, or at least misrepresented, in the bulk of Earth system models, as they rely on deep convection or omit downslope entrainment processes when forming AABW (Heuzé, 2021).

While much remains for future work on the Middle Pleistocene Transition, our results here underline the central role that mid- and high latitude, Southern Hemisphere processes play in ushering in the MPT by forcing strong global and regional cooling across it.

Acknowledgments

This research was supported by Fondecyt grant 1230534 from the Chilean Agencia Nacional de Investigación y Desarrollo (ANID). There are no conflicts of interest.

Open Research

The DCESS II model code used in this study is available at <https://doi.org/10.5281/zenodo.16573050>. This version reproduces our standard MPT simulation. For the additional experiments (e.g., sensitivity tests), see the accompanying README.txt at this site for configuration instructions.

References

Abe-Ouchi, A., Saito, F., Kawamura, K., Raymo, M. E., Okuno, J. I., Takahashi, K., & Blatter, H. (2013). Insolation-driven 100,000-year glacial cycles and hysteresis of ice-sheet volume. *Nature*, 500(7461), 190-193. <https://doi.org/10.1038/nature12374>.

- Amante, C., & Eakins, B. W. (2009). ETOPO1 arc-minute global relief model: : Procedures, Data Sources and Analysis. NOAA Technical Memorandum NESDIS NGDC-24 [dataset]. *National Geophysical Data Center, NOAA*. <https://doi.org/10.7289/V5C8276M>.
- An, Z., Zhou, W., Zhang, Z., Zhang, X., Liu, Z., Sun, Y., et al. (2024). Mid-Pleistocene climate transition triggered by Antarctic Ice Sheet growth. *Science*, *385*(6708), 560-565. <https://doi.org/10.1126/science.abn4861>.
- Ao, H., Rohling, E. J., Li, X., Song, Y., Roberts, A. P., Han, Y., et al. (2023). Northern hemisphere ice sheet expansion intensified Asian aridification and the winter monsoon across the mid-Pleistocene transition. *Communications Earth & Environment*, *4*(36). <https://doi.org/10.1038/s43247-023-00686-9>.
- Anderson, R. F., Ali, S., Bradtmiller, L. I., Nielsen, S. H. H., Fleisher, M. Q., Anderson, B. E., & Burckle, L. H. (2009). Wind-Driven upwelling in the Southern Ocean and the deglacial rise in atmospheric CO₂. *Science*, *323*(5920), 1443-1448. <https://doi.org/10.1126/science.1167441>.
- Baines, P. G. (2005). Mixing regimes for the flow of dense fluid down slopes into stratified environments. *Journal of Fluid Mechanics*, *538*, 245-267. <https://doi.org/10.1017/S0022112005005434>.
- Baines, P. G. (2008). Mixing in downslope flows in the ocean - plumes versus gravity currents. *Atmosphere-Ocean*, *46*(4), 405-419. <https://doi.org/10.3137/ao.460402>.
- Bartoli, G., Hönisch, B., & Zeebe, R. E. (2011). Atmospheric CO₂ decline during the Pliocene intensification of Northern Hemisphere glaciations. *Paleoceanography*, *26*(4), PA4213. <https://doi.org/10.1029/2010PA002055>.
- Batchelor, C. L., Margold, M., Krapp, M., Murton, D. K., Dalton, A. S., Gibbard, P. L., et al. (2019). The configuration of Northern Hemisphere ice sheets through the Quaternary. *Nature Communications*, *10*(3713). <https://doi.org/10.1038/s41467-019-11601-2>.
- Bayon, G., Patriat, M., Godderis, Y., Trinquier, A., De Deckker, P., Kulhanek, D. K., et al. (2023). Accelerated mafic weathering in Southeast Asia linked to late Neogene cooling. *Science Advances*, *9*(13), eadf3141. <https://doi.org/10.1126/sciadv.adf3141>.

- Bereiter, B., Eggleston, S., Schmitt, J., Nehrbass-Ahles, C., Stocker, T. F., Fischer, H., et al. (2015). Revision of the EPICA Dome C CO₂ record from 800 to 600 kyr before present. *Geophysical Research Letters*, *42*(2), 542-549. <https://doi.org/10.1002/2014GL061957>.
- Berends, C. J., Köhler, P., Lourens, L. J., & Van De Wal, R. S. W. (2021). On the Cause of the Mid-Pleistocene Transition. *Reviews of Geophysics*, *59*, e2020RG000727. <https://doi.org/10.1029/2020RG000727>.
- Berger, A., & Loutre, M. F. (1991). Insolation values for the climate of the last 10 million years. *Quaternary Science Reviews*, *10*(4), 297-317. [https://doi.org/10.1016/0277-3791\(91\)90033-Q](https://doi.org/10.1016/0277-3791(91)90033-Q).
- Bintanja, R., & Van De Wal, R. S. W. (2008). North American ice-sheet dynamics and the onset of 100,000-year glacial cycles. *Nature*, *454*(7206), 869-872. <https://doi.org/10.1038/nature07158>.
- Clark, P. U., Archer, D., Pollard, D., Blum, J. D., Rial, J. A., Brovkin, V., et al. (2006). The middle Pleistocene transition: characteristics, mechanisms, and implications for long-term changes in atmospheric pCO₂. *Quaternary Science Reviews*, *25*(23), 3150-3184. <https://doi.org/10.1016/j.quascirev.2006.07.008>.
- Clark, P. U., & Pollard, D. (1998). Origin of the Middle Pleistocene Transition by ice sheet erosion of regolith. *Paleoceanography*, *13*(1), 1-9. <https://doi.org/10.1029/97PA02660>.
- Clark, P. U., Shakun, J. D., Rosenthal, Y., Köhler, P., & Bartlein, P. J. (2024). Global and regional temperature change over the past 4.5 million years. *Science*, *383*(6685), 884-890. <https://doi.org/10.1126/science.adi1908>.
- Depoorter, M. A., Bamber, J. L., Griggs, J. A., Lenaerts, J. T. M., Ligtenberg, S. R. M., Van Den Broeke, M. R., & Moholdt, G. (2013). Calving fluxes and basal melt rates of Antarctic ice shelves. *Nature*, *502*(7469), 89-92. <https://doi.org/10.1038/nature12567>.
- Elderfield, H., Ferretti, P., Greaves, M., Crowhurst, S., McCave, I. N., Hodell, D., & Piotrowski, A. M. (2012). Evolution of ocean temperature and Ice volume through the Mid-Pleistocene Climate Transition. *Science*, *337*(6095), 704-709. <https://doi.org/10.1126/science.1221294>.

- Farmer, J. R., Hönisch, B., Haynes, L. L., Kroon, D., Jung, S., Ford, H. L., et al. (2019). Deep Atlantic ocean carbon storage and the rise of 100,000-year glacial cycles. *Nature Geoscience*, *12*(5), 355-360. <https://doi.org/10.1038/s41561-019-0334-6>.
- Fedorov, A. V., Brierley, C. M., Lawrence, K. T., Liu, Z., Dekens, P. S., & Ravelo, A. C. (2013). Patterns and mechanisms of early Pliocene warmth. *Nature*, *496*(7443), 43-49. <https://doi.org/10.1038/nature12003>.
- Fedorov, A. V., Burls, N. J., Lawrence, K. T., & Peterson, L. C. (2015). Tightly linked zonal and meridional sea surface temperature gradients over the past five million years. *Nature Geoscience*, *8*(12), 975-980. <https://doi.org/10.1038/ngeo2577>.
- Fernández Villanueva, E., & Shaffer, G. (2025). Presentation, calibration and testing of the DCESS II Earth system model of intermediate complexity (version 1.0). *Geoscientific Model Development*, *18*(7), 2161-2192. <https://doi.org/10.5194/gmd-18-2161-2025>.
- Gordon, A. L. (2019). Bottom Water Formation. In J. K. Cochran, H. J. Bokuniewicz, & P. L. Yager (Eds.), *Encyclopedia of Ocean Sciences (Third Edition)* (pp. 120-126). Oxford: Academic Press. <https://doi.org/10.1016/B978-0-12-409548-9.04019-7>.
- Haumann, F. A., Gruber, N., Münnich, M., Frenger, I., & Kern, S. (2016). Sea-ice transport driving Southern Ocean salinity and its recent trends. *Nature*, *537*(7618), 89-92. <https://doi.org/10.1038/nature19101>.
- Herbert, T. D. (2023). The Mid-Pleistocene Climate Transition. *Annual Review of Earth and Planetary Sciences*, *51*, 389-418. <https://doi.org/10.1146/annurev-earth-032320-104209>.
- Heuzé, C. (2021). Antarctic Bottom Water and North Atlantic Deep Water in CMIP6 models. *Ocean Science*, *17*(1), 59-90. <https://doi.org/10.5194/os-17-59-2021>.
- Heywood, K. J., Schmidtko, S., Heuzé, C., Kaiser, J., Jickells, T. D., Queste, B. Y., et al. (2014). Ocean processes at the Antarctic continental slope. *Philosophical Transactions of the Royal Society A: Mathematical, Physical and Engineering Sciences*, *372*, 20130047. <https://doi.org/10.1098/rsta.2013.0047>.

- Hodell, D. A., & Channell, J. E. T. (2016). Mode transitions in Northern Hemisphere glaciation: co-evolution of millennial and orbital variability in Quaternary climate. *Climate of the Past*, *12*(9), 1805-1828. <https://doi.org/10.5194/cp-12-1805-2016>.
- Köhler, P. (2023). Atmospheric CO₂ concentration based on boron isotopes versus simulations of the global carbon cycle during the Plio-Pleistocene. *Paleoceanography and Paleoclimatology*, *38*(2), e2022PA004439. <https://doi.org/10.1029/2022PA004439>.
- Lamy, F., Gersonde, R., Winckler, G., Esper, O., Jaeschke, A., Kuhn, G., et al. (2014). Increased dust deposition in the Pacific Southern Ocean during glacial periods. *Science*, *343*(6169), 403-407. <https://doi.org/10.1126/science.1245424>.
- LaRiviere, J. P., Ravelo, A. C., Crimmins, A., Dekens, P. S., Ford, H. L., Lyle, M., & Wara, M. W. (2012). Late Miocene decoupling of oceanic warmth and atmospheric carbon dioxide forcing. *Nature*, *486*(7401), 97-100. <https://doi.org/10.1038/nature11200>.
- Lear, C. H., Billups, K., Rickaby, R. E. M., Diester-Haass, L., Mawbey, E. M., & Sosdian, S. M. (2016). Breathing more deeply: Deep ocean carbon storage during the mid-Pleistocene climate transition. *Geology*, *44*(12), 1035-1038. <https://doi.org/10.1130/G38636.1>
- Lisiecki, L. E., & Raymo, M. E. (2005). A Pliocene-Pleistocene stack of 57 globally distributed benthic $\delta^{18}\text{O}$ records. *Paleoceanography*, *20*, PA1003. <https://doi.org/10.1029/2004PA001071>.
- Martin, P. E., Macdonald, F. A., Mcquarrie, N., Flowers, R. M., & Maffre, P. J. Y. (2023). The rise of New Guinea and the fall of Neogene global temperatures. *Proceedings of the National Academy of Sciences*, *120*(40), e2306492120. <https://doi.org/10.1073/pnas.2306492120>.
- Martínez-García, A., Rosell-Melé, A., Geibert, W., Gersonde, R., Masqué, P., Gaspari, V., & Barbante, C. (2009). Links between iron supply, marine productivity, sea surface temperature, and CO₂ over the last 1.1 Ma. *Paleoceanography*, *24*, PA1207. <https://doi.org/10.1029/2008PA001657>.
- Martinez-Grcia, A., Rosell-Melé, A., Jaccard, S. L., Sigman, D. M. & Haug, G. H. (2011). Southern Ocean dust-climate coupling over the past four million years. *Nature*, *476*, 312-315. <https://doi.org/10.1038/nature10310>.

Medina-Elizalde, M., & Lea, D. W. (2005). The Mid-Pleistocene Transition in the Tropical Pacific. *Science*, *310*(5750), 1009-1012. <https://doi.org/10.1126/science.1115933>.

Nicholls, K. W., Østerhus, S., Makinson, K., Gammelsrød, T., & Fahrback, E. (2009). Ice-ocean processes over the continental shelf of the southern Weddell Sea, Antarctica: A review. *Reviews of Geophysics*, *47*(3), RG3003. <https://doi.org/10.1029/2007RG000250>.

Orsi, A. H., Smethie Jr., W. M., & Bullister, J. L. (2002). On the total input of Antarctic waters to the deep ocean: A preliminary estimate from chlorofluorocarbon measurements. *Journal of Geophysical Research*, *107*(C8). <https://doi.org/10.1029/2001JC000976>.

Pälike, H., Lyle, M. W., Nishi, H., Raffi, I., Ridgwell, A., Gamage, K., et al. (2012). A Cenozoic record of the equatorial Pacific carbonate compensation depth. *Nature*, *488*(7413), 609-614. <https://doi.org/10.1038/nature11360>.

Raymo, M. E., Lisiecki, L. E., & Nisancioglu, K. H. (2006). Plio-Pleistocene ice volume, Antarctic climate, and the global $\delta^{18}\text{O}$ record. *Science*, *313*(5786), 492-495. <https://doi.org/10.1126/science.1123296>.

Rignot, E., Jacobs, S., Mouginot, J., & Scheuchl, B. (2013). Ice-shelf melting around Antarctica. *Science*, *341*(6143), 266-270. <https://doi.org/10.1126/science.1235798>.

Rohling, E. J., Yu, J., Heslop, D., Foster, G. L., Opdyke, B., & Roberts, A. P. (2021). Sea level and deep-sea temperature reconstructions suggest quasi-stable states and critical transitions over the past 40 million years. *Science Advances*, *7*(26), eabf5326. <https://doi.org/10.1126/sciadv.abf5326>.

Ruddiman, W. F., Raymo, M., & McIntyre, A. (1986). Matuyama 41,000-year cycles: North Atlantic Ocean and northern hemisphere ice sheets. *Earth and Planetary Science Letters*, *80*(1), 117-129. [https://doi.org/10.1016/0012-821X\(86\)90024-5](https://doi.org/10.1016/0012-821X(86)90024-5).

Sarmiento, J. & Toggweiler, J. (1984) A new model for the role of the oceans in determining atmospheric $P\text{CO}_2$. *Nature*, *308*, 621–624. <https://doi.org/10.1038/308621a0>

Shaffer, G. (1993). Effects of the Marine Biota on Global Carbon Cycling. In Heimann, M. (Eds.), *The Global Carbon Cycle. NATO ASI Series*, vol 15 (pp. 431-455). Springer, Berlin, Heidelberg. https://doi.org/10.1007/978-3-642-84608-3_18.

Shaffer, G., & Lambert, F. (2018). In and out of glacial extremes by way of dust–climate feedbacks. *Proceedings of the National Academy of Sciences*, *115*(9), 2026-2031. <https://doi.org/10.1073/pnas.1708174115>.

Shaffer, G., Malskær Olsen, S., & Pepke Pedersen, J. O. (2008). Presentation, calibration and validation of the low-order, DCESS Earth System Model (Version 1). *Geoscientific Model Development*, *1*, 17-51. <https://doi.org/10.5194/gmd-1-17-2008>.

Shin, S. I., Liu, Z., Otto-Bliesner, B. L., Kutzbach, J. E., & Vavrus, S. J. (2003). Southern Ocean sea-ice control of the glacial North Atlantic thermohaline circulation. *Geophysical Research Letters*, *30*(2), 1096. <https://doi.org/10.1029/2002GL015513>.

Silva, T. A. M., Bigg, G. R., & Nicholls, K. W. (2006). Contribution of giant icebergs to the Southern Ocean freshwater flux. *Journal of Geophysical Research: Oceans*, *111*(C3), C03004. <https://doi.org/10.1029/2004JC002843>.

Snyder, C. W. (2016). Evolution of global temperature over the past two million years. *Nature*, *538*(7624), 226-228. <https://doi.org/10.1038/nature19798>.

Sosdian, S. M., Greenop, R., Hain, M. P., Foster, G. L., Pearson, P. N., & Lear, C. H. (2018). Constraining the evolution of Neogene ocean carbonate chemistry using the boron isotope pH proxy. *Earth and Planetary Science Letters*, *498*, 362-376. <https://doi.org/10.1016/j.epsl.2018.06.017>.

Starr, A., Hall, I. R., Barker, S., Rackow, T., Zhang, X., Hemming, S. R., et al. (2021). Antarctic icebergs reorganize ocean circulation during Pleistocene glacials. *Nature*, *589*(7841), 236-241. <https://doi.org/10.1038/s41586-020-03094-7>.

Thomas, N. C., Bradbury, H. J., & Hodell, D. A. (2022). Changes in North Atlantic deep-water oxygenation across the Middle Pleistocene Transition. *Science*, *377*(6606), 654-659. <https://doi.org/10.1126/science.abj7761>.

Toggweiler, J. R., Russell, J. L., & Carson, S. R. (2006). Midlatitude westerlies, atmospheric CO₂, and climate change during the ice ages. *Paleoceanography*, *21*(2), PA2005. <https://doi.org/10.1029/2005PA001154>.

Tziperman, E., & Gildor, H. (2003). On the mid-Pleistocene transition to 100-kyr glacial cycles and the asymmetry between glaciation and deglaciation times. *Paleoceanography*, *18*(1), 1001. <https://doi.org/10.1029/2001PA000627>.

Venugopal, A. U., Bertler, N. A. N., Severinghaus, J. P., Brook, E. J., Cortese, G., Lee, J. E., et al. (2023). Antarctic evidence for an abrupt northward shift of the Southern Hemisphere westerlies at 32 ka BP. *Nature Communications*, *14*, 5432. <https://doi.org/10.1038/s41467-023-40951-1>.

von der Heydt, A. S., Ashwin, P., Camp, C. D., Crucifix, M., Dijkstra, H. A., Ditlevsen, P., & Lenton, T. M. (2021). Quantification and interpretation of the climate variability record. *Global and Planetary Change*, *197*, 103399. <https://doi.org/10.1016/j.gloplacha.2020.103399>.

Westerhold, T., Marwan, N., Drury, A. J., Liebrand, D., Agnini, C., Anagnostou, E., et al. (2020). An astronomically dated record of Earth's climate and its predictability over the last 66 million years. *Science*, *369*(6509), 1383-1387. <https://doi.org/10.1126/science.aba6853>.

Willeit, M., Ganopolski, A., Calov, R., & Brovkin, V. (2019). Mid-Pleistocene transition in glacial cycles explained by declining CO₂ and regolith removal. *Science Advances*, *5*(4), eaav7337. <https://doi.org/10.1126/sciadv.aav7337>.

Zeebe, R. E., & Tyrrell, T. (2019). History of carbonate ion concentration over the last 100 million years II: Revised calculations and new data. *Geochimica et Cosmochimica Acta*, *257*, 373-392. <https://doi.org/10.1016/j.gca.2019.02.041>.

Role of mid- and high-latitude, Southern Hemisphere processes for ushering in the Middle Pleistocene Transition

Gary Shaffer¹, Esteban Fernández Villanueva² and Cyrus Karas³

¹Niels Bohr Institute, University of Copenhagen, 2100 Copenhagen Ø, Denmark

²Graduate Program in Oceanography, Department of Oceanography, Faculty of Natural Sciences and Oceanography, University of Concepción, P.O. Box 160-C, Concepción, Chile

³Universidad de Santiago de Chile, Av. Bernardo O'Higgins 3363, Santiago, Chile

Contents of this file

Text S1

Figures S1 to S7

Table S1

Introduction

The supporting information consists of a text file (Text S1) with a description of the minor modifications in the DCESS II model for this study, seven supporting figures (Figures S1-S7), and a table (Table S1).

Text S1. Minor model modifications

In addition to the modifications and improvements described in the main text, a few additional refinements were applied to the model setup in this study. These are described in the following.

First, to achieve the new equilibrium climate sensitivity of 5 °C per doubling atmospheric CO₂, we recalibrate the model atmospheric longwave radiation parameterization by choosing appropriate values of B and A_{PI} in equations 6 and 7 in Fernández & Shaffer (2025). Second, inflow from the Southern Ocean onto the Antarctic continental shelf is now implemented as an inflow at the shelf edge (500 m depth), rather than as a uniform inflow across the 0 - 500 m depth range. Third, under non-pre-industrial conditions, the originally fixed total freshwater forcing of the Southern Ocean shelf from precipitation, calving, and ice melting (F_g) is now taken as a time-dependent function of the annual mean atmospheric freshwater flux crossing 55° S such that,

$$F_g(t) = F_{g,PI} \times F_{w55}(t)/F_{w55,PI} \quad (1)$$

Where $F_{g,PI}$ is the pre-industrial (PI) total freshwater flux to the Southern Ocean shelf equal to 0.08 Sv (Depoorter et al., 2013; Rignot et al., 2013), slightly higher than 0.07 Sv used in Fernández & Shaffer (2015), and F_{w55} and $F_{w55,PI}$ are the time-dependent and the PI model annual mean atmospheric freshwater fluxes crossing 55° S, respectively.

References

Amante, C., & Eakins, B. W. (2009). ETOPO1 arc-minute global relief model: : Procedures, Data Sources and Analysis. NOAA Technical Memorandum NESDIS NGDC-24 [dataset]. *National Geophysical Data Center, NOAA*. <https://doi.org/10.7289/V5C8276M>.

Depoorter, M. A., Bamber, J. L., Griggs, J. A., Lenaerts, J. T. M., Ligtenberg, S. R. M., Van Den Broeke, M. R., & Moholdt, G. (2013). Calving fluxes and basal melt rates of Antarctic ice shelves. *Nature*, *502*(7469), 89-92. <https://doi.org/10.1038/nature12567>.

Fernández Villanueva, E., & Shaffer, G. (2025). Presentation, calibration and testing of the DCESS II Earth system model of intermediate complexity (version 1.0). *Geoscientific Model Development*, *18*(7), 2161-2192. <https://doi.org/10.5194/gmd-18-2161-2025>.

Rignot, E., Jacobs, S., Mouginot, J., & Scheuchl, B. (2013). Ice-shelf melting around Antarctica. *Science*, *341*(6143), 266-270. <https://doi.org/10.1126/science.1235798>.

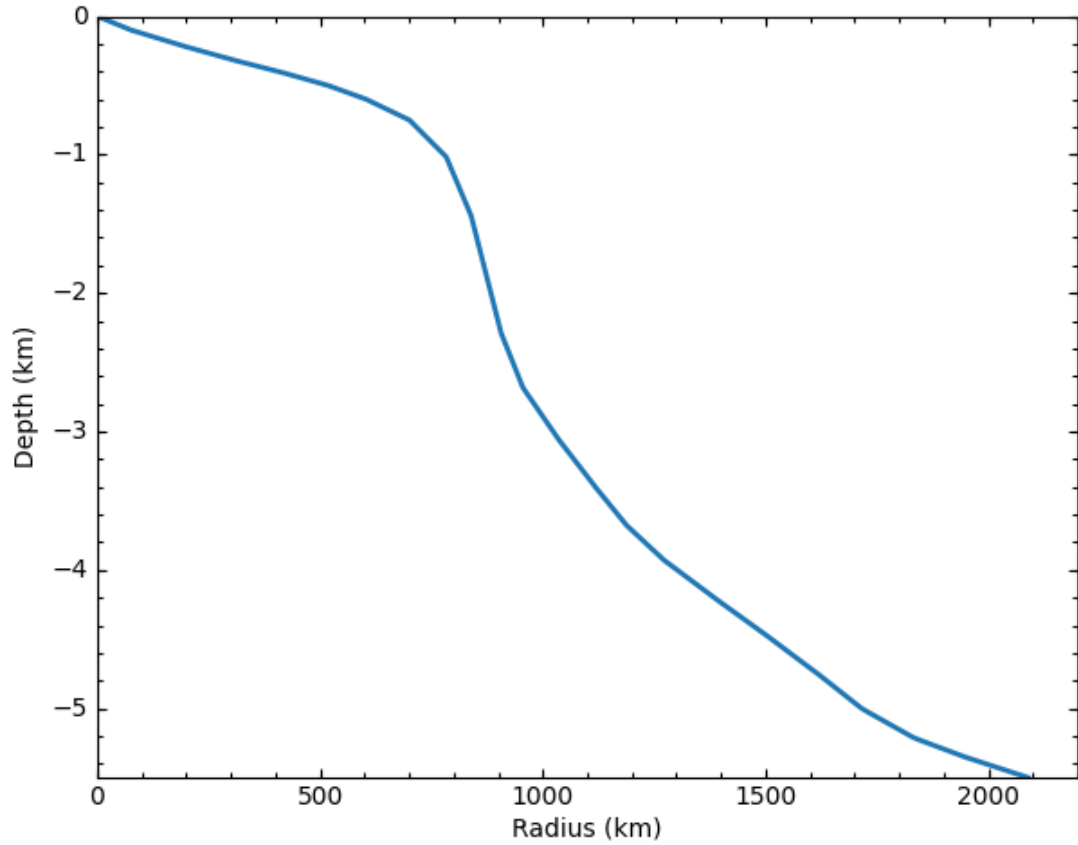


Figure S1. Observed depth profile for the Antarctic slope as projected to an axi-symmetric framework. The profile is used in DCESS II for the Antarctic Bottom Water formation (AABW) scheme and was calculated using the ETOPO1 database (Amante & Eakins 2009).

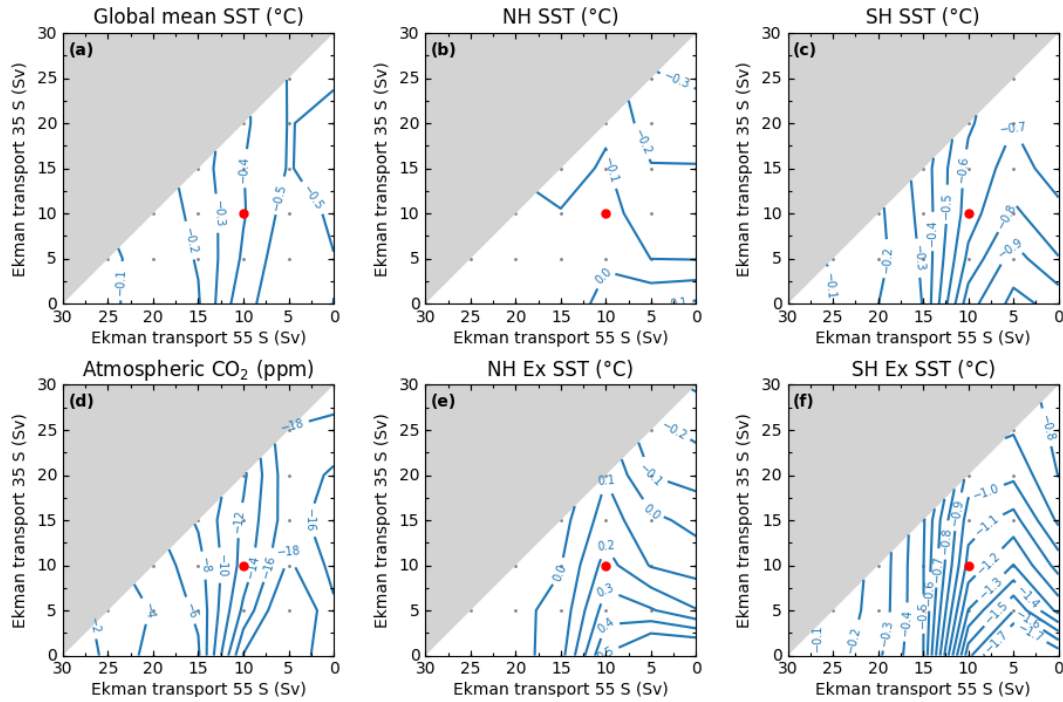


Figure S2. Sensitivity analysis showing the model response for specific combinations of northward Ekman transport at 55°S and 35°S (small gray dots), while all other forcings are applied using their standard case values (Table 1 in the main text). **a.** Global mean sea surface temperature (SST), **b.** Northern Hemisphere (NH) SST, **c.** Southern Hemisphere (SH) SST, **d.** Atmospheric CO₂, **e.** and **f.** Extratropical (35° -55°) SST for NH and SH, respectively. Contour lines indicate the change in a given property from 1.5 Ma to 0.8 Ma as described in the main text. 1.5 Ma forcing values are in the lower, left-hand corner. The red dot marks the combination for the standard MPT simulation at 0.8 Ma. We did not carry out simulations where the forcing combination exceeds 30 Sv (filled gray area).

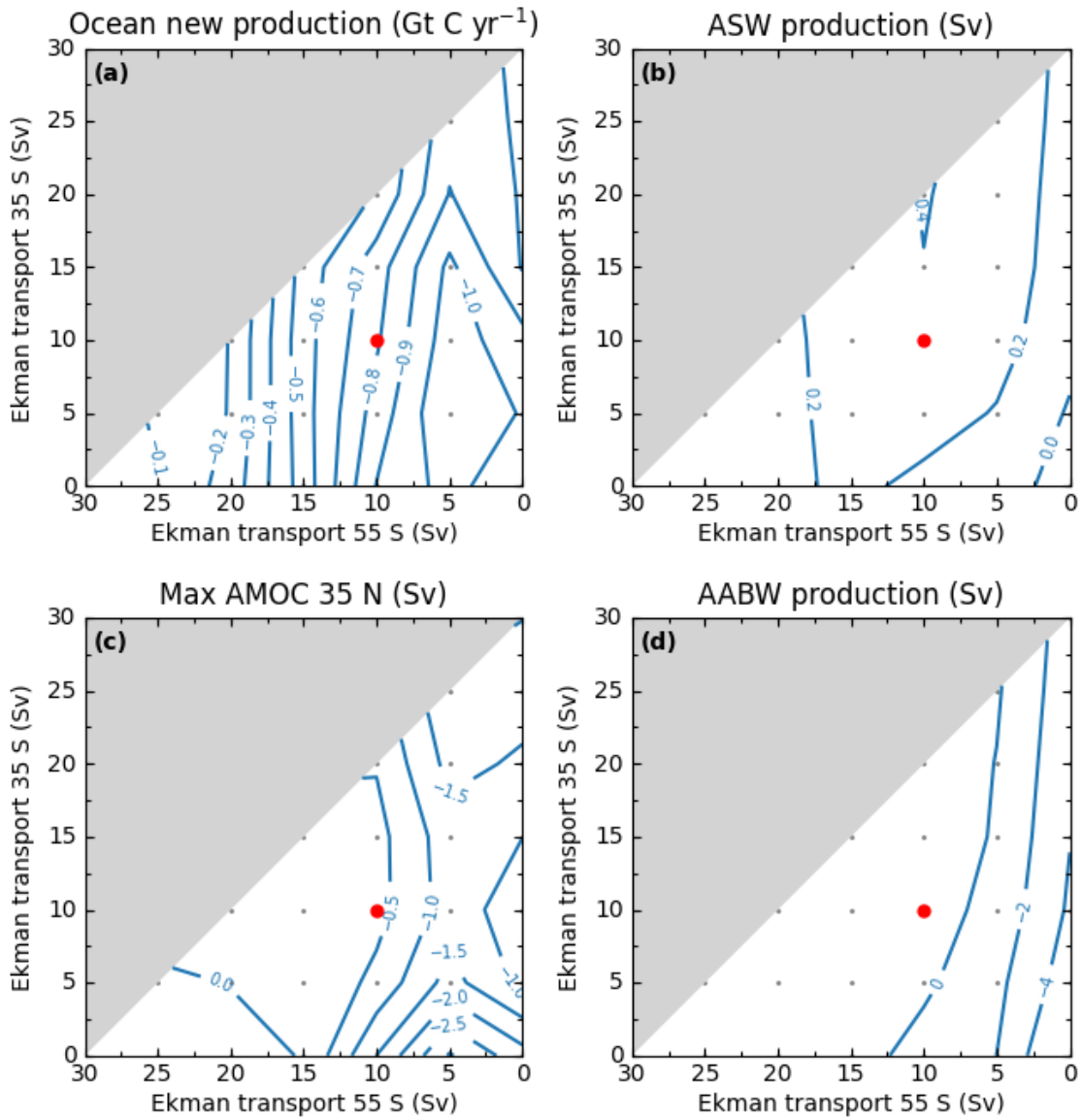


Figure S3. As in Figure S2 but for **a.** Ocean new production, **b.** Antarctic Shelf Water (ASW) production, **c.** Atlantic Meridional Overturning Circulation (AMOC) strength at 35 °N and **d.** AABW production.

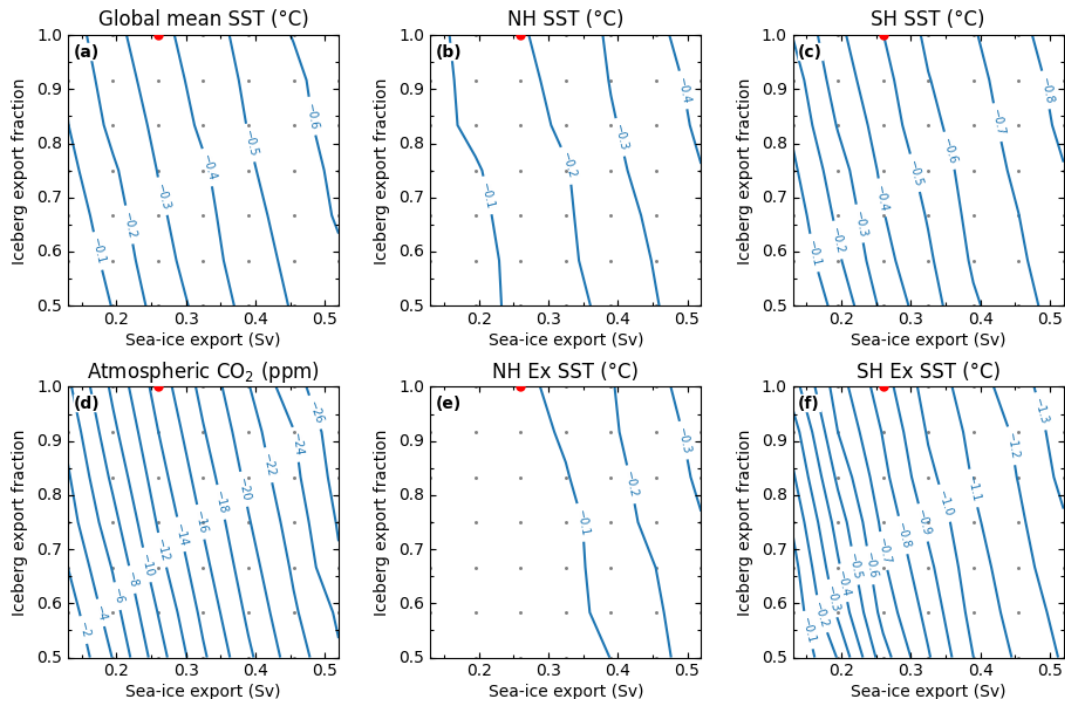


Figure S4. Sensitivity analysis showing the model response for specific combinations of sea ice and iceberg export out of the Southern Ocean shelf (small gray dots), while all other forcings are applied using their standard case values (Table 1 in the main text). **a.** Global mean sea surface temperature (SST), **b.** Northern Hemisphere (NH) SST, **c.** Southern Hemisphere (SH) SST, **d.** Atmospheric CO₂, **e.** and **f.** Extratropical (35° -55°) SST for NH and SH, respectively. Contour lines indicate the difference in a given property between at 0.8 Ma and 1.5 Ma as described in the main text. 1.5 Ma forcing values are in the lower, left-hand corner. The red dot marks the combination for the standard MPT simulation at 0.8 Ma.

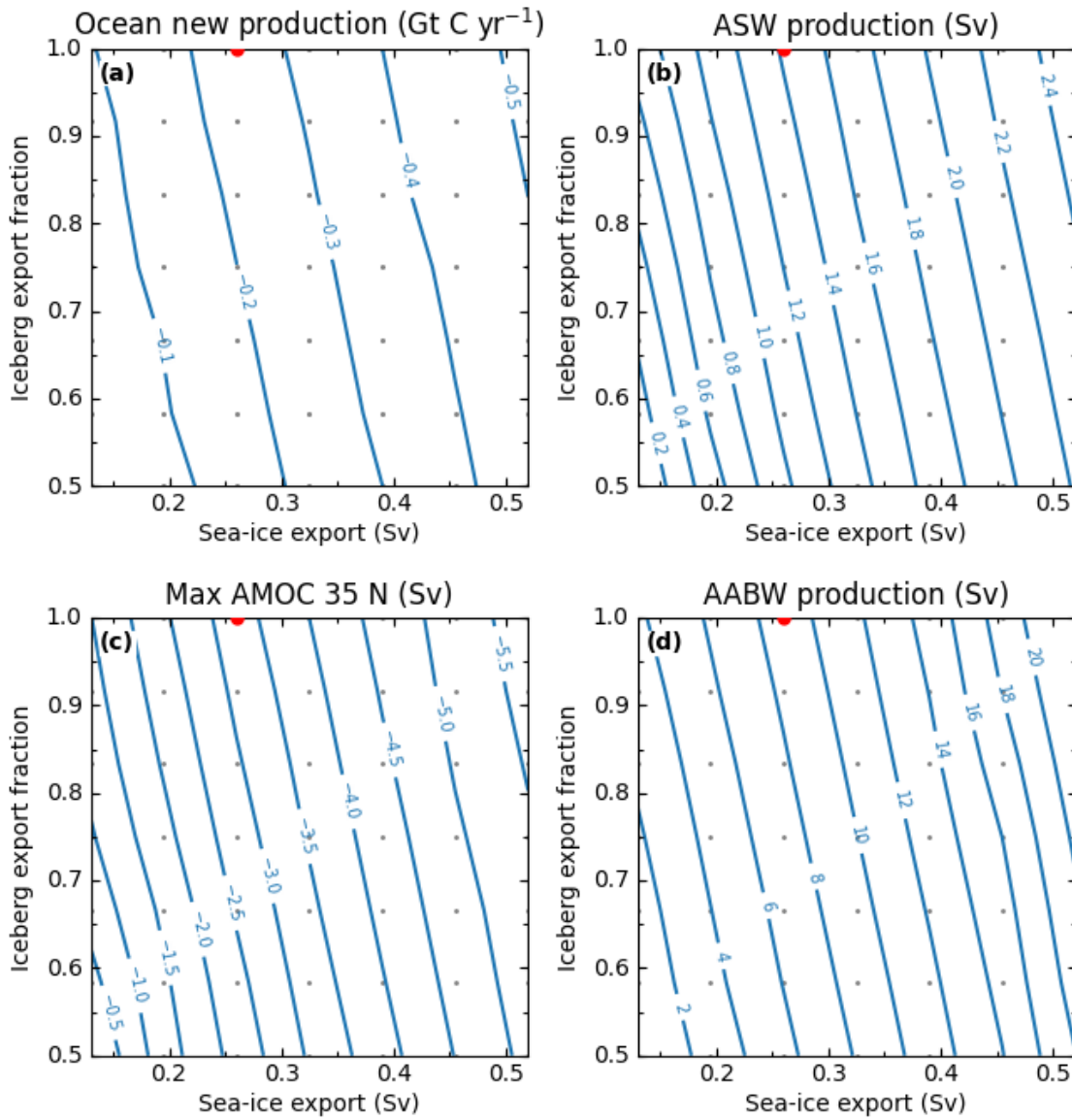


Figure S5. As in Figure S4 but for **a.** Ocean new production, **b.** Antarctic Shelf Water (ASW) production, **c.** Atlantic Meridional Overturning Circulation (AMOC) strength at 35 °N and **d.** AABW production.

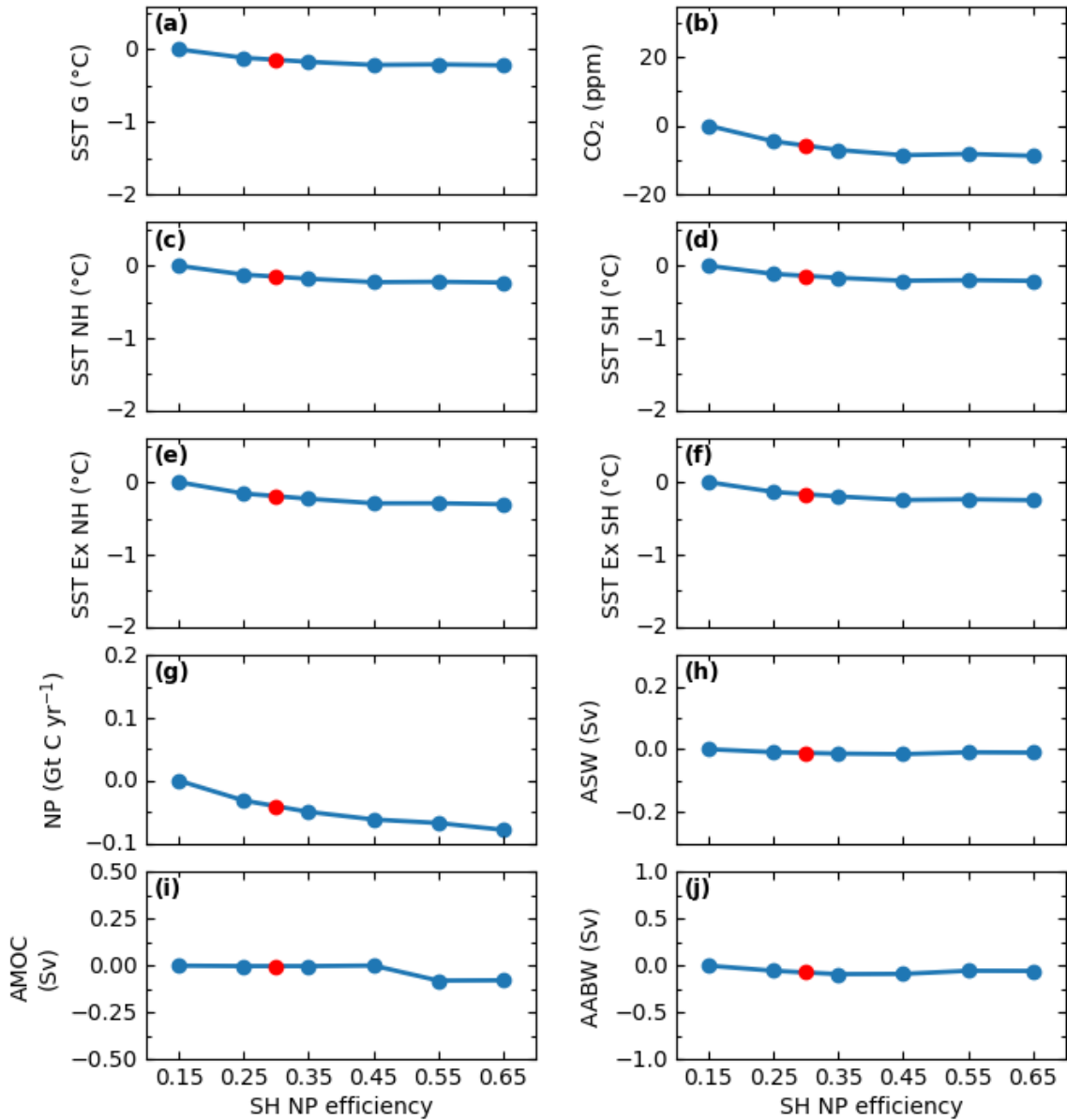


Figure S6. Model property differences from 1.5 Ma to 0.8 Ma as functions of different Southern Hemisphere new production (NP) efficiency factors, while all other forcings are applied using their standard case values (Table 1 in the main text). **a.** Global mean sea surface temperature (SST), **b.** atmospheric CO₂, **c.** - **d.** Northern and Southern Hemisphere SST, respectively, **e.** - **f.** Northern and Southern Hemisphere Extratropical (35°-55°) SST, respectively, **g.** Ocean new production (NP), **h.** Antarctic Shelf Water (ASW) production, **i.** Atlantic Meridional Overturning Circulation (AMOC) strength at 35°N and **j.** Antarctic Bottom Water (AABW) production. The left-hand blue dot is for the 1.5 Ma efficiency factor (0.15). The red dot marks the value used for the standard MPT simulation at 0.8 Ma, as described in the main text.

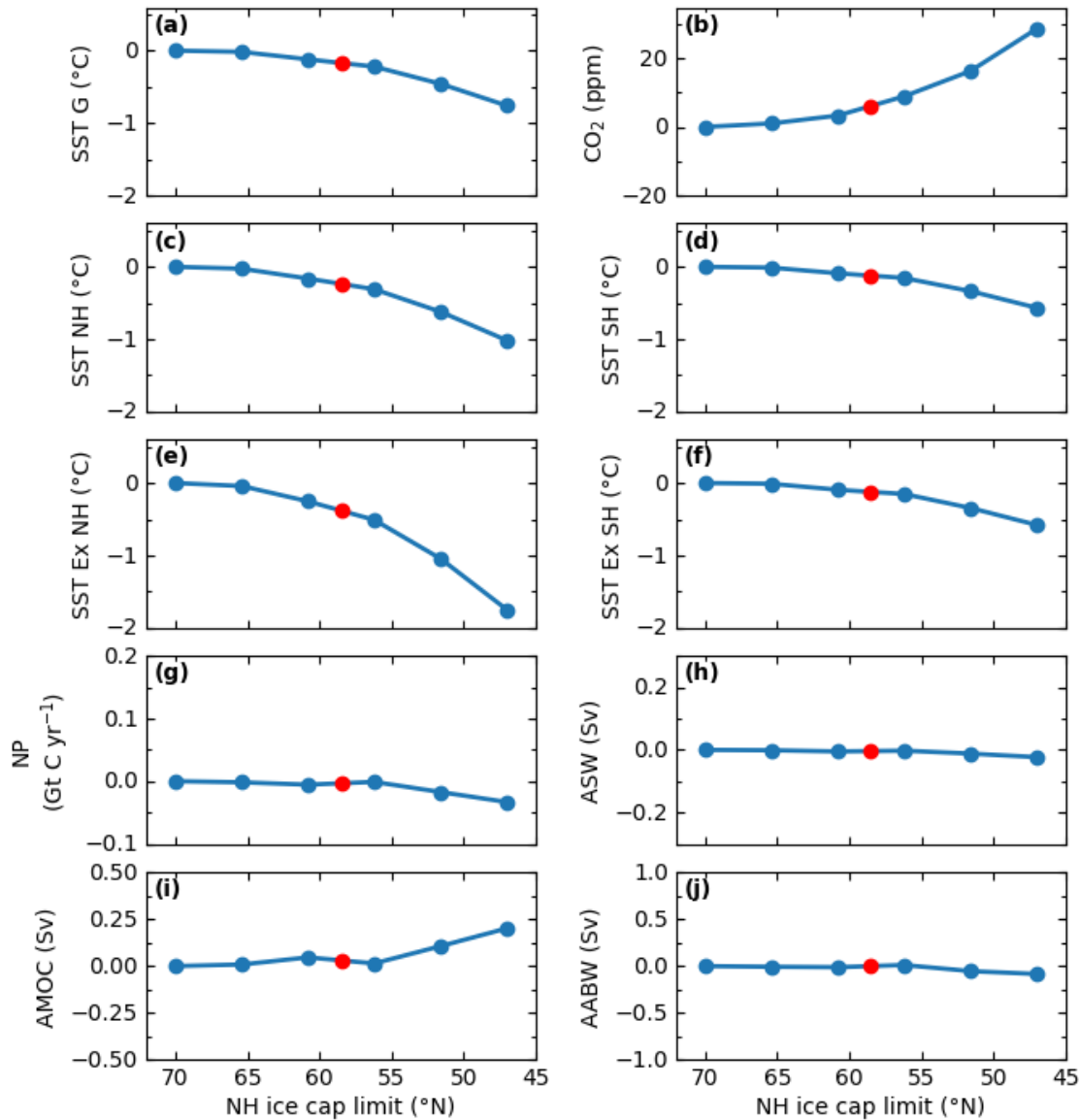


Figure S7. Model property differences between 0.8 Ma and 1.5 Ma as functions of the equatorward expansion of Northern Hemisphere ice sheets, while all other forcings are applied using their standard case values (Table 1 in the main text). **a.** Global mean sea surface temperature (SST), **b.** Atmospheric CO₂, **c.** - **d.** Northern and Southern Hemisphere SST, respectively, **e.** - **f.** Northern and Southern Hemisphere Extratropical (35°-55°) SST, respectively, **g.** Ocean new production (NP), **h.** Antarctic Shelf Water (ASW) production, **i.** Atlantic Meridional Overturning Circulation (AMOC) strength at 35°N and **j.** Antarctic Bottom Water (AABW) production. The left-hand blue dot is for the 1.5 Ma ice sheet latitude (70°N). The red dot marks the value used for the standard MPT simulation at 0.8 Ma, as described in the main text.

Ocean sector	Atlantic Ocean		Pacific Ocean	
	1.5 Ma	0.8 Ma	1.5 Ma	0.8 Ma
65°N-55°N	0.170	0.124	0.045	0.037
55°N-35°N	0.437	0.469	0.301	0.273
35°N-0°	0.430	0.395	1.351	1.084
0°-35°S	0.341	0.300	1.798	1.394
35°S-55°S	0.155	0.196	0.531	0.639
	Southern Ocean 55°S-69°S		Arctic Ocean 65°N-90°N	
	0.277	0.251	0.007	0.003

Table S1. Standard case, ocean new ocean production (Gt C yr^{-1}) for each ocean sector, 1.5 and 0.8 million years ago (Ma). Enhanced dust fertilization was applied to all ocean sectors south of 35°S (the entire model Southern Ocean) over this period.

5. DISCUSSION

5.1. A new Earth System Model

A new Earth System model of intermediate complexity, DCESS II (Fernández and Shaffer, 2025), has been described and tested which was calibrated to pre-industrial time. For this relatively simple model, efforts were made to limit the number of free parameters and to constrain their values as much as possible using observations. At the end of this process, despite model limitations, an excellent agreement with available modern observation was found. When compared with results from its predecessor (DCESS I, Shaffer et al., 2008), a number of improvements in this new model stand out, as described below.

The implementation of key features of the physical components of the model, like improved horizontal resolution, a simplified dynamical scheme for large-scale ocean circulation, stratification-dependent vertical diffusion, a gravity current approach to the formation of Antarctic Bottom Water (AABW) and a dynamical formulation for sea ice, have helped to achieve a good agreement with observed data like atmospheric heat and water vapor transport and ocean temperature and salinity distributions, not possible using the previous version of the model. These improvements, together with updates in ocean biogeochemistry such as light dependence of the surface new (export) production of organic matter, dependence on the calcite saturation state for the biogenic carbonate production and local temperature dependence on organic matter remineralization, resulted in accurate model representations of ocean biogeochemical tracers, highlighted by excellent model-data agreement with regard to marine carbon cycle species. This agreement was well beyond that achieved with DCESS I, in particular with respect to ^{13}C . Furthermore, the incorporation of a new land biosphere module including three different vegetation types and a light-atmospheric CO_2 dependence on net primary production on land, as well as ocean sediment and lithosphere modules applied to multiple ocean and land sectors, makes results of the new model much more amenable to comparison with data than is the case for its predecessor. All the above improvements help make the DCESS II model an excellent yet economical tool for studying and gaining short- as well as long-term understanding of the global carbon cycle.

In order to explore and test the model performance, two simple experiments were conducted. In the first experiment the model was forced in a way that emulates the role of the Southern Hemisphere Westerly Winds (SWW) in large-scale ocean circulation. In the second experiment, a freshwater pulse onto the shelf surrounding Antarctica was introduced to mimic the effect of Antarctic ice sheet melt. In both experiments, model results showed important physical and biogeochemical changes in the ocean, driving perturbations in the global carbon cycle. These experiments served to demonstrate how the model captures the global role that SWW and AABW play in the Earth system. Furthermore, the first experiment supports the role of Southern Hemisphere westerly winds in modulating glacial-interglacial atmospheric carbon dioxide variations, while the second experiment points to the impact that future Antarctic ice sheet melting would have on the formation of AABW and on the deep global ocean in general.

The development and calibration of the DCESS II model, as described in Fernández and Shaffer (2025), have also set the stage for future work. For example, coupling of the model to an Antarctic ice sheet (AIS) model will provide a more realistic Earth system simulations, especially when compared to the idealized second experiment. For this work, an extended and improved version of the simple, well-tested DAIS model (Shaffer, 2014) would be used. In another example, planned incorporation of methane, nitrogen and sulfur cycles into a next DCESS II update will significantly improve its ability to deal realistically with deep-time global warming events associated with massive carbon inputs to the Earth system. Under such conditions, suboxic/anoxic ocean conditions may arise, leading, for example, to denitrification and sulfate reduction that must be addressed in such an update. Groundwork for this step has already been done in as much as these global biogeochemical cycles and suboxic/anoxic processes have been incorporated into the DCESS I model (Shaffer et al., 2017). Finally, other potential model applications include the study of different global climatic events like Dansgaard-Oeschger oscillations or longer climatic events like the Eocene-Oligocene transition or even the assessment of deep-time mass extinction events by taking advantage of the relatively simplicity of the model for setting proper boundary conditions like orbital forcing and continental distribution.

5.2. The Middle Pleistocene Transition

The newly-developed Earth System model of intermediate complexity DCESS II (Fernández et al., 2025), was applied to better understand the strong, observed cooling across the Middle Pleistocene Transition (MPT) from about 1.5 to 0.8 million years ago (Ma). During the MPT, glacial-interglacial cycles became longer, stronger and more asymmetric. Various underlying causes for this transition have been proposed (An et al., 2024; Clark et al., 2006; Clark et al., 2024; Raymo et al., 2006; Ruddiman et al., 1986; Tziperman and Gildor, 2004; Willeit et al., 2019) but it appears clear that the strong cooling laid the groundwork this for system change by, for example, forcing Northern Hemisphere ice sheet growth.

In order to explain the cooling across the MPT and inspired by recent analyses indicating the importance of Southern Hemisphere processes then (Clark et al., 2024; An et al., 2024), three Southern Hemisphere forcings were proposed: F1. Southern West Wind strength and position, F2. Sea ice and iceberg export from the Antarctic shelf, F3. Southern Ocean dust fertilization, to which an additional forcing was added: F4. Northern Hemisphere ice sheet extent.

To match observed SST and atmospheric CO₂ at 4 Ma, a high-end, climate-sensitivity of 5°C per doubling CO₂ was needed. Then initial, simulated pre-MPT cooling was ultimately forced by an applied, linearly-increasing weatherability, representing non-temperature-dependent weathering changes from factors like mountain building. Since weatherability as so defined would not be expected to be climate-dependent, we applied this same calibrated rate increase across the MPT, explaining part of the cooling there. The remaining MPT cooling was addressed by the proposed forcings F1, F2, F3 and F4.

The standard-case simulation reproduced main features of observed global and regional SST trends over the last 4 million years (Clark et al., 2024), including relatively uniform global cooling from 4 to 1.5 Ma, followed by accelerated and regionally variable cooling across the MPT. Furthermore, model results indicated that by the end of the MPT (0.8 Ma), the CO₂ decline was consistent with ice core records (Bereiter et al., 2015). Moreover, considering several carbon-related ocean model properties, modelled results indicated the development of an older, carbon-rich, more acidic and more uniform deep-water mass, as in reconstructions (Farmer et al., 2019; Lear et al., 2016; Thomas et al., 2022). This followed a large increase in AABW

formation across the MPT, initiated by more formation of denser Antarctic Shelf Water from greater brine rejection due to the prescribed increase in sea ice and iceberg export from the shelf. However, the most of the AABW transport increase came from the enhanced entrainment of deeper waters as the AABW plume in the model's gravity current approach flows down the Antarctic slope. This led to enhanced deep ocean recirculation, isolated from the atmosphere, and explained the deep-water mass mentioned above and, thereby, much of the atmospheric CO₂ decrease across the MPT that was not explained by weathering.

The prescribed increase in sea ice and iceberg export from the Antarctic shelf also freshened the upper Southern Ocean as this ice melted. Together with less upwelling of relatively-salty water carried by the Atlantic Meridional Overturning Circulation, due to the prescribed weaker, equatorward-displaced Southern West Winds, this led to increased upper ocean stratification and decreased model vertical diffusivity there. Less upward heat transport from mixing and advection and less air-sea heat exchange from more extensive Southern Ocean sea ice cover explained much of the observed, amplified Southern Hemisphere SST cooling across the MPT. Likewise, this combination further trapped carbon in the deep ocean, helping to draw down atmospheric CO₂.

In order to isolate the effects of each forcing, additional MPT simulations were carried out. Although each forcing produced distinct magnitudes and patterns of SST cooling, interactions among them are essential for reproducing the standard case cooling. Moreover, sensitivity studies varying each forcing in plausible ranges, showed interesting Earth System property responses and would allow tuning of the model for an improved fit to observed SST drops across the MPT.

The standard case simulation was able to explain most of the size and structure of observed SST cooling across the MPT, however, some of the remaining cooling is likely explained by other processes and interactions not considered, nor indeed addressable, by the new simplified model. For example, longer, stronger and more asymmetric glacial-interglacial cycles developed across the MPT with longer glacial and shorter interglacial periods. Mean temperatures across such cycles would show more cooling because of this asymmetry alone.

The results shown in section 4.2 underline the importance of modelling AABW formation in agreement with observations. The new DCESS II model uses a simplified gravity current-

entrainment formulation to capture in a realistic way how AABW is formed. Deep recirculation that follows from this formulation was a key factor in the modelled atmospheric CO₂ drawdown across the MPT, but such deep recirculation would be missed, or at least misrepresented, in the bulk of Earth system models, as they rely on deep convection or omit downslope entrainment processes when forming AABW (Heuzé, 2021).

While much remains for future work on the Middle Pleistocene Transition, the results here underline the central role that mid- and high latitude, Southern Hemisphere processes play in ushering in the MPT by forcing strong global and regional cooling across it.

6. CONCLUSIONS

Based on the results presented in Sections 4.1 and 4.2, it can be concluded that:

- A simple and fast new Earth system model of intermediate complexity has been presented, validated and tested intended to be a flexible, comprehensive and economical Earth system modelling platform. Despite its limitations, the model represents most Earth system components quite well, especially the global-scale carbon cycle. Due to its simplicity, it could be easily modified in terms of boundary conditions to address specific past epochs. Thus, DCESS II has proven to be a useful tool for studies of past, present and future global change on timescales of years to millions of years while not needing substantial computational resources.
- When DCESS II model was applied to study the period from 4 Ma to 0.8 Ma, the model was able to reproduce the long-term cooling trend from 4 Ma to 1.5 Ma, as well as the stronger cooling associated to the Middle Pleistocene Transition occurring between 1.5 Ma and 0.8 Ma. The first mechanism involved a non-climate-dependent factor, such as enhanced weathering rates, particularly from orogenic activity (e.g., mountain building). For the latter, proposed mid- and high-latitude Southern Hemisphere forcings explained much of the cooling across de MPT. However, the results highlight the importance of the combined interactions among the forcings for producing the observed cooling.

7. REFERENCES

- Abe-Ouchi, A., Saito, F., Kawamura, K., Raymo, M. E., Okuno, J. I., Takahashi, K., & Blatter, H. (2013). Insolation-driven 100,000-year glacial cycles and hysteresis of ice-sheet volume. *Nature*, 500(7461), 190-193. <https://doi.org/10.1038/nature12374>.
- Amante, C., & Eakins, B. W. (2009). ETOPO1 arc-minute global relief model: Procedures, data sources and analysis. NOAA Technical Memorandum NESDIS NGDC-24 [dataset]. <https://doi.org/10.7289/V5C8276M>.
- An, Z., Zhou, W., Zhang, Z., Zhang, X., Liu, Z., Sun, Y., et al. (2024). Mid-Pleistocene climate transition triggered by Antarctic Ice Sheet growth. *Science*, 385(6708), 560-565. <https://doi.org/10.1126/science.abn4861>.
- Anderson, R. F., Ali, S., Bradtmiller, L. I., Nielsen, S. H. H., Fleisher, M. Q., Anderson, B. E., & Burckle, L. H. (2009). Wind-Driven Upwelling in the Southern Ocean and the Deglacial Rise in Atmospheric CO₂. *Science*, 323(5920), 1443-1448. <https://doi.org/10.1126/science.1167441>
- Ao, H., Rohling, E. J., Li, X., Song, Y., Roberts, A. P., Han, Y., et al. (2023). Northern hemisphere ice sheet expansion intensified Asian aridification and the winter monsoon across the mid-Pleistocene transition. *Communications Earth & Environment*, 4(36). <https://doi.org/10.1038/s43247-023-00686-9>.
- Baines, P. G. (2005). Mixing regimes for the flow of dense fluid down slopes into stratified environments. *Journal of Fluid Mechanics*, 538, 245-267. <https://doi.org/10.1017/S0022112005005434>.
- Baines, P. G. (2008). Mixing in Downslope Flows in the Ocean - Plumes versus Gravity Currents. *Atmosphere-Ocean*, 46(4), 405-419. <https://doi.org/10.3137/ao.460402>.
- Bambach, R. K. (2006). Phanerozoic biodiversity mass extinctions. *Annual Review of Earth and Planetary Sciences*, 34, 127-155. <https://doi.org/10.1146/annurev.earth.33.092203.122654>.
- Bartoli, G., Hönisch, B., & Zeebe, R. E. (2011). Atmospheric CO₂ decline during the Pliocene intensification of Northern Hemisphere glaciations. *Paleoceanography*, 26(4), PA4213. <https://doi.org/10.1029/2010PA002055>.

- Batchelor, C. L., Margold, M., Krapp, M., Murton, D. K., Dalton, A. S., Gibbard, P. L., et al. (2019). The configuration of Northern Hemisphere ice sheets through the Quaternary. *Nature Communications*, 10(3713). <https://doi.org/10.1038/s41467-019-11601-2>.
- Bayon, G., Patriat, M., Godderis, Y., Trinquier, A., De Deckker, P., Kulhanek, D. K., et al. (2023). Accelerated mafic weathering in Southeast Asia linked to late Neogene cooling. *Science Advances*, 9(13), eadf3141. <https://doi.org/10.1126/sciadv.adf3141>.
- Bereiter, B., Eggleston, S., Schmitt, J., Nehrbass-Ahles, C., Stocker, T. F., Fischer, H., et al. (2015). Revision of the EPICA Dome C CO₂ record from 800 to 600 kyr before present. *Geophysical Research Letters*, 42(2), 542-549. <https://doi.org/10.1002/2014GL061957>.
- Berends, C. J., Köhler, P., Lourens, L. J., & Van De Wal, R. S. W. (2021). On the Cause of the Mid-Pleistocene Transition. *Reviews of Geophysics*, 59, e2020RG000727. <https://doi.org/10.1029/2020RG000727>.
- Berger, A., & Loutre, M. F. (1991). Insolation values for the climate of the last 10 million years. *Quaternary Science Reviews*, 10(4), 297-317. [https://doi.org/10.1016/0277-3791\(91\)90033-Q](https://doi.org/10.1016/0277-3791(91)90033-Q).
- Berner, R. (1980). *A. Early Diagenesis: A Theoretical Approach*. Princeton University Press. <https://doi.org/10.2307/j.ctvx8b6p2>.
- Bintanja, R., & Van De Wal, R. S. W. (2008). North American ice-sheet dynamics and the onset of 100,000-year glacial cycles. *Nature*, 454(7206), 869-872. <https://doi.org/10.1038/nature07158>.
- Bonan, G. B. (2008). Forests and Climate Change: Forcings, Feedbacks, and the Climate Benefits of Forests. *Science*, 320(5882), 1444-1449. <https://doi.org/10.1126/science.1155121>.
- Chapin III, S. F., Matson, P. A., and Vitousek, P. (2011). *Principles of terrestrial ecosystem ecology*, Springer, New York, NY, USA, <https://doi.org/10.1007/978-1-4419-9504-9>.
- Chen, C., Riley, W. J., Prentice, I. C., & Keenan, T. F. (2022). CO₂ fertilization of terrestrial photosynthesis inferred from site to global scales. *Proceedings of the National Academy of Sciences*, 119(10). <https://doi.org/10.1073/pnas.2115627119>.

- Chiang, J. C. H., Maffre, P., Swanson-Hysell, N. L., & Macdonald, F. A. (2024). The Role of Southeast Asian Island Topography on Indo-Pacific Climate and Silicate Weathering. *Paleoceanography and Paleoclimatology*, 39(3). <https://doi.org/10.1029/2023PA004672>.
- Ciais, P., Tagliabue, A., Cuntz, M., Bopp, L., Scholze, M., Hoffmann, G., et al. (2012). Large inert carbon pool in the terrestrial biosphere during the Last Glacial Maximum. *Nature Geoscience*, 5(1), 74-79. <https://doi.org/10.1038/ngeo1324>.
- Clark, P. U., Archer, D., Pollard, D., Blum, J. D., Rial, J. A., Brovkin, V., et al. (2006). The middle Pleistocene transition: characteristics, mechanisms, and implications for long-term changes in atmospheric pCO₂. *Quaternary Science Reviews*, 25(23), 3150-3184. <https://doi.org/10.1016/j.quascirev.2006.07.008>.
- Clark, P. U., & Pollard, D. (1998). Origin of the Middle Pleistocene Transition by ice sheet erosion of regolith. *Paleoceanography*, 13(1), 1-9. <https://doi.org/10.1029/97PA02660>.
- Clark, P. U., Shakun, J. D., Rosenthal, Y., Köhler, P., & Bartlein, P. J. (2024). Global and regional temperature change over the past 4.5 million years. *Science*, 383(6685), 884-890. <https://doi.org/10.1126/science.adi1908>.
- Crisp, D., Dolman, H., Tanhua, T., Mckinley, G. A., Hauck, J., Bastos, A., et al. (2022). How Well Do We Understand the Land-Ocean-Atmosphere Carbon Cycle? *Reviews of Geophysics*, 60(2). <https://doi.org/10.1029/2021RG000736>.
- Davidson, E. A., & Janssens, I. A. (2006). Temperature sensitivity of soil carbon decomposition and feedbacks to climate change. *Nature*, 440(7081), 165-173. <https://doi.org/10.1038/nature04514>.
- DeVries, T. (2022). The Ocean Carbon Cycle. *Annual Review of Environment and Resources*, 47, 317-341. <https://doi.org/10.1146/annurev-environ-120920-111307>.
- Eichinger, R., Shaffer, G., Albarran, N., Rojas, M., & Lambert, F. (2017). An improved land biosphere module for use in the DCESS Earth system model (version 1.1) with application to the last glacial termination. *Geoscientific Model Development*, 10(9), 3481-3498. <https://doi.org/10.5194/gmd-10-3481-2017>.

- Elderfield, H., Ferretti, P., Greaves, M., Crowhurst, S., McCave, I. N., Hodell, D., & Piotrowski, A. M. (2012). Evolution of Ocean Temperature and Ice Volume Through the Mid-Pleistocene Climate Transition. *Science*, 337(6095), 704-709. <https://doi.org/10.1126/science.1221294>.
- Farmer, J. R., Hönisch, B., Haynes, L. L., Kroon, D., Jung, S., Ford, H. L., et al. (2019). Deep Atlantic Ocean carbon storage and the rise of 100,000-year glacial cycles. *Nature Geoscience*, 12(5), 355-360. <https://doi.org/10.1038/s41561-019-0334-6>.
- Fernández Villanueva, E., & Shaffer, G. (2025). Presentation, calibration and testing of the DCESS II Earth system model of intermediate complexity (version 1.0). *Geoscientific Model Development*, 18(7), 2161-2192. <https://doi.org/10.5194/gmd-18-2161-2025>.
- Flato, G. M. (2011). Earth system models: an overview. *WIREs Climate Change*, 2(6), 783-800. <https://doi.org/10.1002/wcc.148>.
- Frey, S. D., Lee, J., Melillo, J. M., & Six, J. (2013). The temperature response of soil microbial efficiency and its feedback to climate. *Nature Climate Change*, 3(4), 395-398. <https://doi.org/10.1038/nclimate1796>.
- Gordon, A. L. (2019). Bottom Water Formation. In J. K. Cochran, H. J. Bokuniewicz, & P. L. Yager (Eds.), *Encyclopedia of Ocean Sciences (Third Edition)* (pp. 120-126). Oxford: Academic Press. <https://doi.org/10.1016/B978-0-12-409548-9.04019-7>.
- Hain, M. P., Sigman, D. M., & Haug, G. H. (2014). The Biological Pump in the Past. In H. D. Holland & K. K. Turekian (Eds.), *Treatise on Geochemistry (Second Edition)* (pp. 485-517). Oxford: Elsevier. <https://doi.org/10.1016/B978-0-08-095975-7.00618-5>.
- Herbert, T. D. (2023). The Mid-Pleistocene Climate Transition. *Annual Review of Earth and Planetary Sciences*, 51, 389-418. <https://doi.org/10.1146/annurev-earth-032320-104209>
- Heuzé, C. (2021). Antarctic Bottom Water and North Atlantic Deep Water in CMIP6 models. *Ocean Science*, 17(1), 59-90. <https://doi.org/10.5194/os-17-59-2021>.
- Hodell, D. A., & Channell, J. E. T. (2016). Mode transitions in Northern Hemisphere glaciation: co-evolution of millennial and orbital variability in Quaternary climate. *Climate of the Past*, 12(9), 1805-1828. <https://doi.org/10.5194/cp-12-1805-2016>.

- Jones, M. C., Grosse, G., Treat, C., Turetsky, M., Anthony, K. W., & Brosius, L. (2023). Past permafrost dynamics can inform future permafrost carbon-climate feedbacks. *Communications Earth & Environment*, 4, 272. <https://doi.org/10.1038/s43247-023-00886-3>.
- Köhler, P. (2023). Atmospheric CO₂ concentration based on boron isotopes versus simulations of the global carbon cycle during the Plio-Pleistocene. *Paleoceanography and Paleoclimatology*, 786 38(2), e2022PA004439. <https://doi.org/10.1029/2022PA004439>.
- Lamy, F., Gersonde, R., Winckler, G., Esper, O., Jaeschke, A., Kuhn, G., et al. (2014). Increased Dust Deposition in the Pacific Southern Ocean During Glacial Periods. *Science*, 343(6169), 403-407. <https://doi.org/10.1126/science.1245424>.
- LaRiviere, J. P., Ravelo, A. C., Crimmins, A., Dekens, P. S., Ford, H. L., Lyle, M., & Wara, M. W. (2012). Late Miocene decoupling of oceanic warmth and atmospheric carbon dioxide forcing. *Nature*, 486(7401), 97-100. <https://doi.org/10.1038/nature11200>.
- Lear, C. H., Billups, K., Rickaby, R. E. M., Diester-Haass, L., Mawbey, E. M., & Sosdian, S. M. (2016). Breathing more deeply: Deep ocean carbon storage during the mid-Pleistocene climate transition. *Geology*, 44(12), 1035-1038. <https://doi.org/10.1130/G38636.1>.
- Lisiecki, L. E., & Raymo, M. E. (2005). A Pliocene-Pleistocene stack of 57 globally distributed benthic $\delta^{18}\text{O}$ records. *Paleoceanography*, 20, PA1003. <https://doi.org/10.1029/2004PA001071>.
- Maier-Reimer, E. (1993). Geochemical cycles in an ocean general circulation model. Preindustrial tracer distributions. *Global Biogeochemical Cycles*, 7(3), 645-677. <https://doi.org/10.1029/93gb01355>.
- Manning, C. E. (2014). A piece of the deep carbon puzzle. *Nature Geoscience*, 7(5), 333-334. <https://doi.org/10.1038/ngeo2152>.
- Marchal, O., Stocker, T. F., & Joos, F. (1998). A latitude-depth, circulation-biogeochemical ocean model for paleoclimate studies. Development and sensitivities. *Tellus B*, 50(3), 290-316. <https://doi.org/10.3402/tellusb.v50i3.16130>.
- Martin, P. E., Macdonald, F. A., Mcquarrie, N., Flowers, R. M., & Maffre, P. J. Y. (2023). The rise of New Guinea and the fall of Neogene global temperatures. *Proceedings of the National Academy of Sciences*, 120(40), e2306492120. <https://doi.org/10.1073/pnas.2306492120>.

- Martínez-García, A., Rosell-Melé, A., Jaccard, S. L., Geibert, W., Sigman, D. M., & Haug, G. H. (2011). Southern Ocean dust–climate coupling over the past four million years. *Nature*, 476(7360), 312-315. <https://doi.org/10.1038/nature10310>.
- Medina-Elizalde, M., & Lea, D. W. (2005). The Mid-Pleistocene Transition in the Tropical Pacific. *Science*, 310(5750), 1009-1012. <https://doi.org/10.1126/science.1115933>.
- Olsen, S. M., Shaffer, G., & Bjerrum, C. J. (2005). Ocean oxygen isotope constraints on mechanisms for millennial-scale climate variability. *Paleoceanography*, 20, PA1014. <https://doi.org/10.1029/2004PA001063>.
- Orsi, A. H., Smethie Jr., W. M., & Bullister, J. L. (2002). On the total input of Antarctic waters to the deep ocean: A preliminary estimate from chlorofluorocarbon measurements. *Journal of Geophysical Research*, 107(C8). <https://doi.org/10.1029/2001JC000976>.
- Pagani, M., Caldeira, K., Archer, D., & Zachos, J. C. (2006). An Ancient Carbon Mystery. *Science*, 314(5805), 1556-1557. <https://doi.org/10.1126/science.1136110>.
- Pan, X., Chen, D., Pan, B., Huang, X., Yang, K., Piao, S., et al. (2025). Evolution and prospects of Earth system models: Challenges and opportunities. *Earth-Science Reviews*, 260, 104986. <https://doi.org/10.1016/j.earscirev.2024.104986>.
- Pierrehumbert, R. T., Abbot, D. S., Voigt, A., & Koll, D. (2011). Climate of the Neoproterozoic. *Annual Review of Earth and Planetary Sciences*, 39, 417-460. <https://doi.org/10.1146/annurev-earth-040809-152447>.
- Prinn, R. G. (2013). Development and application of earth system models. *Proceedings of the National Academy of Sciences*, 110, 3673-3680. <https://doi.org/10.1073/pnas.1107470109>.
- Raymo, M. E., Lisiecki, L. E., & Nisancioglu, K. H. (2006). Plio-Pleistocene Ice Volume, Antarctic Climate, and the Global $\delta^{18}\text{O}$ Record. *Science*, 313(5786), 492-495. <https://doi.org/10.1126/science.1123296>.
- Ruddiman, W. F., Raymo, M., & McIntyre, A. (1986). Matuyama 41,000-year cycles: North Atlantic Ocean and northern hemisphere ice sheets. *Earth and Planetary Science Letters*, 80(1), 117-129. [https://doi.org/10.1016/0012-821X\(86\)90024-5](https://doi.org/10.1016/0012-821X(86)90024-5).

Sarmiento, J., L., & Gruber, N. (2006). *Ocean Biogeochemical Dynamics*, Princeton University Press, Princeton, New Jersey, USA, <https://doi.org/10.2307/j.ctt3fgxqx>.

Saugier, B., Roy, J., and Mooney, H. A. (Eds.) (2001). Estimations of global terrestrial productivity: converging toward a single number?, in: *Terrestrial Global Productivity*, Academic Press, San Diego, CA, 543–557. <https://doi.org/10.1016/B978-012505290-0/50024-7>.

Shaffer, G. (2014). Formulation, calibration and validation of the DAIS model (version 1), a simple Antarctic ice sheet model sensitive to variations of sea level and ocean subsurface temperature. *Geoscientific Model Development*, 7(4), 1803-1818. <https://doi.org/10.5194/gmd-7-1803-2014>.

Shaffer, G., Fernández Villanueva, E., Rondanelli, R., Pedersen, J. O. P., Olsen, S. M., & Huber, M. (2017). Implementation of methane cycling for deep-time global warming simulations with the DCESS Earth system model (version 1.2). *Geoscientific Model Development*, 10(11), 4081-4103. <https://doi.org/10.5194/gmd-10-4081-2017>.

Shaffer, G., Huber, M., Rondanelli, R., & Pepke Pedersen, J. O. (2016). Deep time evidence for climate sensitivity increase with warming. *Geophysical Research Letters*, 43(12), 6538-6545. <https://doi.org/10.1002/2016gl069243>.

Shaffer, G., & Lambert, F. (2018). In and out of glacial extremes by way of dust–climate feedbacks. *Proceedings of the National Academy of Sciences*, 115(9), 2026-2031. <https://doi.org/10.1073/pnas.1708174115>.

Shaffer, G., Malskær Olsen, S., & Pepke Pedersen, J. O. (2008). Presentation, calibration and validation of the low-order, DCESS Earth System Model (Version 1). *Geoscientific Model Development*, 1, 17-51. <https://doi.org/10.5194/gmd-1-17-2008>.

Shin, S. I., Liu, Z., Otto-Bliesner, B. L., Kutzbach, J. E., & Vavrus, S. J. (2003). Southern Ocean sea-ice control of the glacial North Atlantic thermohaline circulation. *Geophysical Research Letters*, 30(2), 1096. <https://doi.org/10.1029/2002GL015513>.

Sosdian, S. M., Greenop, R., Hain, M. P., Foster, G. L., Pearson, P. N., & Lear, C. H. (2018). Constraining the evolution of Neogene ocean carbonate chemistry using the boron isotope pH

proxy. *Earth and Planetary Science Letters*, 498, 362-376. <https://doi.org/10.1016/j.epsl.2018.06.017>.

Starr, A., Hall, I. R., Barker, S., Rackow, T., Zhang, X., Hemming, S. R., et al. (2021). Antarctic icebergs reorganize ocean circulation during Pleistocene glacials. *Nature*, 589(7841), 236-241. <https://doi.org/10.1038/s41586-020-03094-7>.

Steffen, W., Richardson, K., Rockström, J., Schellnhuber, H. J., Dube, O. P., Dutreuil, S., et al. (2020). The emergence and evolution of Earth System Science. *Nature Reviews Earth & Environment*, 1(1), 54-63. <https://doi.org/10.1038/s43017-019-0005-6>.

Tesi, T., Muschitiello, F., Smittenberg, R. H., Jakobsson, M., Vonk, J. E., Hill, P., et al. (2016). Massive remobilization of permafrost carbon during post-glacial warming. *Nature Communications*, 7(1), 13653. <https://doi.org/10.1038/ncomms13653>.

Thomas, N. C., Bradbury, H. J., & Hodell, D. A. (2022). Changes in North Atlantic deep-water oxygenation across the Middle Pleistocene Transition. *Science*, 377(6606), 654-659. <https://doi.org/10.1126/science.abj7761>.

Toggweiler, J. R., Russell, J. L., & Carson, S. R. (2006). Midlatitude westerlies, atmospheric CO₂, and climate change during the ice ages. *Paleoceanography*, 21(2), PA2005. <https://doi.org/10.1029/2005PA001154>.

Tziperman, E., & Gildor, H. (2003). On the mid-Pleistocene transition to 100-kyr glacial cycles and the asymmetry between glaciation and deglaciation times. *Paleoceanography*, 18(1), 1001. <https://doi.org/10.1029/2001PA000627>.

Venugopal, A. U., Bertler, N. A. N., Severinghaus, J. P., Brook, E. J., Cortese, G., Lee, J. E., et al. (2023). Antarctic evidence for an abrupt northward shift of the Southern Hemisphere westerlies at 32 ka BP. *Nature Communications*, 14, 5432. <https://doi.org/10.1038/s41467-023-40951-1>.

Volk, T., & Hoffert, M. I. (1985). Ocean Carbon Pumps: Analysis of Relative Strengths and Efficiencies in Ocean-Driven Atmospheric CO₂ Changes. In *The Carbon Cycle and Atmospheric CO₂: Natural Variations Archean to Present* (pp. 99-110). <https://doi.org/10.1029/GM032p0099>.

von der Heydt, A. S., Ashwin, P., Camp, C. D., Crucifix, M., Dijkstra, H. A., Ditlevsen, P., & Lenton, T. M. (2021). Quantification and interpretation of the climate variability record. *Global and Planetary Change*, 197, 103399. <https://doi.org/10.1016/j.gloplacha.2020.103399>.

Westerhold, T., Marwan, N., Drury, A. J., Liebrand, D., Agnini, C., Anagnostou, E., et al. (2020). An astronomically dated record of Earth's climate and its predictability over the last 66 million years. *Science*, 369(6509), 1383-1387. <https://doi.org/10.1126/science.aba6853>.

Willeit, M., Ganopolski, A., Calov, R., & Brovkin, V. (2019). Mid-Pleistocene transition in glacial cycles explained by declining CO₂ and regolith removal. *Science Advances*, 5(4), eaav7337. <https://doi.org/10.1126/sciadv.aav7337>.

Zachos, J., Pagani, M., Sloan, L., Thomas, E., & Billups, K. (2001). Trends, Rhythms, and Aberrations in Global Climate 65 Ma to Present. *Science*, 292(5517), 686-693. <https://doi.org/10.1126/science.1059412>.

Zachos, J. C., Dickens, G. R., & Zeebe, R. E. (2008). An early Cenozoic perspective on greenhouse warming and carbon-cycle dynamics. *Nature*, 451(7176), 279-283. <https://doi.org/10.1038/nature06588>.

Zeebe, R. E., & Tyrrell, T. (2019). History of carbonate ion concentration over the last 100 million years II: Revised calculations and new data. *Geochimica et Cosmochimica Acta*, 257, 373-392. <https://doi.org/10.1016/j.gca.2019.02.041>.